Variation of image counts with patient anatomy and development of a Monte Carlo simulation system for whole-body bone scans.

A thesis submitted in partial fulfilment of

the requirements for the

Degree of Master of Science in

Medical Physics

By

Ross J. McGurk

University of Canterbury

2007

Table of contents

List of Figures

List of Tables

Acknowledgments

First, I wish to express my sincere appreciation to Mr Darin O'Keeffe, Dr Richard Watts and Dr Deloar Hossain for their time, support and input into the project as my supervisors. Second, I thank Professor Michael Ljungberg of Lund University, Sweden and Associate Professor William Paul Segars at Duke University, USA for their support with the SIMIND program and NCAT phantom, respectively. Third, to Dr John Turner and the Nuclear Medicine nurses and technologists, whose effort in the collection of patient data and design of the clinical study were greatly appreciated. Finally, my thanks and my love goes to my parents, Brian and Denise for all the support given to me over the years. I also wish to thank my friends for their support in what has been a challenging year. I would not be where I am today without all of you.

Abbreviations

AIC	Akaike Information Criteria
ALARA	As Low as Reasonably Achievable
BMI	Body Mass Index
Co-57	A radioactive form of the element cobalt
FOV	Field Of View
FWHM	Full Width at Half Maximum
FWTM	Full Width at Tenth Maximum
GE	General Electric
HDP/HMDP	hydroxymethylene diphosponate
keV	kiloelectron Volt (1000 electron Volts or 1.6×10^{-16} Joules)
LEGP	Low Energy General Purpose
LEHR	Low Energy High Resolution
MBq	Megabequerel (1 million counts per second)
MIRD	Medical Internal Radiation Dose
Mo-99	Molybdenum-99. The parent nuclide of Tc-99m
MRI	Magnetic Resonance Imaging
NCAT	NURBS Cardiac and Torso
NURBS	Non-Uniform-Rational B-Splines
PDF	Probability Distribution Function
PET	Positron Emission Tomography
QA	Quality Assurance
SNR	Signal to Noise Ratio
SPECT	Single Photon Emission Tomography
Tc-99m	The isomeric state of Tc-99

Abstract

The optimisation of image quality in medical imaging techniques is a significant factor in favourable patient prognoses. The number of counts in a nuclear medicine image is one factor in determining the diagnostic value of the image. The current study aims to determine the variation in counts in whole-body bone scan images with patient height and weight. Three separate studies were undertaken as part of the investigation.

First, 65 whole-body bone scans were analysed together with patient height, weight, age and sex. Weight was found to the most important anatomy influence on image counts. However, significant influences from patient sex and age meant that a useful relationship between image counts and patient anatomy based solely on height and weight could not be determined.

For the second study, a model of General Electric Millennium MG gamma camera was created and validated within the SIMIND Monte Carlo software. The results indicate that the model is an accurate representation of the gamma camera.

Third, the 4D NCAT whole-body patient phantom was modified to represent the average male and female clinical study participants. The phantoms were used in conjunction with the gamma camera model to simulate the whole-body bone scan procedure. The counts in the simulated images were consistent with the average measured counts of the clinical study indicating that it is feasible to use the NCAT phantom for nuclear medicine bone imaging. However, the phantom's method of activity distribution should be refined to allow a more realistic distribution of activity throughout the skeleton.

1. Introduction

1.1 General introduction

The early diagnosis of disease is one of the most important factors determining patient outcome [1-3]. The earlier detection of cancers that carry a high chance of metastasizing such as ovarian or malignant melanoma, or cancers that generally have a rapid progression, such as lung cancer, can lead to longer life spans and a better quality of life for the patient [4, 5]. Similarly, tumours present in organs such as the brain or pancreas may not need to metastasize or even be large before motor function or hormone production can be affected [6, 7]. Thus, an early diagnosis of disease will generally improve a patient's prognosis. Any technique or technology that can be used to improve the detection and diagnosis of a condition may be beneficial to patient care.

Nuclear medicine is the branch of medicine where patients are administered radioactive substances known as radiopharmaceuticals, in order to produce images representing the spatial distribution of the radiopharmaceutical in vivo [8]. This is in contrast to medical procedures such as x-ray, ultrasound or magnetic resonance imaging (MRI) that produce an anatomical map of the structure of the tissues or organs under investigation using external probes such as x-rays, radio waves or mechanical oscillations [9]. Thus, the results of nuclear medicine procedures emphasise the function of organs rather than their structure. This characteristic makes nuclear medicine a powerful diagnostic tool since physicians can diagnose a wide variety of pathological conditions that are

initiated by changes in the biochemistry of tissue at the cellular level, i.e. the function of a tissue or organ [10]. This is because the biochemical processes responsible for the degenerative change will also cause a change in the uptake of a radiopharmaceutical In contrast, only morphological or signal changes can be observed by external probe imaging procedures.

Since the beginning of nuclear medicine as a discipline in its own right, Monte Carlo techniques and simulation software have played a major role in solving diverse problems within the field. To date, most applications of the technique have been in a pure research environment That is, in investigating problems in detector design, image acquisition, processing and analysis. When applied correctly, Monte Carlo simulations provide a powerful and flexible method of obtaining results that cannot be measured in experiment such as scattering information. It may also be used to investigate new technology without the expense of building prototypes. However, while the techniques have been used extensively in a research environment, their use in a clinical environment has been restricted due to the time-consuming nature of the simulations. Most recently, faster Monte Carlo software and improved hardware has allowed these techniques to be implemented in a radiotherapy setting [11, 12]. However, these techniques are yet to become widespread in nuclear medicine clinics.

Models to describe human anatomy have also advanced to the point where accurate representations of organs and other large structures are available. The most advanced representations rely on techniques and tools developed for three-dimensional computer

graphics and are also able to account for changes in anatomy over time such as cardiac and respiratory motion. These models, coupled with the Monte Carlo technique are a powerful tool for researchers investigating a wide variety of issues within the nuclear medicine discipline and wider medical physics community.

1.2 Reasons for this current study

The exposure to ionising radiation is of concern to the professional or legislative bodies that provide recommendations regarding the radiation doses administered to patients undergoing medical procedures. These procedures may be a nuclear medicine scan or radiography procedure such as an x-ray. From a purely clinical perspective, the potential benefits of exposing patients to small amounts of ionizing radiation will usually outweigh the risk of first, not diagnosing the disease, and second, the risk of developing secondary cancers from the exposure to the radiation. Unlike limits for members of the public or workers whose employment requires contact with radiation, medical procedures are not subject to the dose limits imposed by the governing bodies. Instead, the As-Low-As-Reasonably-Achievable (ALARA) policy has been used in guiding the amounts of radiation used in a medical procedure to be the *minimum required* for a diagnostically valuable image to be obtained.

Currently, the activity administered to patients undergoing nuclear medicine scans are balanced against the scan time required to account for patient motion and comfort. Alternatively, the guidelines may also take into account the doses received by organs

calculated using the Medical Internal Radiation Dose committee (MIRD) stylized phantom models [13-16]. At Christchurch Hospital, the recommended amount of activity to administer to a standard adult patient undergoing a whole-body bone scan has been approximately 700 MBq [13]. Various scaling factors do exist to modify the amount of radioactivity used for scans of patients that are outside of the standard range. At Christchurch, this factor is $(\text{Weight}/70)^{2/3}$. Another set of guidelines recommend administering a further 11-13 MBq/kg for markedly obese patients designed to ensure a diagnostically viable scan [17]. For nuclear medicine scans of children, a common practice is to use the same drug scaling factors based on weight or surface area measurements [14]. These widely ranging sets of recommendations and the subsequent lack of standardization mean that it is possible that the ALARA principle is not being observed to a rigorous degree of accuracy. This has two possible consequences. First, the dose is too low, in which case the images have reduced diagnostic utility. Second, the dose is too high in which case there is an increased risk to patients of radiation induced harm.

1.3 The aims and hypotheses of the current study

The aim of this study was to investigate how counts in a whole-body bone scan image vary with patient height and weight. As the previous section stated, there is real value in administering the correct amount of activity in terms of diagnostic utility and dose minimisation. While previous studies have determined simple scaling factors to estimate how much activity to dispense to patients, no standardised set of easily applicable recommendations can be found for clinical staff to use. This study aims to use modern simulation techniques to create a framework in which this goal could be achieved.

The work in this thesis has been separated into three sections, each describing a study undertaken during the course of this project. Each section is closely related to the others but it is intended that each section can be read and understood without reference to the others. However, before the main body of work is presented, a literature review and background information pertinent to the thesis is provided in Chapter 2. This is designed to aide readers that do not have detailed knowledge in the areas of nuclear medicine, the use of Monte Carlo techniques and computational patient phantoms in medical physics research.

The first study is presented in Chapter 3. This was a clinical study undertaken in the Nuclear Medicine department of Christchurch Public Hospital. The aims of this study were two fold – first, to use actual patient data to determine the relationship between the counts detected on the Millennium MG and a patient's height and weight. The second aim was to

collect patient data to use in the validation of a computer model of the whole-body bone scan imaging procedure developed in Chapter 4 and 5.

From the results of this clinical study, the development of a more controlled environment was necessary to investigate the variation of image counts with patient anatomy. Therefore, the aim of the second study was to employ Monte Carlo techniques to design, build and validate a model of the General Electric (GE) Millennium MG gamma camera currently installed at the Nuclear Medicine department at Christchurch Public Hospital. The added advantage of this study was that since Monte Carlo techniques now account for a large number of physics research publications in nuclear medicine, a fully validated model would provide a valuable tool for future research.

The aim of the final study was to introduce the Non-Uniform-Rational-B-Splines (NURBS) computational whole-body phantom into the validated model of the Millennium MG. This was a proof of concept study to ascertain the efficacy of using the model and phantom together for clinical research, specifically simulating the whole-body bone scan procedure. The goal was to confirm that the simulation environment provides a viable alternative to the clinical study for determining the variation in detected counts with patient height and weight. Overall, it was hypothesised that this study would show that it was feasible and even desirable to move towards advanced simulating techniques and their application to real-world clinical issues.

2. Background

2.1 Scintigraphic imaging

Scintigraphic imaging is designed to produce images that represent the distribution of a radiopharmaceutical *in vivo.* These images are based on the emission of gamma ray photons from the radioactive nuclei of the radiopharmaceutical. Specifically, photons are emitted from a decaying radioactive nucleus at a point within a patient, these photons travel to the imaging equipment where they are detected and used to produce an image. The challenge for the nuclear medicine equipment is to detect and use only the correct photons to produce the image. This is because a large proportion of the photons produced at a point in the patient will be scattered via interactions within the patient. Such photons will only degrade the image if they are detected.

2.1.1 Interactions of radiation with matter

Photons emitted from a radioactive source may undergo four interactions. These are Rayleigh scattering, photoelectric interactions, Compton scattering and pair production [18].

Rayleigh (or coherent) scattering is where an incident photon of energy hυ interacts coherently with all the electrons in an atom and is scattered with no energy transferred into kinetic energy of secondary particles. The scattered photon thus has the same energy as the incident photon but now most likely directed at a different angle.

Photoelectric interactions occur when an incident photon interacts with an atom and ejects one of the bound electrons from the K, L, M or N shells. The ejected electron is called a photoelectron and possesses a kinetic energy equal to the energy of the incident photon, minus the binding energy of the shell where the photoelectron originated.

Compton (or incoherent) scattering is where a photon interacts with a shell electron of an atom causing the electron to be ejected and the photon scattered. The energy of the ejected electron depends on the energy of the incident photon and from which shell the electron was originally present. The incident photon also changes energy. Both the scattered photon and freed electron travel in directions that act to conserve energy and momentum. The spectra of scattered photons can be modelled by the Klein-Nishina equation [19-21]. The last photon interaction that may occur is pair production. This interaction is a result of a photon possessing greater than 1.022 MeV - the equivalent rest-mass energy of an electron and positron pair. A photon with greater than 1.022 MeV may interact with the Coulomb field surrounding the nucleus to produce an electron-positron pair. The electron and positron are emitted in opposite directions so that energy and momentum are conserved. The relatively large energy of 1.022 MeV required for this interaction to occur means pair production is not observed in the diagnostic nuclear medicine energy range. However, the reverse of this interaction is utilized in Positron Emission Tomography when a positron interacts with an electron to produce 2 gamma ray photons emitted at 180º that are subsequently detected and used to form an image.

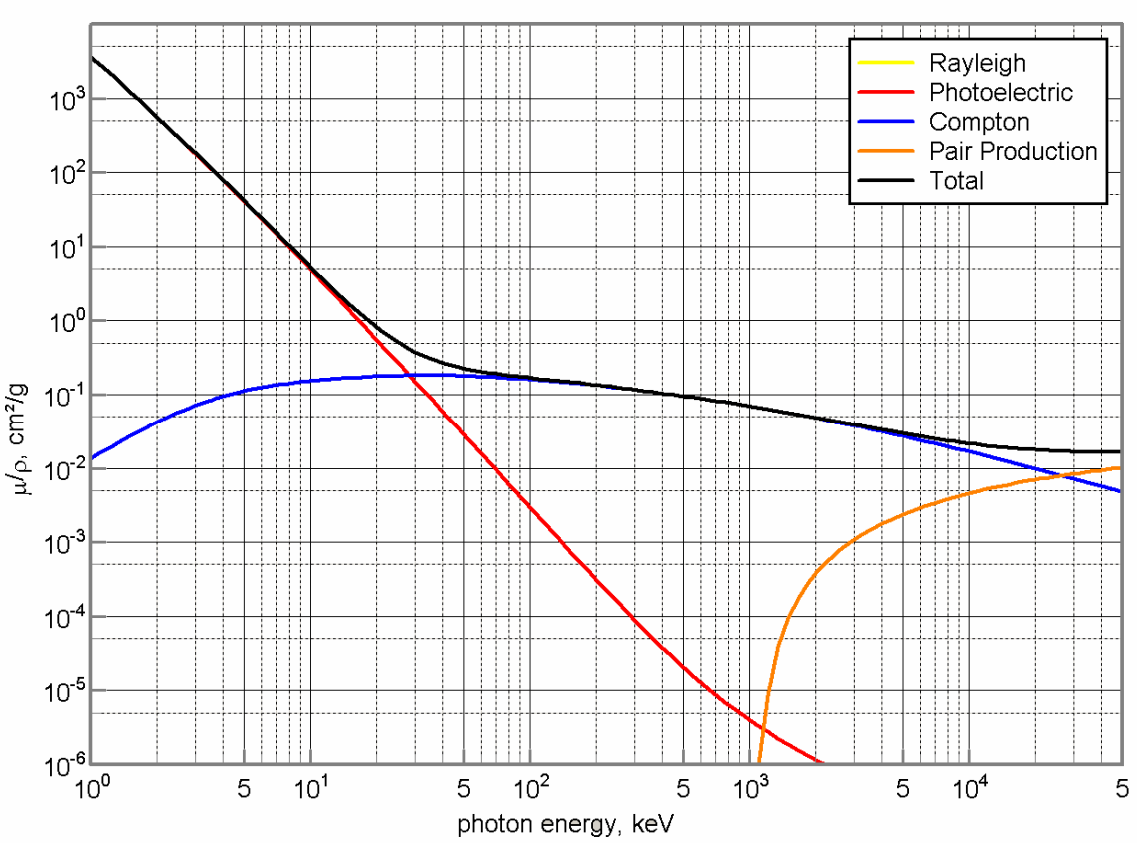

Figure 1. Attenuation coefficients for the possible photon interaction mechanisms in ICRP 44 defined soft tissue. Larger values of μ/ρ indicate an increased probability for that interaction process occurring. Compton scattering is the predominant process for the energy ranges used in diagnostic nuclear medicine. Attenuation coefficients were produced using the xmudat GUI [22].

Figure 1 shows that attenuation interaction coefficients for the four processes in soft tissue. From the 140 keV energy of the Tc-99m gamma ray emission, Figure 1 shows the two processes most relevant to nuclear medicine are photoelectric interactions and Compton scattering. The photoelectric interaction and the Compton scattering affect a nuclear medicine image in different ways. The photoelectric effect reduces the number of photons emitted from the radioactive source as they pass through tissue via attenuation.

This reduction in the number of detectable photons reduces the signal to noise ratio (SNR). To overcome this, a longer scan time are needed. Photons that have undergone Compton scattering may have a new direction of travel. If these photons are detected they will be recorded as having originated from a position in the body where they were not emitted. This results in a reduction of image contrast [9].

2.1.2 Radiopharmaceuticals

Scintigraphic imaging procedures produce images that represent the distribution of a radiopharmaceutical within a patient or phantom. A radiopharmaceutical consists of two components. The first component is a photon emitting radionuclide and the second is the pharmaceutical compound [23]. The photons emitted from the radionuclide are used for imaging while the pharmaceutical compound dictates the distribution within a patient.

Several factors must be taken into consideration when selecting a radionuclide to be used in nuclear medicine imaging. These factors are the type of radiation the radionuclide emits, the energy of the emitted radiation, the radionuclide's half-life, and its ability to form a stable bond with the pharmaceutical compound.

First, the type of radiation must be photon radiation. Alpha and beta radiation are particles, which deposit their energy locally and as a result, have a short range in tissue. This type of radiation significantly contributes to the dose received by the patient and not to the formation of an image. In contrast, photons with appropriate energies may pass through

several centimetres of human tissue before being absorbed. This increases the number of photons emitted that reach a detector, and reduces the radiation dose to the patients.

Second, the energy of the radiation is important consideration as there is a limited range of energies able to be detected reliably by current imaging equipment. The energies of diagnostically useful photons lie in the range of 70 to 200 keV [24]. Photon radiation with energy lower than 70 keV will generally not escape the patient and therefore contribute to the dose. Photons with energies higher than 200 keV can penetrate the septa of the collimator to produce artefacts in the image, or pass through the NaI(Tl) crystal without interacting and detrimentally affect the counting statistics. Medium and high-energy collimators can overcome these problems but these suffer from reduced spatial resolution and sensitivity compared to low energy collimators [25, 26].

Third, the half-life of the radionuclide must be considered. There are two components of half –life, physical and biological. The physical half-life is unique to the radionuclide and determines how the activity changes with time. The biological half-life is based on how long the radiopharmaceutical will be present in the organ of interest. This is described by the uptake and clearance rate of each organ and is dependent on the organs function. This is also known as the kinetics of the radiopharmaceutical. Together, the physical and biological half-life determines how long the radiopharmaceutical is present in the body and thus how much dose the patient receives. As such, the radionuclide should be chosen with a physical half-life that ensures enough activity is present at the time of a scan

to form an image, but which also decays away expeditiously to ensure the radiation does not significantly contribute to patient dose after the imaging procedure is completed.

The final consideration in radionuclide selection is that it should form a strong bond with its pharmaceutical compound. This ensures the photon emitting radionuclide is distributed to and within the intended organ or organs under investigation. A nuclear medicine imaging procedure becomes worthless if the radionuclide and pharmaceutical have separated at the time of imaging. The main radiopharmaceuticals used for bone scans and thus relevant to this study are Tc-99m labelled diphosphonates. Figure 2 shows the molecular structure of the two most common varieties of phosphate radiopharmaceuticals. These are methylene-diphosphonate (MDP) or hydroxymethylene diphosphonate (HDP or HMDP) The phosphate component of the radiopharmaceuticals displays an affinity for the metabolically active bone mineral hydroxyapatite, resulting in the uptake and kinetic behaviour of the compound in active regions of the skeleton [10]. The oxygen components of the radiopharmaceutical are the actual part of the pharmaceutical that bind to the calcium of the bone surface [27]. The bidentate or tridentate component of the MDP or HMDP is where the reduced form of Tc-99m is attached to the molecule.

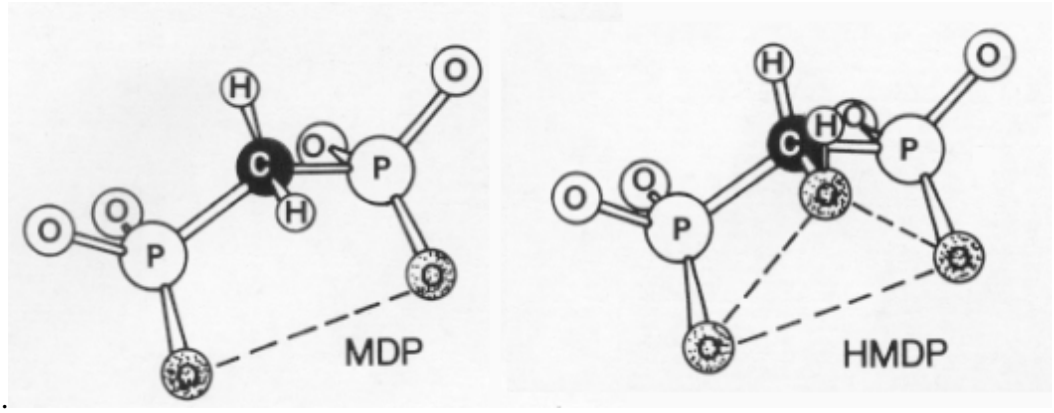

Figure 2. The structures of methylene diphosphonates (MDP) and hydroxymethylene diphosphonate (HMDP). The reduced Tc-99m attached to the bidentate or tridentate part of the molecule (shown as the shaded oxygen atoms and dashed line in the figure).

One radionuclide that fulfils all of the above criteria is Technetium 99m (Tc-99m). First, the Tc-99m radionuclide emits 140.5 keV photons. These photons are attenuated 50% in a thickness of 4.6 cm of human tissue and are therefore able to escape the patient and be detected. Second, the physical half-life of Tc-99m is 6.02 hours. This ensures that patient dose is kept to a reasonable level. The method of producing Tc-99m is also straightforward. Tc-99m is extracting from the secular equilibrium it exists in with its parent nucleus, Molybdenum 99 (Mo-99). The Mo-99 nucleus undergoes β^- decay:

$$^{99}Mo \rightarrow {}^{99}Tc^{m} + e^{-} + \bar{\upsilon} \qquad [28]$$

Mo-99m generators or 'cows' are usually delivered to a hospital at the beginning of a week. Staff then 'milk' the generator by washing the internal column with saline to produce the sodium pertechnetate complex ($Na^{99m}TcO_4^-$). This complex is then attached to a pharmaceutical appropriate to the organ of interest. However, the complex may be used

directly for quality assurance (QA) measurements or imaging. For these reasons, Tc-99m is used in 85-90% of all nuclear medicine scans [18, 29, 30].

2.2 Assessment of image quality

The quality of any image produced by detectors will determine how useful the image is in diagnosing an illness or condition. Image quality can be described by the parameters of contrast, noise and spatial resolution. Usually, there is a compromise between the three. In other words, the optimisation of one parameter detrimentally affects one or both of the others.

2.2.1 Contrast

The contrast of an image is the difference in image intensity or grey scale in the image. A uniformly grey image has no contrast, whereas an image with vivid transitions between dark grey and light grey demonstrates high contrast. In nuclear medicine, the contrast arises from the difference in radiopharmaceutical uptake between organs and the surrounding tissue. Planar imaging represents a 2D projection of a 3D radiopharmaceutical distribution so the image contrast is affected by the presence of activity in overlapping structures. With SPECT or PET images, a higher contrast can be obtained since the contribution of the activity in overlying structures is removed. Contrast is also affected by attenuation, scatter, background radiation and septal penetration of the primary photons from the radionuclide. A basic equation that determines the contrast (C) in a region of interest is

$$C = \frac{|N - B|}{|N + B|} \cdot 100\% \qquad [28]$$

Where N is the average number of counts in each pixel of the region of interest (ROI) and B is the average value of counts in a surrounding background region.

2.2.2 Spatial resolution

The spatial resolution is the ability of an imaging system to distinctly depict two objects as they become smaller and closer together [31]. The closer together the objects are, with the image still showing them as separate objects, the better the spatial resolution. At the point where the two objects become so close they appear as one, spatial resolution is lost. Nuclear medicine imaging systems typically have lower spatial resolutions than other imaging modalities such as X-ray radiography or MRI. This is because the spatial resolution in a nuclear medicine scan is dependent on the intrinsic resolution of the NaI(Tl) crystal and PMT combination, the geometric resolution of the collimator, and further losses due to scatter and septal penetration. The best spatial resolution of a scintigraphic image is achieved using a LEHR collimator. This is because the LEHR collimator has a longer hole or septal-length which rejects more photons that are not travelling directly perpendicular to the crystal face. However, this higher spatial resolution comes at the cost of reduced sensitivity and lower signal to noise ratios since there is a reduced number of photons reaching the detector.

2.2.3 Noise

An image may have good contrast and spatial resolution, but if the noise in an image is high, then the ability to distinguish objects from the background may be difficult.

In nuclear medicine, the value of a pixel image is the integral of gamma-ray events in that pixel position over time. Thus, every pixel on a nuclear medicine image can be regarded as a photon counter. If a photon is detected and accepted by the gamma camera, a count will be added to the pixel position the count is recorded in. There are two major contributions to noise in a nuclear medicine image. The first is statistical fluctuations in the number of gamma-ray photons detected per pixel. This is also known as 'quantum noise' and is caused by the random radioactive decay of the source. The second contribution is not an increase in noise, but a reduction in the signal to noise ratio (SNR) due to the physical properties of the actual imaging and display system. Fluctuations due to collimator and amplification effects from the PMTs both reduce the number of photons available to form an image. This reduces the signal to noise ratio in the image making it more difficult to reliably identify an object in an image.

Nuclear medicine images display high levels of noise compared to other imaging modalities such as x-rays due to the lower flux of photons incident on the detector in a given time. The flux is reduced for two main reasons. First, only a limited amount of radioactive material can be administered to the patient because of dose concerns. Second, the collimator only lets through around 0.1% of the total number of photons incident on the collimator face. The combined effect of these two factors mean a typical nuclear medicine scan is a lengthy procedure as sufficient counts must be detected to achieve an adequate SNR ensuring the scan is diagnostically valuable.

2.3 The gamma camera

2.3.1 Development and features

The detector used for the majority of all nuclear medicine procedures is the gamma, or Anger camera. It was developed by Hal Anger in the late 1950's [32] and despite improvements in its performance due to advances in digital electronics and multiple detector systems, the basic components are largely unchanged [30]. The gamma camera consists of a collimator, material that the gamma-ray photons emitted from a radioactive source interact with, and components used to convert the energy from the gamma radiation into a useable signal to produce an image. A basic outline is shown below in Figure 3 (used with permission - Larsson, 2005)

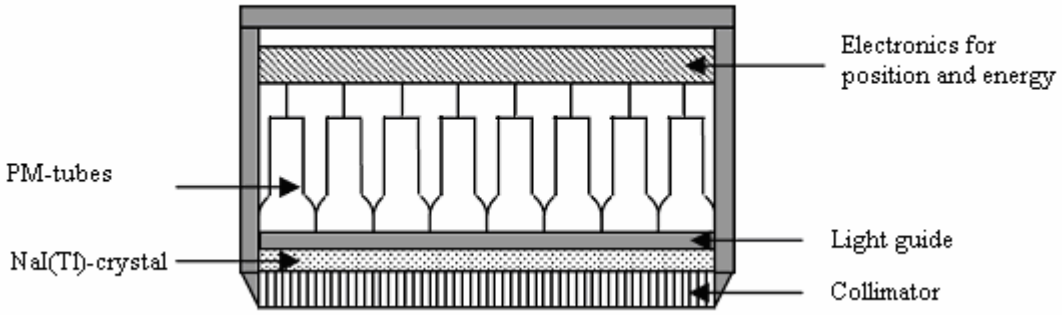

Figure 3. Simplified schematic of a modern gamma camera. The main components are outlined on the figure.

The collimator is a configuration of closely arranged holes separated by thin septa constructed using a dense, high atomic number material - usually lead. The collimator is designed to allow only gamma or x-ray photons that are travelling perpendicular to the crystal face to be used in image formation. This excludes many photons that have

undergone scattering events, but dramatically reduces the number of photons that can be used to form an image since approximately 1 in 10,000 photons able to pass through the septa [25]. The diameter and separation of the holes throughout the lead collimator also determine the achievable spatial resolution of an image.

There are many types of collimators available for different types of nuclear medicine scan. The most common is the parallel hole collimator [33]. There are also converging, diverging and pinhole collimators. Most gamma cameras are provided with different parallel hole collimators such as low-energy general purpose (LEGP), low-energy high resolution (LEHR) and medium-energy high sensitivity (MEHS). All are designed to produce the best possible image depending on the photon energy emitted by a radionuclide or the imaging procedure being performed.

The majority of gamma cameras use sodium iodide crystals that have been doped with thallium, NaI(Tl), as the material the gamma ray photons interact with [34]. NaI(Tl) is a scintillating material that emits light photons with an intensity proportional to the energy of the incident gamma radiation. NaI(Tl) is also highly optically transparent with near 100% light transmission efficiency [35]. This means the light photons produced in the crystal can travel be detected by an array of photomultiplier tubes (PMT) with little loss of intensity due to attenuation within the crystal. The crystal thickness in modern gamma cameras is between 0.9 and 1 cm and is an important parameter because it affects the amount of spreading out or ‘blurring’ in the signal arising from the light photons. Absorption or activation events and scattering interactions that occur within the crystal

cause the signal to spread out which reduces the spatial resolution of the imaging system. Generally, this means that the thicker the crystal, the greater the blurring effect is. However, the use of a thin crystal means that more incident photons will pass through the scintillation material without interacting. These potentially useful photons are then lost, causing a reduction in signal and the corresponding counting statistics.

The conversion from photon detection events into a useable signal is done via the use of photomultiplier tubes (PMTs). The PMTs convert the light signal from the NaI(Tl) crystal into an electrical signal that can be measured by the internal electronics of the gamma camera. This electrical signal is used to determine the position of a gamma ray detection event and the energy of the gamma photon. When a photon originating from a point P passes through the collimator it produces a scintillation event in the crystal. The X and Y coordinate of the scintillation on the crystal face is the same as the X and Y coordinate of the point P. The X and Y coordinates are determined by analysing the intensity of the flash of light detected by the PMT via the internal electronic circuits (Figure 4).

The energy of a gamma ray photon is determined via the fact that the intensity of the light detected by the PMTs is proportional to the energy of the incident photon. Scattered photons cause there to be a spectrum of energies incident on the detector. A method of discriminating against these photons is required since they only act to degrade the image. The internal electronics of the camera may be used to set a range of energies that the camera accepts in order to form an image. This range of energies is known as the

energy window. For nuclear medicine imaging using Tc-99m it is most common to use a 20% energy window centred on 140 keV. This means the camera will detect only photons with incident energies of 126-154 keV.

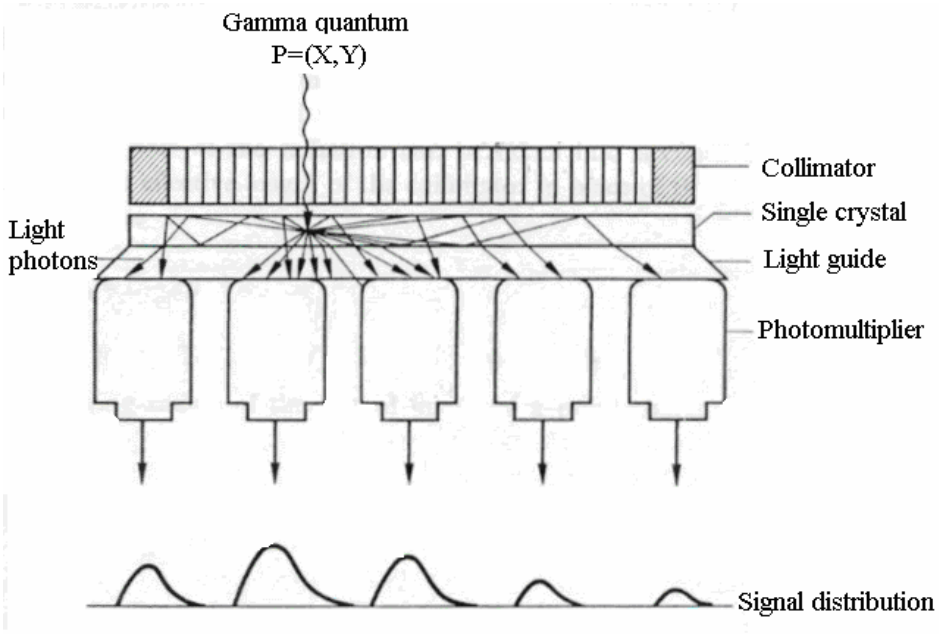

Figure 4. Spatial discrimination principle for the gamma camera. The intensity of light photons detected by the PMTs is used to isolate the position of the gamma ray interaction site in the NaI(Tl) crystal.

Gamma cameras may possess a single or multiple detectors and these may be stationary or rotate around the patient. With stationary detectors, the images produced are a 2-dimensional representation of the 3-dimensional distribution of the radiopharmaceutical within a patient. For a whole-body bone scan, it is common for two detectors to acquire the anterior and posterior projections simultaneously. With one or more detectors rotating through many projection angles, a 3-dimensional image can be produced after the projections at each angle are reconstructed. This mode of operation is called Single Photon

Emission Computed Tomography (SPECT). A 3-dimensional image may also be produced by using a ring of stationary detectors as is done with certain positron emitting radionuclides in Positron Emission Tomography (PET) imaging. However, both SPECT and PET are not involved in the current study and will not be discussed further.

2.3.2 Performance characteristics

Energy Resolution

The energy resolution of a gamma camera is a measure of its ability to distinguish between interactions depositing different energies in its crystal [9]. Energy resolution is a measure of how good the detector is at discriminating between primary and scattered photons. It is calculated as:

$$R_E = \frac{FWHM}{E_0} \qquad [36]$$

Where FWHM is the full width at half maximum of the photo-peak energy window and E_0 is the average energy of the photo-peak. Values for modern gamma cameras have energy resolutions of 8-10% for the 140 keV photons of Tc-99m [37]. A better energy resolution means an increased separation between the energies of photo-peak window and Compton region which mean we can detect primary photons (those that have not undergone scatter) preferentially over scattered photons. In any case, the energy resolution used should provide good scatter rejection but maintain an adequate sensitivity. With a

wider energy window or large energy resolution more photons can be detected, increasing the sensitivity, but at the expense of detecting more scattered photons.

Sensitivity

The sensitivity of a gamma camera is a measure of the number of photons detected relative to the number emitted from the source in a given amount of time. The units are counts per second per megabequerel (CPS/MBq). The sensitivity must be known for an accurate quantification of activity. The factors affecting the sensitivity of a nuclear medicine system are the collimator, the crystal thickness, the energy of the incident gamma ray photons and the width of the energy window. The collimator has the greatest effect on the sensitivity because it is the part of the gamma camera that rejects the largest number of photons that reach the detector by discriminating by incident angle. Increasing the diameter of the holes will increase the number of photons and decrease image noise, but this decreases the achievable spatial resolution.

The crystal thickness and energy will determine the number of photons that interact to produce light photons for detection. The energy of the gamma-ray photons will dictate how far into the NaI(Tl) crystal they penetrate before interacting. Thicker crystals will let higher energy photons interact but light photons from the lower energy photons will undergo a blurring effect reducing the spatial resolution of the image [38-40].

Finally, the width of the energy window used to discriminate against scattered photons is also a factor in determining the number of photons that are detected. A narrow

energy window will only accept photons close to the midpoint of the photo-peak energy window. However, this reduces the number of legitimate photons that can contribute to the image. Widening the energy window allows more photons to be detected to produce an image, but this widening will also increase the number of scattered photons that will be accepted. These scattered photons will degrade the contrast of the image.

Count rates

The count rate performance is the ability of the imaging system to record the true count rate, which is the number of detected photons per time within the energy window [24]. Every photon can contribute to the total light yield detected by the PMTs. Furthermore, the light produced in the NaI(Tl) crystal from a gamma-ray photon exists as 'glow' for a finite time; typically around 230 ns [35]. There is also electronic dead time with the PMTs and electronic circuits.

Count rate performance is measured as the maximum observed count rate, and the count rate at 20% losses [36]. Large variations exist between different gamma cameras but values taken from a GE Millennium MG camera as used in this study by other researchers have found the maximum count rate in a 15% energy window to be ≥220 000 cps and the value at 20% losses to be ≥155 000 cps [24]. Thus, with a high activity (large numbers of decays per second) from a radionuclide, the detected count rate may be less than the true count rate and the energy of any one event may be detected incorrectly. Corrections can be performed for count rates above 100 000 cps [41, 42].

2.3.3 The Millennium MG gamma camera

The gamma camera specific to this work is the General Electric (GE) Millennium MG multi-purpose dual-headed camera (Figure 5). It is one of two gamma cameras in the Nuclear Medicine department, the other being a Siemens e.cam Variable Angle gamma camera.

Figure 5. The GE Millennium MG Dual Headed Gamma Camera in place at the Nuclear Medicine Department at Christchurch Hospital. Detector 1 is the top detector. The patient bed has been extended over the face of detector 2 and the IEC count rate performance in scatter phantom positioned on it.

The Millennium MG is used almost exclusively for bone scans within the department. For whole-body bone scans, the Millennium MG camera is equipped with a Multi-Purpose Rectangular (MPR), low-energy high-resolution (LEHR) collimator. The

dimensions of this collimator were taken from documents provided from the manufacturer (Table 1).

Table 1. Collimator data for the GE Millennium MG used in this study

	Septal thickness (mm)	*Hole diameter (mm)*	*Hole length (mm)*	*Energy at 5% penetration*	*System Resolution (mm)*
LEHR	*1.2*	*3.0*	*42*	*176*	*7.9*

For all the experiments undertaken in this work, the count rates measured on the camera were below 50,000 counts per second (cps) which is below the pile up region for the Millennium MG camera. This effectively means all counts produced by the source are recorded by the camera and pile up effects can be ignored [24].

2.4 Monte Carlo techniques in nuclear medicine

The term Monte Carlo refers to the sampling of random numbers to solve problems that can be based on probability distributions of the underlying processes involved [43, 44]. The technique has historical use in calculating a numerical value of π and in solving indefinite integrals [45]. However, the modern era of Monte Carlo may be attributed to von Neumann and Ulam - physicists working on the Manhattan Project calculations in the effort to create the atomic bomb [46]. They coined the term Monte Carlo method in their calculations of neutron transport.

The 'golden age' of the Monte Carlo technique was ushered in with the introduction of the digital computer. In particle physics, the simulation of charged particle transport required extremely long computing times compared to those involving neutral particles and photons. This is due to the greater number of interactions required by these particles to lose their initial energy. With the introduction of the condensed history technique by Berger in 1960 [47], charged particle transport simulations using the Monte Carlo method could now be accomplished in reasonable time frames [48]. Berger's technique was known as the Electron Transport (ETRAN) algorithm and was introduced into the first modern day Monte Carlo codes. These codes were used mostly in calculating detector responses and material stopping powers [28, 49-55].

Since then, Monte Carlo techniques have been used in many fields in medical and radiation physics [44]. In nuclear medicine, the use of Monte Carlo software has been used

extensively. Such applications include the design of apparatus used in a clinical setting [25, 56-59], the acquisition of images [60], and furthermore, the post processing of the images attained in order to increase the chance of correctly identifying the disease [61, 62]. More complicated algorithms have been implemented to improve the speed and accuracy of the simulations.

Monte Carlo codes can be divided into two categories, general purpose and user specific. General purpose codes tend to have a large user base and thus be well documented and validated for many purposes and energy ranges. Examples of such codes are the Electron-Gamma-Shower (EGS), Monte Carlo Neutron Particle (MCNP) and GEometry ANd Tracking (GEANT). Alternatively, specific codes usually utilise simplified situations to investigate well-defined problems. Many only deal with one type of particle such as gamma photons, or fixed geometries. Specific codes may not be as well supported nor have benefited from extensive validation as the larger general codes. However, specific codes are generally faster and simpler to implement. A few examples of the many specific codes available are SIMulation of Imaging Nuclear Detectors (SIMIND) [63], Simulation System for Emission Tomography (SimSET) [64], and PENetration and Energy LOss of Positrons and Electrons (PENELOPE) [65]. The SIMIND code is the Monte Carlo simulation software used in this work.

2.4.1 SIMIND

The Monte Carlo simulation code, SIMIND, describes a standard clinical single detector SPECT camera and can easily be modified for almost any type of calculation or measurement encountered in SPECT imaging. The SIMIND code has been developed by Professor Michael Ljungberg of the Medical Radiation Physics section of the Department of Clinical Sciences at Lund University, Sweden. The entire code is written in FORTRAN-90 and includes versions that are fully operational on Linux systems (x86), and on Windows (x86). The SIMIND system has two main programs, named CHANGE and SIMIND. The CHANGE program provides a way of defining the system to be simulated and writing data to external data files. The actual Monte Carlo simulation is performed by the program SIMIND that reads input files created by CHANGE and outputs results to the screen and to various data files. In this way, several input files can be prepared and loaded into a command file for submission to a batch queue, a convenient way of working since Monte Carlo simulations by default are time consuming [63]. After the simulation, information from the saved image and energy spectra binary files can be extracted and saved using the Binary Image Matrix (BIM) and Binary Image Spectra (BIS) utilities that are included in the SIMIND distribution.

SIMIND was chosen for this work for several reasons. First, the software is purposely designed to model planar imaging systems for planar and SPECT scintigraphic imaging which is the equipment present in the Nuclear Medicine department at Christchurch Hospital. Second, the CHANGE program has a graphical user interface

(GUI). A GUI provides an easy and efficient way of defining and modifying an accurate model of the GE Millennium MG before a simulation is started. A GUI is also more user friendly to clinical staff and future researchers. Third, the code is fast - it makes use of several advanced variance reduction techniques and does not model any electron transport. Any electrons produced by physical processes within the model are terminated at their point of origin. Testing and validation has shown that ignoring electrons does not detrimentally effect the accuracy of the simulations [66-68]. Ultimately, the speed of the code allows large numbers of photon histories to be simulated and therefore, accurate statistics to be extracted from the results. Finally, the software allows the introduction of very complicated non-homogeneous phantoms. This is a major requirement for the accomplishment of this work. Previous studies have used SIMIND in conjunction with the Zubal head and full body phantom [69] and the NCAT cardiac phantom [47]. It is also fully compatible with the Radiological Support Devices (RSD) series of phantoms [70] and the Mathematical CArdiac and Torso (MCAT) phantom. The software also has the ability to read in user defined density maps derived from CT scans [63]. Thus, an enormous flexibility is contained in the software for many types of phantom simulation.

2.5 Computational anthropomorphic phantoms

In all fields of medical physics, there is a need for models of human anatomy. Phantoms for radiological use were introduced as early as 1910 while phantoms in the field of radiation protection began to undergo evolution in the 1950s [71].

Computational anthropomorphic phantoms are computer models of human anatomy. The phantoms are divided into two classes, analytical or stylized, and voxel based or tomographic. Analytical phantoms describe the shapes of the human body including its internal organs via combinations of mathematical equations that describe plane, cylindrical, conical, elliptical and spherical surfaces. The first such analytical computational phantom was a 30 cm thick slab, closely followed by a solid cylindrical phantom. Both were used extensively for investigating neutron interactions in tissue like materials for dose calculations [72]. In 1960, a phantom was constructed by Hayes and Brucer to resemble the human body [73]. The Medical Internal Radiation Dose (MIRD) committee requested an extension and refinement to the Hayes-Brucer phantom and the result was the Fisher and Snyder model (Figure 6). This phantom was used to calculate the dose to organs of patients from the administration of radiopharmaceuticals.

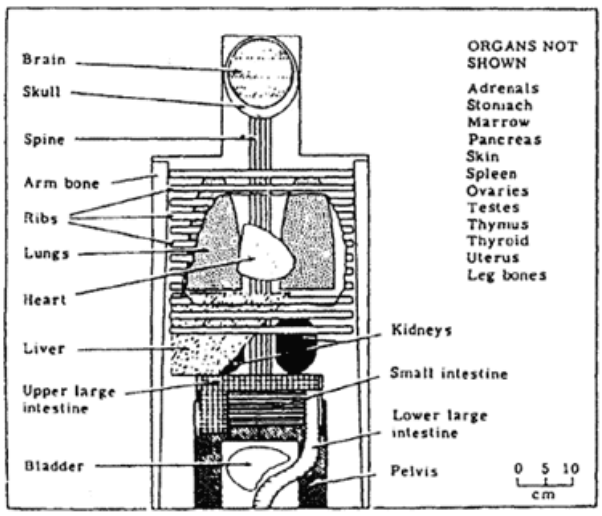

Fig. B.9. (a) Disposition of organs in human phantom of Snyder *et al.* (1969). This shows the anterior view of principal organs in head and trunk of phantom.

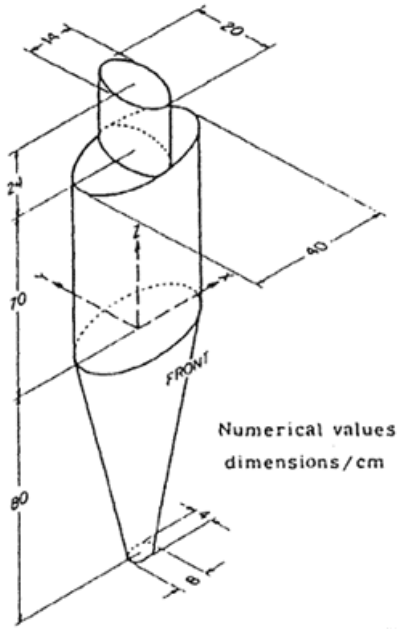

Figure 6. The original Fisher-Synder MIRD reference man computational phantom. This phantom was used to derived the dose factors (DF's) for organs under a variety of nuclear medicine procedures [74].

In contrast, tomographic or voxel based phantoms are derived from computed tomography (CT) or MRI images of real human subjects. The organs and tissues must be segmented from the two-dimensional slices. These 2D-images are then stacked to produce a three-dimensional voxel matrix with each voxel having an assigned density and identity. Since these phantoms are based on real human anatomy, they are able to more realistically describe human anatomy than analytical phantoms. The first voxel-based phantom was based on X-ray Computed Tomography (CT) scans of the torso and head of a female cadaver [75]. Soon after, another voxel-based phantom was developed to construct an 8-week old female baby and 7 year old female child [76]. A more complete phantom was

developed by Zubal et al. where a head to mid-thigh CT scan of a patient with diffuse melanoma was developed [77]. This phantom had 35 organs and tissues segmented. The phantom was subsequently extended to include the head using magnetic resonance (MR) images of a 35-year-old male, and arms and legs from the Visible Human data set from the US National Library of Medicine (Figure 7).

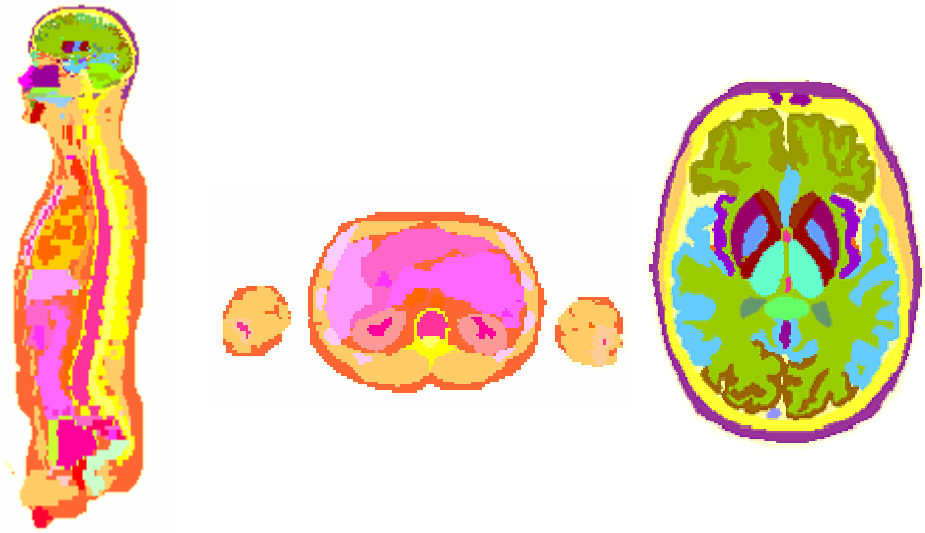

Figure 7. The Zubal phantom. (Left) Sagittal slice through the torso of the phantom. (Middle and Right) Transverse slices of the torso and head respectively. Voxel based phantoms display a greater level of detail but at the expense of flexibility [78].

Most recently, advances in the fields of computer graphics and computer-aided design have crossed over into the development of anthropomorphic phantoms. The most widely used phantom of this sort is the NCAT phantom. This was the patient model chosen to be used in this study.

2.5.1 The NCAT phantom

Non-rational uniform B splines (NURBS) are used extensively in 3D computer graphics to model three-dimensional surfaces [79]. The latest version of the NURBS Cardiac And Torso phantom (NCAT) is a realistic and flexible model of the entire body and internal organs.

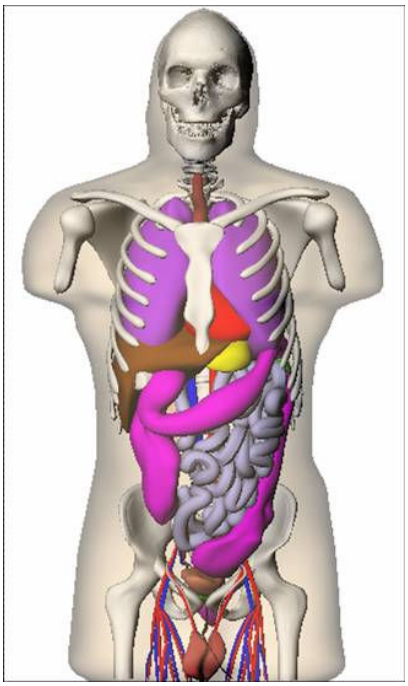

Figure 8. The NCAT male torso phantom: NURBS are used to define realistic organs surfaces. These NURBS may be changed to model a large variety of patient sizes. In addition to the male torso, female, infant and fetus whole body phantoms have been developed for dosimetry and imaging research [80].

Surfaces within the phantom are defined by NURBS equations giving users the ability to modify the size and shape of any organ desired. Time-position and time-activity curves are also able to be defined to allow the description of respiratory and cardiac motion and the varying activity in an organ with respect to time. The NURBS equations mean the

NCAT phantom can be modified in both spatial and temporal dimensions so that four-dimensional (4D) studies may be performed more efficiently and accurately. This is a major step forward in the modelling of human anatomy. The flexibility extends further as the phantom can be made into any resolution that is required. This is in contrast to other tomographic phantoms such as the Zubal phantom, where it may only be possible to define one or two resolutions. Phantom resolution is an important factor in the accuracy of Monte Carlo simulations because the higher the resolution, the closer the model is the real human anatomy Therefore, the NCAT phantom can be described as being both an analytical *and* a voxel based phantom. The phantom is analytical in the sense that organs shapes may be altered using the NURBS equations much like the original analytical phantoms could be altered by changing the equations spheres, ellipse or rectangles while it is a voxel based phantom since the organs may be changed into smaller volumes to input into Monte Carlo simulations However, while the phantom combines the advantages from both types of phantom but has the disadvantage of an increased complexity in how the surfaces are defined. NURBS surfaces are difficult to visualize and special software is required to change the geometry [81]. Some of the many areas the phantom has been used in the medical physics community to date include CT imaging [82-84], cardiac imaging and gating [85, 86], SPECT acquisitions [87-89] and dosimetry calculations [90].

2.6 The whole-body bone scan

The focus of this study was the clinical whole-body bone scan. Bone scans are the most common type of nuclear medicine scan performed in the Nuclear Medicine department at Christchurch Hospital and around the world [91]. The bone scan is a particularly sensitive modality for detecting regions of bone that exhibit increased metabolic activity. Such regions of the skeleton may be indicative of the presence of cancer since a normal response is to form new bone at the site or periphery of a tumour [10]. Regions of bone that show a void in the signal of the nuclear medicine scan are also indicative of bone infarctions or aggressive bone metastases. This is because such conditions are characterised by a lack of blood flow meaning the radiopharmaceutical is not delivered to the region. Bone scans are also used in the diagnosis of bone fractures and infections, Paget's disease and other degenerative changes that may cause an increased uptake of radiopharmaceutical within the skeleton [92].

Each clinic will have its own in-house protocol for performing whole-body bone scans since no clinic contains the same equipment and staff. However, all patients undergoing a whole-body bone scan in the Nuclear Medicine Department and Christchurch Hospital are imaged using the following procedure:

- Fully extend the bed. The top of the patient's head should be included in the field of view (FOV) with their feet, no further than the end of the bed extension.
- Ensure the camera detector heads are at 0 and 180 and the bed is centered.
- Raise the bed and bring both camera heads as close to the patient as possible.
- View: Anterior Detector 1/ Posterior Detector 2
- Matrix: 256 x 1024
- Time: 10 minutes per metre
- Length: Max. 1.94 m.
- Use of low-energy high-resolution collimators
- 20 % energy window centred at 140 keV
- Proper patient positioning to ensure comfort and reduction in patient movement to reduce motion artefacts
- Patient voids just before acquisition begins to reduce the effect bladder activity has on the scan
- 700 MBq HDP-Tc-99m should be administered.[93]

Unusual or exceptional clinical circumstances may require modifications to the guidelines such as modifying the amount of activity administered for children or obese patients, or the use of a couch extension for taller patients. In all cases, the goal of the procedure is to produce a high quality and diagnostically valuable image while minimising patient dose.

3. Whole-body bone scan clinical study to investigate the variation of image counts with patient anatomy

3.1 Introduction

The aims of this study were two-fold. The first aim was to determine whether there is a relationship between patient height and weight and the counts registered in the whole-body bone scan images output by the Millennium MG. We anticipated that a computer model would be required to determine the relationship and so our second aim was to use the patient data in the validation of this model. The development of this computer model is outlined in later chapters. The determination of a relationship, if it exists, is an important step in the optimisation of the clinical protocols as it would allow the expected number of counts in an image for any individual patient to be predicted. For example, if a range of patient sizes is found to result in images that contain a number of counts that are too low, then the activity administered to these patients would need to be increased. The opposite case is also true, with too many counts the recommended patient dose may have been exceeded thus necessitating the reduction in administered activity. By determining a relationship, we may be able to optimise the clinical protocol for individual patients. If no obvious relationship is able to be determined or there are other parameters that are found to have a significant influence, it would be necessary to undertake another approach.

3.2 Method

3.2.1 Subjects

This study received ethics committee approval from both the Ministry of Health Upper South Regional Committee and the University of Canterbury Human Ethics Committee.

The participants for the study were those that would normally undergo a whole-body bone scan as a diagnostic procedure. In total 65 patients were recruited to be participants in this study – 28 males and 37 females. Upon arrival to the Nuclear Medicine Department, informed consent was sought from the participants. If this was given, their height and weight was recorded in centimetres and kilograms, respectively. The age (measured in years) and the sex of each participant was also recorded. It should be noted that although the Body Mass Index (BMI) is the standard measure of patient size in the literature, this study was designed to see what the relationship is between the two separated variables. Furthermore, the patient BMI is able to be determined easily from our data, even though we have not done so expressly.

The dispensed activity of the Tc-99m labelled HDP or HMDP, the time of dispensing, time of injection and time of the scan was recorded to correct for the physical decay and biological clearance of the radiopharmaceutical. After review by a nuclear medicine specialist, only those scans reported as being normal or near normal were included for analysis.

3.2.2 Extracting and normalising the image counts

The total counts in the anterior and posterior projection images for each patient were calculated using the ImageJ image analysis software [94]. To do so, ImageJ uses a parameter called the 'Integrated Density' to calculate the number of counts in an ROI within an image. This parameter is equal to the area of the ROI multiplied by the mean value of the pixels within the ROI. Based on the information in the DICOM file header, the pixel size is 2.26 x 2.26 mm^2 which necessitates the use of an area correction term equal to $(2.26)^{-2}$. Multiplying the integrated density by the area correction term results in values of counts in the image identical to those calculated using the Millennium MG Xeleris processing workstation.

In addition to calculating the counts in the anterior and posterior projection images, the counts from the contents of the bladder were excluded by drawing a second ROI around the bladder of each patient's bone scan projection image. The counts in the bladder ROI were then subtracted from the counts of the total image. As a measure of consistency in the ROI drawing, one patient image was selected and the bladder ROI defined multiple times. The variation in the counts within the ROI was found to be less than 5%. The bladder is usually excluded in the image reporting in the nuclear medicine clinic but the main advantage of doing so in this study was that the counts in each image could be normalised using the activity in each patient *at the time of their scan* using the ICRP reference kinetic data as this data excludes bladder contents. This parameter was selected

because it is only the activity present within the patient at the time of their scan that contributes to the counts detected by the gamma camera.

To estimate this activity, the ICRP kinetic data for the normal uptake and clearance of phosphate based bone-imaging radiopharmaceuticals (Table 2) was used as a reference to derive time-activity curves for the amount of activity in both the skeleton and the body tissue. The time-activity curve representing the relative activity within the entire body and skeleton is displayed in Figure 9. The model has foundations in the calculation of cumulated activity to determine the dose to an organ from radiopharmaceuticals that have non-instantaneous uptake and clearance through physical and biological mechanisms [95]. The activity in each patient at the beginning of their bone scan was estimated by using the amount of activity administered to the patient and the time delay between injection and scan start time in the time-activity curve equation. This value of activity was then used to normalise the counts in the anterior and posterior image for each patient to find counts in units of counts per MBq.

Table 2. ICRP reference kinetic data used to estimate total activity within patients at the time of the whole-body bone scan. F_s = fractional distribution to organ over all time, if there was no radioactive decay. T = biological half-time. a = fraction of F_s eliminated or taken up in an organ or tissue. A_s/A_0 = cumulated activity over activity administered – measure of total decays in organ or tissue [96].

Organs (S)	F_s	T	a	A_s/A_0
Normal uptake and excretion	1.0	0.5 hr	0.3	4.06 hr
Total body (excluding bladder contents)				
		2 hr	0.3	
		3 d	0.4	
Bone	0.5	0.25 hr	-1.0	3.01 hr
		2 hr	0.3	
		3 d	0.7	
Kidneys	0.02	0.5 hr	0.3	7.5 min
		2 hr	0.3	
		3 d	0.4	
Bladder contents	1.0			1.15 hr

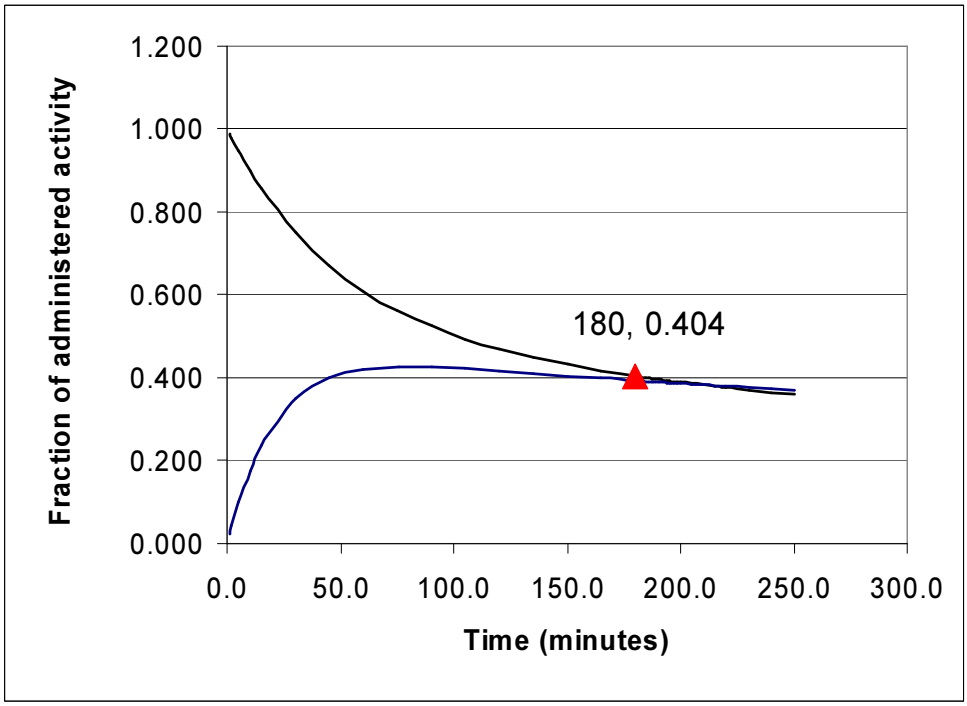

Figure 9. Sample kinetic data of Tc-99m HDP. The lines correspond to the body kinetics (black) and bone kinetics (blue).The point on the curves is the recommended 3 hour delay between the administration and imaging. At this point 40% of the initially administered activity remains.

3.2.3 Data Analysis

The attempt to determine the relationship involved three stages. First, the mean, standard deviation and minimum and maximum values for each of the measured variables was calculated. This was to give information about the distribution of parameters and to determine whether the Christchurch hospital clinical guidelines (Chapter 2.6) were being adhered to.

Second, the correlation coefficients together with their statistical significance of each of the variables were found using the 'corr' function in MATLAB. A p-value of 0.01 was used to judge whether a correlation was significant or not. It should be noted that the correlation of a particular explanatory variable with the response variable does not achieve statistical significance does not necessarily imply that it will not be a useful predictor in the multiple regression [97]. However, the process does provide a means to better understand any relationships that may be nested within the data.

Finally, a multivariate linear regression was performed to determine the overall relationship between the measured variables to see if the best fit to the data was a relationship between image counts and patient anatomy or whether other factors were a significant influence on the image counts.

3.2.4 Multivariate linear regression

Multivariate linear regression is a method of fitting measured data to a function in such a way that the discrepancy between the measured values and calculated values is minimised. The fitting is based on the hypothesis that the optimum description of a data set is one that minimises the weighted sum of the squares of the deviation of the data y_i from the fitting function $y(x_i)$ [98]. That is, given a function

$$\hat{y}_i = b_0 + b_1 x_{i1} + b_2 x_{i2} + \ldots + b_p x_{ip}$$

that has been fitted to the measured data y_i, the regression acts to minimise the quantity

$$\sum (y_i - b_0 - b_1 x_{i1} - b_2 x_{i2} - \ldots - b_p x_{ip})^2$$

Where y_i is the measured counts from subject i, x_{i1} = weight, x_{i2} = height etc. The second stage was to perform the regression. Our primary interest is with the variation of patient height and weight and subsequently detected counts in the image. However, since we also have data available for patient age and sex, we can see if there are any underlying effects due to these variables. What complicates the situation is that the variables of normalised counts, age, sex, weight and height may be used to create many possible relationships. Therefore, we require a method of determining the most parsimonious combination of the variables. In other words, we wish to find the model that can account for the most variance between the measured normalised counts and the normalised counts predicted by the linear regression model, but which also uses the least number of variables to do so. One such statistical technique that provides such information is the “Akaike Information Criteria” or

AIC. The AIC is a measure of the goodness of fit of an estimated statistical model in which the measure of a fit is also dependent on the complexity of an estimated model. In other words, although the addition of suitable variables to the model will increase the model's ability to account for any variance between the model and measured data, there is a measure of 'punishment' for the increase in complexity. There is no standardised reference value to compare the AIC of different data sets unlike such measures of fit as the R^2 or χ^2 parameters. However, for any given data set, the lower value of the AIC, the better the estimated model [99].

To perform the multiple regression and subsequent AIC analysis, patient sex was assigned a value of 0 for females and 1 for males. Then, all possible combinations of the 4 explanatory variables of age, sex, height and weight and their cross terms were input into the regress function of version 9 of the data analysis and statistical software package STATA (Texas, USA). The AIC value for each of these regression combinations was also found. The combination of variables that were gave the lowest AIC value was selected as the model to be used in predicting how counts change in the whole-body bone scan image.

To determine the 'goodness of fit' of the best model derived from the multivariate regression, the residuals were calculated.

3.3 Results

3.3.1 Preliminary analysis

The results of the initial foray into the raw data (Appendix A) are displayed in Table 3. The amount of activity being administered to males is higher than those of females. Furthermore, the activity administered to females displays more variation (larger standard deviation). However, the mean injected activities for patients indicate that both sexes are being administered activities consistent with the current Christchurch Hospital clinical protocols (Chapter 2.6). The mean time between injection and scan time is higher than the 3 hour recommended by the guidelines but this could be due to constraints placed on the availability of equipment or patient not being ready for their scan at the allocated time. Focusing of patient anatomy, females appear to be both shorter and weigh less than males - not an unexpected result. Counts in each image appear to be similar for both sexes.

Table 3. Measured variables of the whole-body bone scan clinical study.

		Mean	Std Dev	Min	Max
Male	(N=28)				
Age	(years)	67.1	10.5	41	85
Height	(cm)	174.0	6.0	160	187
Weight	(kg)	82.6	11.2	57	108
Injected Act	(MBq)	706	29.3	635	758
Injection-Scan Time	(hrs)	3.3	0.3	2.8	3.9
Image counts					
- *Anterior*		2472424	587233	1531292	4075030
- *Posterior*		2361687	556681	1550684	4138477
Female	(N=37)				
Age	(years)	59.4	13.3	25	87
Height	(cm)	161.5	6.7	145	173
Weight	(kg)	68.6	15.8	41	104
Injected Act	(MBq)	685.0	56.9	590	940
Injection-Scan Time	(hrs)	3.2	0.3	2.5	3.7
Image counts					
- *Anterior*		2528004	528428	1676731	3914866
- *Posterior*		2376837	489338	1538347	3659672

3.3.2 Correlations between variables

Correlations provide information about the effect of one variable on another. The correlations between all the measured variables are displayed in Table 4. A correlation was said to be statistically significance if the p-value was below 0.01.

Table 4. Correlation matrices for the counts in the anterior projection images (Top) and posterior projection image (Bottom). Correlation coefficients are displayed on the top row with p values for each correlation listed beneath each coefficient. The 5 most significant correlations (defined as p value < 0.01) are highlighted in each matrix.

	Counts/MBq	Age	Sex	Height	Weight
Counts/MBq	1.0000	**0.5470**	-0.0765	-0.2283	**-0.4226**
	0.0000	**0.0000**	0.5449	0.0673	**0.0005**
Age		1.0000	0.3040	-0.0041	0.0933
		0.0000	0.0138	0.9743	0.4598
Sex			1.0000	**0.7135**	**0.4614**
			0.0000	**0.0000**	**0.0001**
Height				1.0000	**0.4623**
				0.0000	**0.0001**
Weight					1.0000
					0.0000

	Counts/MBq	Age	Sex	Height	Weight
Counts/MBq	1.0000	**0.5791**	-0.0473	-0.2224	**-0.4326**
	0.0000	**0.0000**	0.7084	0.0749	**0.0003**
Age		1.0000	0.3040	-0.0041	0.0933
		0.0000	0.0138	0.9743	0.4598
Sex			1.0000	**0.7135**	**0.4614**
			0.0000	**0.0000**	**0.0001**
Height				1.0000	**0.4623**
				0.0000	**0.0001**
Weight					1.0000
					0.0000

As the most significant correlations are between the same variables for both the anterior and posterior counts per MBq, we will only plot the 5 most significant correlations for the anterior projection data counts to visualise the relationships between these variables.

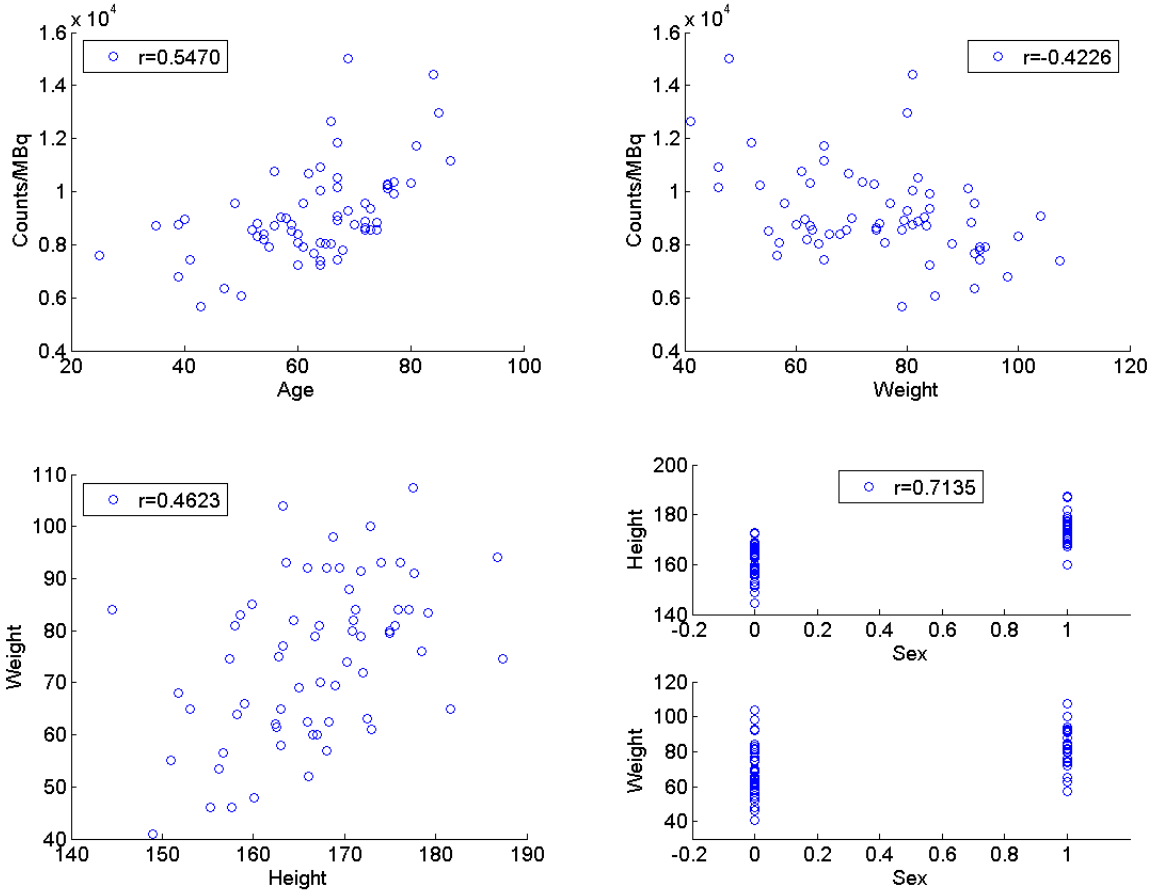

Figure 10. The 5 most significant correlations between variables measured in the clinical study. The correlation coefficients are taken from the anterior correlation matrix of Table **4** and are displayed on each graph as r values.

The most obvious correlations displayed in Table 4 are that males are taller and also weigh more than females. Furthermore, there is a significant correlation between taller patients and weight. These are all relationships that could perhaps be expected to exist. The negative correlation between patient weight and detected counts is perhaps also expected since it is quite likely that the heavier a patient, the more soft tissue that the patient possesses. This extra soft tissue would have an attenuating effect on the radiation present within the patient thus explaining the lower counts per MBq detected by the gamma camera. The positive correlation between patient age and detected counts per MBq is interesting. It is possible that the older the patient is, the less they weight – although according to Table 4, the correlation between patient age and weight is not statistically significant.

3.3.3 Multivariate linear regression

The list of possible combinations of the 4 variables recorded in the clinical study and the corresponding AIC values are shown below in Table 5.

Table 5. AIC analysis to find the best model of the clinical study. The variables are defined as S = Sex, A = Age, H = Height, W = Weight. More than one letter corresponds to a mixed term, i.e. AH = Age x Height. Lower values of AIC indicate a better fit.

Regression Variables									AIC	
									Anterior	Posterior
S									1158.302	1148.685
A									1135.572	1122.28
H									1155.202	1145.532
W									1145.896	1135.361
H	W								1147.786	1137.31
BMI									1149.991	1139.268
H	W	HW							1149.387	1138.734
S	A								1131.253	1118.672
S	A	SA							1128.929	1116.626
S	H								1156.15	1145.779
S	H	SH							1158.12	1147.74
S	W								1146.468	1134.96
S	W	SW							1147.217	1135.509
A	H								1132.649	1119.363
A	H	AH							1116.453	1121.223
A	W								1112.226	1095.33
A	W	AW							1113.271	1095.942
S	A	H							1132.967	1120.194
S	A	H	SA	SH	AH				1133.122	1120.854
S	A	W							1113.981	1097.305
S	**A**	**W**	**SA**	**SW**	**AW**				**1110.618**	**1093.049**
S	H	W							1146.41	1134.391
S	H	W	SH	SW	HW				1150.662	1138.379
A	H	W							1114.222	1097.32
A	H	W	AH	AW	HW				1118.74	1101.071
S	A	H	W						1115.842	1099.226
S	A	H	W	SA	SH	SW	AH	AW	1113.472	1095.534

The AIC analysis reveals the most parsimonious fit arises from some linear combination of patient sex, age, weight, and various cross terms containing these 3 variables. Using the patient BMI only gives a poor AIC value when compared to other possible combinations. From the AIC analysis, the counts per MBq may be predicted using the coefficients displayed in Table 6.

Table 6. Coefficients of the model to predict the counts/MBq detected on the Millennium MG gamma camera for an individual patient.

	ANTERIOR	POSTERIOR
S	-8245.221	-7374.622
A	65.06357	56.31172
W	-65.81197	-72.02218
SA	63.54738	54.34536
SW	49.90918	47.96459
AW	.0083381	0.1294645
Constant	9866.491	9763.234

From Table 5 fits that use only terms directly related to the patient height and weight yields relatively high AIC values. This means that although it is possible to fit the data using patient height and weight, it is not the best fit. Therefore, for this collection of patients, our ability to predict the counts per MBq using only patient height and weight is not the best approach.

The absence of a height term indicates that height is much less significant than was originally anticipated. This may be explained by the fact that the gamma camera detector moves longitudinally along the patient while the greatest attenuating effect is expected to arise from the width of the patient.

3.3.4 Measure of regression fit: residuals and R^2

For a model to be an accurate descriptor of the measured data the residuals must be independent and normally distributed with mean 0 and standard deviation σ [97]. The mean and standard deviation of the residuals of the best fit based on the AIC analysis are displayed in Table 7 with the relative frequency of the residuals plotted in Figure 11. Overlapping the histograms are the normalised probability distribution functions (PDF) that have means and standard deviations equal to those in Table 7.

Table 7. The mean and standard deviation for the residuals for the anterior and posterior projection images - units are counts per MBq.

	Mean	Std Dev
Anterior	-0.00029421	1123.6
Posterior	0.00012176	981.6

The histogram appears to resemble the PDF match indicating that the residuals are in fact normally distributed with a mean of 0 and standard deviation σ. If we were able to increase the number of participants in this study, the shape of histogram would be expected to converge on the PDF.

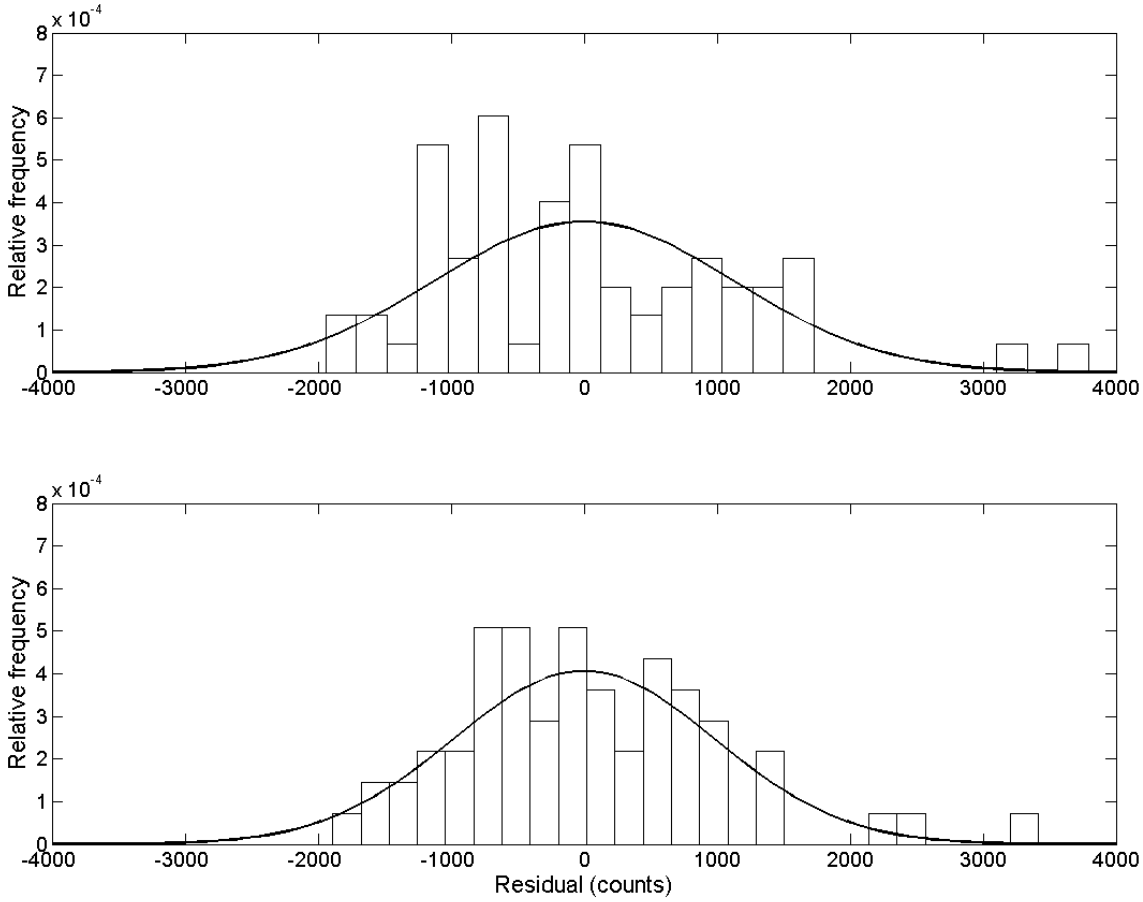

Figure 11. Residuals of the fit for the anterior projection images (Top) and posterior projection images (Bottom). The solid line represents the normalised probability distribution function described by the mean and standard deviation of the residuals of each projection.

Finally we calculate the measure of correlation, R^2, of each of the fits. The R^2 is the fraction of variation in the response variable that can be explained by the least squares regression of the response variable on the explanatory variables. In other words, an R^2 equal to 0 means that the fit explains none of the variation, while an R^2 of 1 explains all the variation. The R^2 value for the best fit as shown in Table 5 is 0.5907 for the counts per

MBq in the anterior projection images and 0.6365 for the counts per MBq in the posterior projection images.

In contrast, the R^2 values for the fit to the counts per MBq in the anterior projection image using only the height and weight terms is 0.1800 and 0.1878 for the posterior counts per MBq in the anterior projection image (Appendix B).

3.4 Discussion

The AIC analysis has revealed the 'best' fit to the clinical data based on our measured variables. Three important results can be drawn from this study.

First, the study has shown that the current clinical protocols are being adhered to with regard to administering activity. However, the mean time between injection and scan time for all patients is between 6.6-10% higher than the 3 hour time that is recommended by the hospital protocols.

Second, using the AIC analysis, the best predictor of the counts per MBq for each projection image is a linear combination of patient sex, age and weight. The use of AIC has revealed that the influence of height on detected counts per MBq is not as significant as was originally thought. Furthermore, this fit results in residuals that appear to be normally distributed with a mean very close to 0. This is evidence that the model found using the multivariate linear regression is an appropriate description of the data.

Finally, although the R^2 values for the best fit are significantly higher than for those using only a linear combination of patient height and weight, they are still much less than 1. This indicates a presence of a factor, or factors, that are causing a large amount of variation between the measured and predicted counts per MBq for the anterior and posterior projection images that this model can account for.

It is hypothesised that the factor responsible for reducing the 'goodness of fit' is the physiological differences between patients. Differences in patient physiology to that of the ICRP model will mean that the activity present within the patient at the time of their scan is

different to the activity used to normalise the counts in the image. In other words, if the true activities within the patients are different than those predicted by the ICRP kinetic data and used to normalise the counts in the image, then the fit found using the regression will not be accurate. The acquisition of these more accurate values of activity within each patient at the time of their scan would, at the very least require ethics committee approval for the collection of patient urine before their scan time. As patients are asked to empty their bladder right before their scan, this procedure would allow a more accurate determination of the actual amount of activity that remains within each patient's body at the scan time. However, clinical staff would need to allocate additional time to complete this task. This study already required an additional half an hour period to be added for each bone scan as it was required to obtain informed consent and record details from the participants. This meant the number of bone scans able to be performed in the nuclear medicine clinic on a daily basis was already reduced and in the interests of patient care and responsibility, performing this step could not be justified.

Also, the effect of age on patient physiology is also an important consideration. We observed a significant improvement in the AIC values when patient age is included in the multivariate regression. Age is known to influence patient physiology of pharmaceuticals [100, 101] and such influences could affect the uptake and clearance of the MDP or HDP radiopharmaceutical. Therefore, if we are interested in finding the optimum relationship between images counts and the activity administered, then the age of the patients should be incorporated into the model.

Finally, it was only possible to recruit a total of 65 participants for this study. It is possible that with increased participant numbers, a more obvious correlation between counts and a height and weight range may be observed. It is also possible that a more detailed statistical analysis may reveal underlying correlations that the AIC is not sensitive to.

3.5 Conclusion

The clinical study has revealed that the relationship between the detected counts per MBq in each projection image and the height and weight of a patient is affected to a degree by the sex and age of the patient. If we wish to quantify how the counts in the projection images are affected only by patient height and weight then we need to remove these additional influences through the use of a more controlled environment.

The use of the NCAT whole-body computational phantom in conjunction with the Monte Carlo method should provide such an environment. The phantom has the important advantage over a clinical study in that the factor that appear to have the greatest influence on the counts detected in the projection images such as the kinetics of the radiopharmaceutical can be controlled. Furthermore, the results are independent of patient age. Implementing a system that allows the simulation of the whole-body bone scan procedure is believed to give the best chance of determining the variation of detected counts based solely on the patient anatomy.

4. Development and validation of a Monte Carlo model of the GE Millennium MG gamma camera

4.1 Introduction

The aim of this study was to create and validate a model of the General Electric Millennium MG gamma camera within the Monte Carlo software, SIMIND. The dimensions of the detector, collimator and intrinsic characteristics of the gamma camera were defined using available documentation and measurement. Then, this model was tested in two series of experiments.

The first series of experiments was designed to calibrate the computational model. Calibration is a necessity because there are inherent limitations in the SIMIND which are expected to give differences between simulation and experiment. These differences may be accounted for by finding correction factors and applying them to the results from the simulations to allow a direct comparison between simulated and experimental data.

The second series of experiments was then performed to test the ability of the calibrated model to match standard performance measurements acquired from experiment. The model's ability was also tested in matching characteristics that are not carried out as part of usual quality assurance protocols but are still relevant to this study. Once fully validated, the model could then be used in a variety of clinical studies. More specifically, the model would be used in conjunction with the NCAT whole-body patient phantom to

determine the relationship between the counts in a whole-body bone scan image and patient height and weight.

4.2 Method

4.2.1 Computing resources used in this work

All SIMIND Monte Carlo simulations were executed on one of a collection of 6 Hewlett-Packard Desktop PCs. All 6 PCs had an Intel® Pentium 4 CPU running at 2.80 GHz and 496 MB RAM. All PCs were running Windows XP Professional Version 2002 with the Service Pack 2 update. Version 4.5 of the SIMIND Monte Carlo program was installed on all 6 PCs using the self-installing script available from the SIMIND homepage, www.radfys.lu.se/simind.

4.2.2 Image analysis

ImageJ, used in the clinical study was again utilised to display and analyse the DICOM files taken from the gamma camera and to import and display the binary files produced by the SIMIND code. To view the simulated images in ImageJ, a 32-bit REAL image type was selected and the width and height of the image matrix were each set according to the experimental DICOM file. For the STATIC images, this was 256 x 256. For the whole-body images, the matrix size was 256 x 1024. An image offset of 0, with 1 image and gap of 0 bytes between images were set.

The integrated density is also able to be extracted from the simulated binary images using ImageJ. However, instead of being the mean grey value multiplied by the area, the integrated density represents the total expected counts in one second, per unit of activity, where the value of activity is defined using the CHANGE program of SIMIND. Therefore,

to find the counts in a simulated image, the value of integrated density must be multiplied by the activity of the source and the length of time that the actual experiment was run for to calculate the number of counts in a ROI.

The second image analysis software used in this study was AMIDE (A Medical Imaging Data Examiner). This program was used in the spatial resolution validation experiment where the Full Width Half Maximum (FWHM) and Full Width Tenth Maximum (FWTM) of the line spread function from a line source were measured.

4.2.3 Physical phantoms

Line source phantom

The Nuclear Associates (New York, USA) line source phantom (Model 76-826) is shown in Figure 12 (Left). This phantom is used to determine the system spatial resolution in SPECT. The phantom consists of an acrylic cylindrical chamber filled with water. Within the water-filled chamber, there are 3 tubes no larger than 1 mm in diameter that are placed in the acrylic cylinder parallel to its axis and act as receptacles for the radioactive sources. Figure 12 (Left) states that Co-57 line sources are normally used. However, in reality, any appropriate radioactive source may be used. One tube is on the axis, the other two are 7.5 cm from the axis and 90 degrees apart with respect to the central tube [36].

IEC count rate performance in scatter phantom

Figure 12 (Right) shows the National Electrical Manufacturers Association [36] [36] "Count rate performance in scatter" phantom (New York, USA) used in the majority of calibration and validation experiments. The phantom contains an inner disk filled with water. This inner disk is designed to be filled with a radioactive source to be imaged alone, or placed inside a larger Perspex phantom. The insert alone provides little scattering material while the outer Perspex phantom is designed to approximate the high level of scatter expected from a patient's torso. Therefore, this phantom can approximate low and high scatter conditions, respectively.

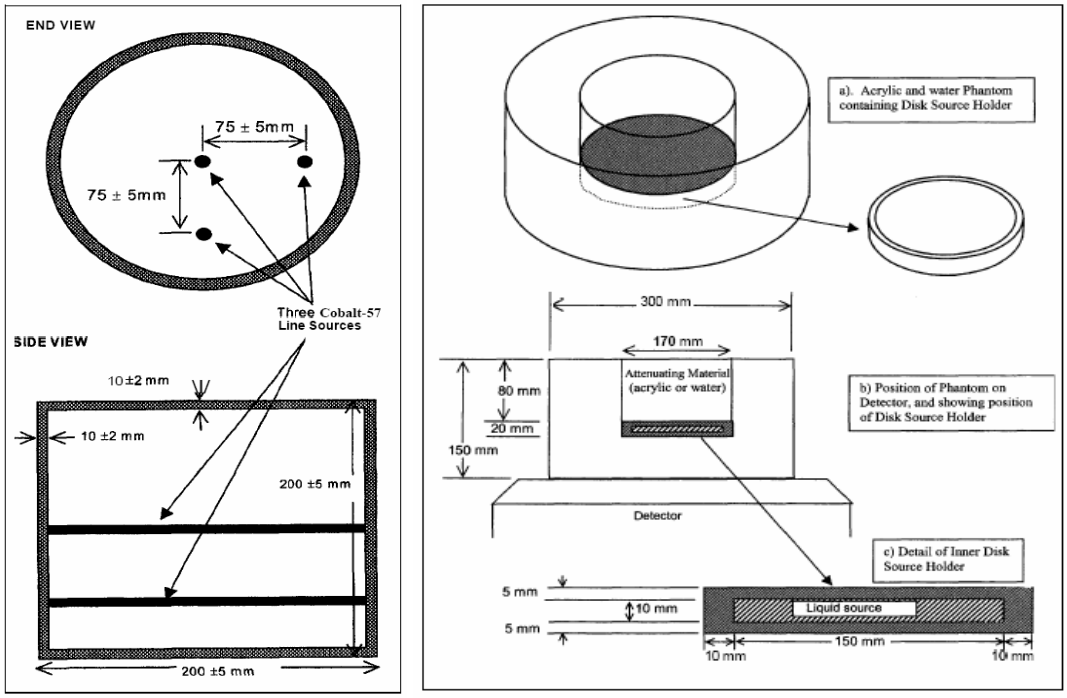

Figure 12. Quality assurance and validation phantoms used in this study. (Left) The NEMA line source phantom as used for the spatial resolution experiment. (Right) The IEC count rate performance in scatter phantom used in both the correction factors and validation experiments.

4.2.4 Technetium sources and dose calibrator

Technetium 99m sources were the main radioactive source used in this study. They were dispensed from the Mo-99/Tc-99m generator present in the Nuclear Medicine department at Christchurch Hospital. All activities were measured using the AtomLab 200 #3 Dose Calibrator from Biodex Medical Systems (Shirley, New York), also located in the department. Tc-99m has a principal gamma ray emission of 140.5 keV with every one decay responsible for producing 0.885 of these photons [102]. This dose calibrator was also used in the clinical study to ensure consistency between the two studies.

4.2.5 SIMIND input

All SIMIND simulations are the result of the SIMIND executable reading an input file containing parameters that were specified in the CHANGE program. This section describes the settings that all simulations have in common and the specific settings for each of the detector of the gamma camera as only one camera head may be simulated at a time.

General parameters

The general parameters defined within SIMIND relate to saving files for the energy spectra, image files and random number seeding. The options are given a value of true or false and can be accessed and changed using the CHANGE program or by using the flag /tr:(index number) at the command line. The settings for all of the general parameters are summarised in Appendix C.

Camera settings

The detector head and crystal radius were determined using the data sheet describing the Millennium MG MPR collimator [103]. The field of view was set to dimensions of 536 x 380 mm. Thus, to model this geometry in SIMIND, the detector length (half-width) was set to 26.8 cm and the detector radius (half-length) was set to 19.0 cm. The crystal was modelled using the material cross-sections of NaI and was enclosed by a 0.1 cm thick aluminium cover. SIMIND does not model any photomultiplier tubes (PMT), light pipes or other components contained within the camera head. These parts may contribute to the backscatter of incident photons. To account for this, the backscattering

material was modelled as a 4 cm thick region of Lucite as is consistent with the literature [24, 68]. The pixel size for the output was set to 0.226 cm to match the pixel size in the recorded Digital Communication (DICOM) files from the camera.

Collimator settings

The LEHR MPR collimator present on the Millennium MG gamma camera was defined using dimensions taken from the collimator data sheet [103] and also from the collimator database included in the SIMIND distribution. It was found that the SIMIND collimator database did not have all the correct dimensions required to fully model the LEHR collimator. Where any discrepancies occurred, the dimensions from the data sheet were used preferentially. The full collimator settings are outlined in Appendix C.

Physics settings

All simulations were performed using the SCATTWINC routine. This routine is an alternative version of the SIMIND executable that allows the setting of multiple energy windows. These windows can be set to record information about scattering events in as many energy ranges as the user desires. Furthermore, it records images that can contain only un-attenuated or primary photons, and images that contain only the photons that have undergone scattering events. The energy windows are set using an ASCII text file. For our simulations, two energy windows were defined. The first was the 20% energy window centred at 140 keV (126-154 keV) that represented the photo-peak window as is set on the Millennium MG camera. The second energy window is the Compton scattering region of

92-125 keV [104]. The Compton window was recorded to be used in the scatter validation experiment. The routine also uses the "Delta Scattering Technique" to model photon interactions in the collimator [68]. This technique was developed mainly for modelling higher energy radionuclides such as I-123, I-131 and Ga-67 but the code records and tracks all lead x-rays that are generated in the collimator.

Other settings included tracking gamma ray photons from the radionuclide until they had undergone 10 scattering events. This was done using the switch '/sc:10' at the command line; it was designed to record the majority of lower energy photons present in the energy spectra and also to ensure that the variance reduction techniques utilised in SIMIND were used appropriately [105]. The solid angle for the photons was set to 1. This setting is another of SIMIND's variance reduction techniques called photon forcing. It improves the detection efficiency by only generating and tracking photons within the geometry that have a chance of interacting with the crystal [63]. Characteristic X-ray emission was included and interactions in the phantom, collimator and aluminium cover of the NaI crystal were modelled. This was done using setting this parameter to 'true' in the CHANGE program and by adding the '/xr:1' switch at the command line. The simulation of energy resolution in the crystal was turned on and forced interaction upon a photon entering the crystal was also included. Finally, the complete 512 energy channels available were used with each channel having an energy value of 0.352 keV. This was to provide the highest possible energy resolution over the 0 to 180 keV energy range in the simulated energy spectra. The full list of command line switches is outlined in Appendix E.

Spatial resolution

The SIMIND code requires values for the intrinsic spatial resolution of the NaI(Tl) crystal to be set in the input file created by the CHANGE program. These parameters were not known and furthermore, would not be expected to match exactly for both detectors. Therefore, before any simulations using SIMIND could be undertaken, these values must be determined through experiment.

A 414 MBq Tc-99m source was placed at a distance of 3 m from the gamma camera detector heads that were fitted with parallel bar lead masks as per the NEMA quality assurance (QA) tests of intrinsic spatial resolution [36]. The Tc-99m was contained in a standard 3 ml syringe and had a total volume of 0.5 ml. 5-minute acquisitions were taken individually for detectors 1 and 2. The spatial resolution values for the x and y uniform field of view (UFOV) were recorded by the GE analysis software and exported to a text file on the nuclear medicine server. The values recorded by these files gave a spatial resolution of 3.77 mm for detector 1 and 3.74 mm for detector 2.

Energy resolution

Like the spatial resolution aspect, the energy resolution of the two detectors was unknown. The following experiment was performed to determine the energy resolution values to be used as input to the model.

A 0.5 ml Tc-99m source contained in a 3 ml Perspex syringe had an activity of 6.35 MBq. The diameter of the cylindrical source was 8 mm and the height was 7 mm. The diameter of the cylindrical syringe was 10 mm and the height was 65 mm. A lead shield for radiation protection purposes was in place at a distance 1 m behind the source. Three different acquisitions of the energy resolution for detector 1 using this source were performed. First, the syringe was positioned at 1.8 m from the face of detector 1. Second, the source was moved to 3 m away from the detector. Thirdly, the source was left at 3 m but the lead shield was removed to provide an environment with little back scatter or characteristic lead x-rays. To measure the energy resolution for detector 2, two acquisitions were done. First, the source was placed at 1.8 m away from the face of detector 2 with the lead shield in place. Second, the source was moved to a distance of 3 m and lead shield was removed.

Table 8. Energy resolution values expressed as % FWHM of the photopeak window.

Experiment	Detector	
	1	2
Run 1 (1.8m Pb shield)	9.01	8.54
Run 2 (3m Pb shield)	9.03	N/A
Run 3 (3m no shield)	8.93	8.68
Average	8.99	8.61

To calculate the energy resolution input for SIMIND, the average of the energy resolution value were found for each detector. A value of 8.99% for detector 1 and 8.61% for detector 2 was set using the CHANGE program.

4.3 Calibration and correction factors

4.3.1 KeV per energy channel correction factor

The aim of this experiment was to find the keV per energy channel calibration factor [36] for the detector heads of the Millennium MG gamma camera. The need for this experiment arises due to the file format output by the Millennium MG software. This output is a binary file, which only contains a binning number and number of counts in that bin. There is no indication of the physical energy each bin represents. To determine a function that allows a conversion from bin number in the binary file to a physical energy, the following experiment was designed and carried out.

Experimental

The LEHR collimators were removed from the camera detectors. A 0.5 ml Tc-99m source with an activity of 6.35 MBq was placed 1.8 m away from each detector head. The source was contained in a standard 3 ml Perspex syringe of diameter 10 mm and 65 mm. The 'spectra' scan mode was initialised to simultaneously record and save the energy spectra from the Tc-99m syringe source once 10,000 counts had been recorded in the photo-peak window. To provide a second point on the energy scale, the experiment was repeated using a Co-57 reference source from RadQual, LLC (Ohio, USA). Co-57 has principal gamma ray emission energy of 122.06 keV [102]. The activity was measured to be 3.52 MBq by RadQual on the 14th February 2005. This activity was corrected to a present day activity of 0.54 MBq using a value for the half-life of Co-57 of equal to 271.80

days [102]. A second spectra scan was performed simultaneously on both detectors until 10,000 counts had been recorded in the photo-peak. The energy spectra files were stored in an unsigned 16-bit integer binary format with 4096 energy bins.

Simulation

Each experiment was repeated in SIMIND with input files specific to each detector and the source being simulated (Appendix D). The Tc-99m source and syringe housing were defined as horizontal cylinders. The source was specified as being shifted +2.5 cm in the +x direction relative to the origin of the SIMIND coordinate system. This was to model the source as being present at the end of the syringe. The Co-57 source and source housing was described as a horizontal cylinder constructed from aluminium. However, this was an approximation as the actual construction material was unknown. The ISOTOPE sub-routine was invoked to model the two significant gamma ray emissions from the Co-57 source of 122 and 136 keV Co-57. This sub-routine is initialised by setting the photon energy (index 1 in the CHANGE program) to a negative number. This forces the code to look for an isotope file, which is a two columned ASCII file located in the smc_dir folder of the directory the SIMIND program has been installed. The first column of this ASCII file contains the photon energy and the second column is the proportion of the decay of the radionuclide that produces this photon energy. The emission energy and proportion of each were defined according to published International Atomic Energy Association [102] data [102]. To tell the executable what file to use, the switch '/fi:co57' was added to the

command line (Appendix E). Both sources were set at a distance of 1.8 m from the face of detector 1 and 2. Finally, the option to include the collimator in the simulation was switched off to match the experimental conditions.

Data analysis

The experimental energy spectra of the Co-57 and Tc-99m sources were converted from their original binary format into the ASCII format using the ReadSpectrum.m MATLAB script [106] (Appendix F). The spectra were then plotted using the MATLAB (Massachusetts, USA) curve-fitting toolbox. A first order Gaussian fit of each photo-peak region was performed using 400 channels in the range of the peak (Figure 13). The form of the first-order Gaussian equation meant the midpoint of the fit corresponds to the channel number matching the physical energy of the primary gamma ray emission of each respective radionuclide. A linear fit to the channel number and physical energy was matched to the data points. This fit is the keV per channel calibration factor of each detector. As a measure of the agreement between the calibrated experimental and simulated energy spectra, each energy spectrum was normalised to the maximum value and plotted for a visual comparison.

Results

Figure 13 shows the first order Gaussians fitted to the channel numbers corresponding to the photo-peaks of the Tc-99 m and Co-57 sources. The channel numbers corresponding to the mid point of each Gaussian fit are displayed in Table 9. The channel numbers for the photo-peak were matched with the known photon energy from each radionuclide. For Co-57 the photon energy is 122.06 keV and for Tc-99m the photon energy is equal to 140.51 keV.

Table 9. Channel numbers for the Gaussian fit of each photo peak.

	Channel number	
	Co-57 (122.06 keV)	Tc-99m (140.51 keV)
Detector 1	987.6	1134
Detector 2	979.2	1121

A linear fit was then performed to find an energy calibration factor for each detector. This linear fit was done using the Microsoft Excel spreadsheet program (Redmond, USA) and the results are displayed in Figure 14 and Equations 1 and 2.

$$E = 0.1256 \cdot C - 2.071 \text{ (Detector 1)} \quad (1)$$

$$E = 0.1310 \cdot C - 6.444 \text{ (Detector2)} \quad (2)$$

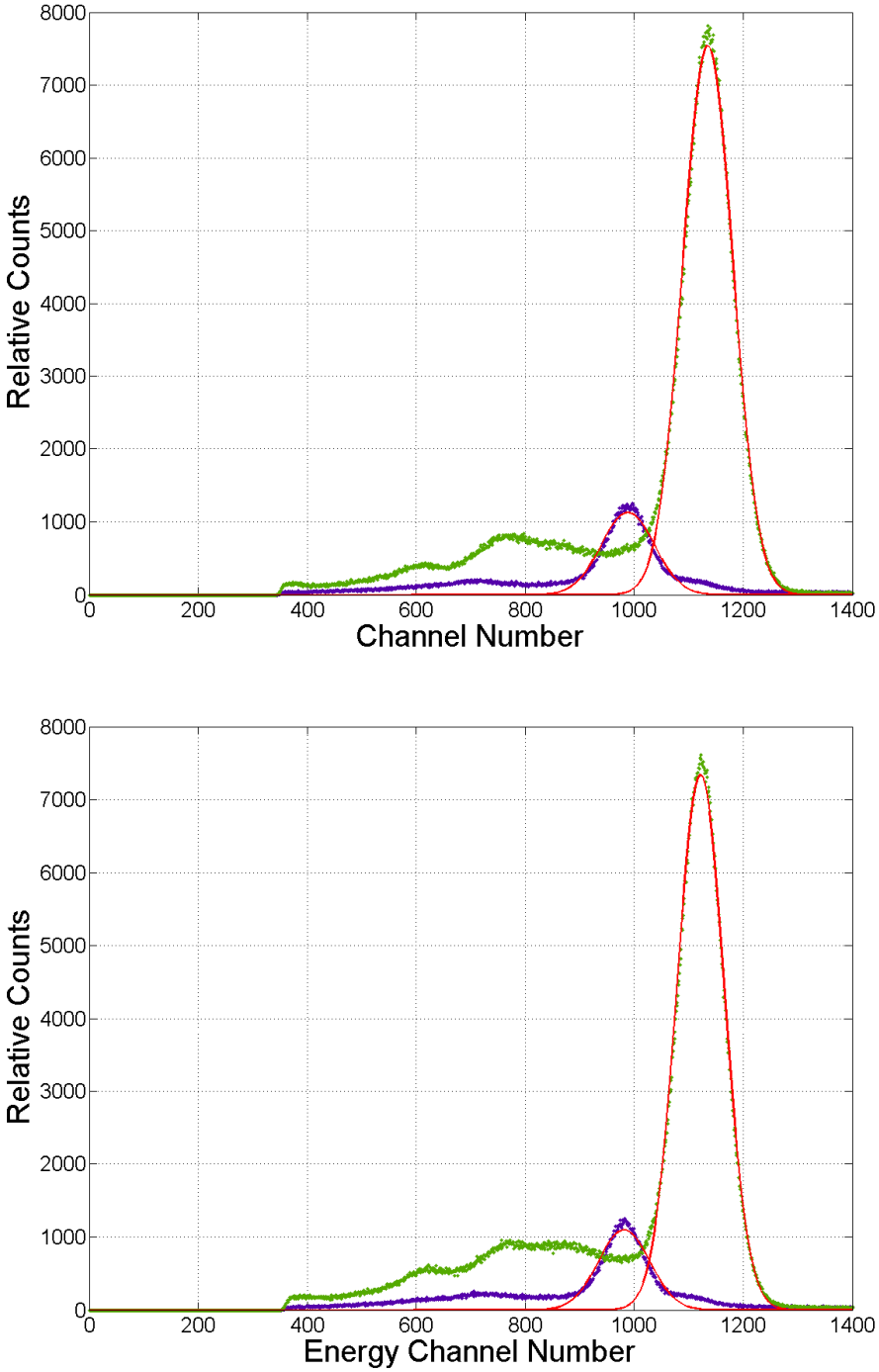

Figure 13. (Top) Gaussian fits for the Co-57 and Tc-99m photo peak as measured by detector 1. (Bottom) Detector 2.

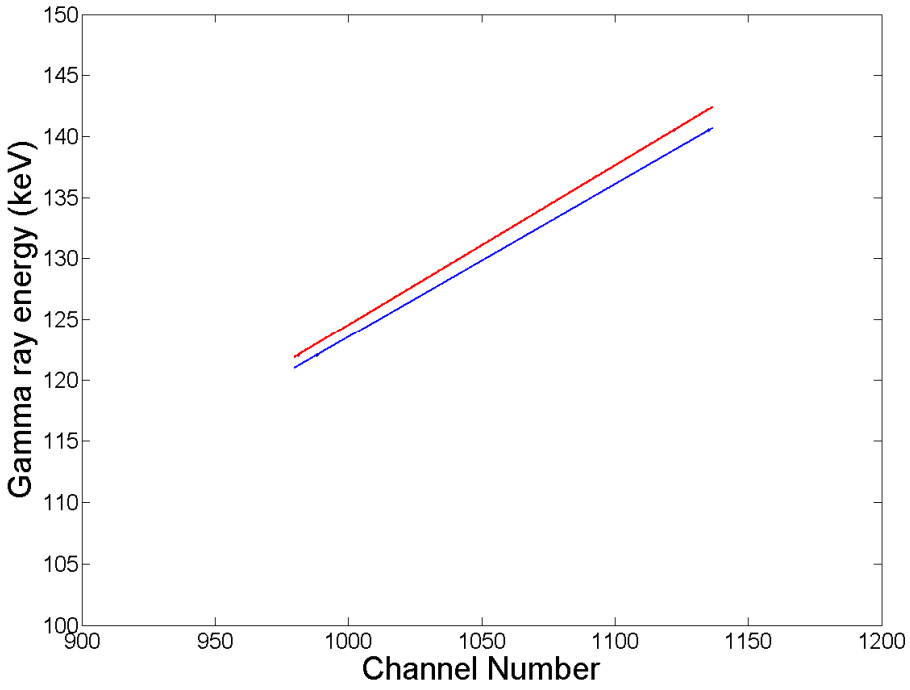

Figure 14. Energy calibration factors for the Millennium MG. Detector 1 (red line); Detector 2 (blue line).

Thus, equation 1 and 2 above are the keV per energy-channel calibration factors that must be applied to the spectrum files taken from the Millennium MG in order to convert the binning numbers into a physical energy.

Comparison of measurements with calibrated Monte Carlo simulation

The result of applying (1) and (2) to the binary files is displayed in Figure 15. Here each spectrum was normalised to the maximum value in the file and overlaid with the corresponding simulated energy spectra.

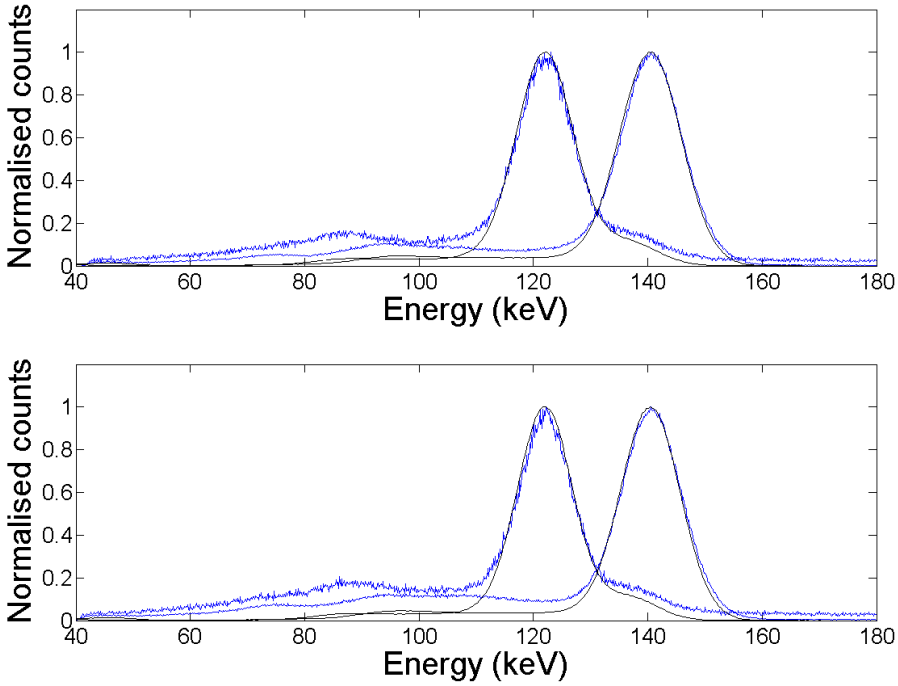

Figure 15. Corrected energy spectra using the energy calibration factors determined from channel number and physical energy of emitted gamma rays. (Top) Detector 1; (Bottom) Detector 2. Black lines are the simulated spectra, while blue represent the measured spectra.

There is close agreement between the simulated and experimental energy spectra after the application of the correction factor. This gives us confidence in converting the binning numbers from the Millennium MG into a scale of energy. Figure 15 also shows that the simulated data underestimates the number of counts for energies below the lower value for each of the photo peaks. This could be indicative of the model not accounting for higher orders of scatter. It may also be a contribution from the opposing detector head, since this detector surface cannot be specified in the simulation.

4.3.2 Sensitivity correction factor

The aim of this experiment was to find a factor that would correct for the differences in the sensitivities of the experiment and simulation. This difference might be due to the model not accounting for the scattered photons that are accepted by the camera. Since the sensitivity is a measure of the counts per second per unit activity (CPS/MBq), this correction factor would in effect, provide a method to scale the number of counts in a simulated image to the 'true' counts in the same experimental static image taken from the gamma camera. This experiment was also performed as part of a quality assurance measurement of the Millennium MG, to confirm that the sensitivity of the gamma camera did not varying significantly over the duration of this study. A consistent value of sensitivity for a given source and phantom configuration meant that images acquired at the start of the study can be confidently compared with those acquired later.

Experiment

To find the sensitivity correction factor, the insert of the IEC count rate performance phantom was filled with amounts of activity varying from 37.6 MBq to 622 MBq and static scans of the insert alone, or insert and phantom configuration acquired on both detector 1 and 2 for a 5-minute period. Ten scans were performed; four on detector 1 and six on detector 2. Where the insert was imaged alone, it was placed on polystyrene blocks so that it was positioned at a distance of 11 cm from the face of both detectors. For

experiments where the insert and phantom were imaged together, the phantom was placed directly on the face of the detector.

Simulation

The series of experiments described above were repeated in SIMIND using settings for the specific detectors and the dimensions of either the IEC insert of IEC insert or phantom depending on what configuration was used in the experiment (Appendix C & D). A total of 10 million photon histories were run for each simulation with the activity of the defined source set to equal that of its corresponding experiment.

Data analysis

A circular ROI corresponding to the boundary of the insert was defined on the experimental image as shown in Figure 16. The integrated density of this ROI was found and converted to total counts via the area correction factor of $(2.26)^{-2}$. Using the number of counts, the sensitivity was found based on the decay corrected activity and the 5-minute time of the static scans. For the simulations, the sensitivity was read directly from the output file of the simulation.

The experimental sensitivity was plotted against the simulated sensitivity and a linear fit of the points was performed with the fit passing through the origin. The gradient of the fit then corresponds to the calibration factor that must be applied to the counts within a ROI of a simulated image.

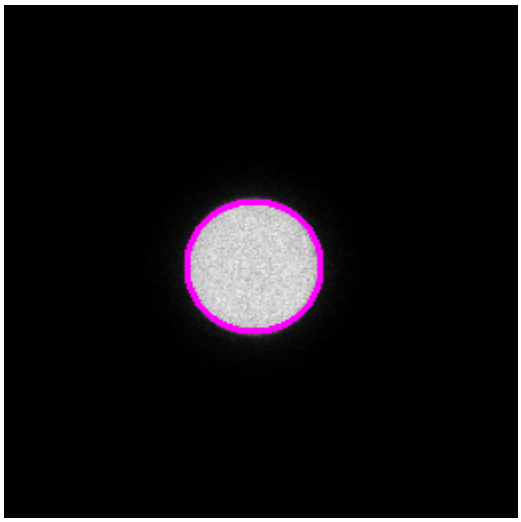

Figure 16. The ROI defined around the source contained within the IEC insert for an experimentally acquired static image. The thickness of the boundary has been exaggerated for clarity.

Results

The results of the ROI analysis of the experimental images and the corresponding simulated results are shown in Table 10. The last two columns are then displayed in Figure 17.

Table 10. Sensitivity correction factor to calibrate the simulated model of the Millennium MG gamma camera.

Detector	Activity (MBq)	Insert	Phantom	Counts in ROI (5 mins)	Sensitivity (CPS/MBq)	
					EXP	MC
1	40	X		5086357	82.99	73.17
1	67.6	X		8799251	84.95	73.23
1	72.2		X	4959551	44.83	38.24
1	622.1	X		72747584	76.32	72.85
2	37.4		X	2722622	47.51	38.14
2	40	X		5093912	83.11	73.61
2	67.6	X		8857523	85.51	73.40
2	69.5		X	4877227	45.80	38.31
2	613.8		X	39247800	41.73	38.14
2	622.1	X		73275704	76.87	73.26

Table 10 shows that the experimental sensitivities are consistently higher. This is perhaps due to differences in the activities of our experimental sources as measured by the AtomLab dose calibrator. If the activities measured using this dose calibrator are down by 15% then that would explain the variation in our experimental sensitivities. The same dose calibrator as used in the clinical study to ensure consistency, but is we wish to ensure that the activities used in the experiment are the same as those set for the simulations we require some figure that provides a calibration of the dose factor back to a primary standard. Unfortunately, this figure was unavailable.

The variation may also be due to the additional sources of scatter contributing to the counts in the experiment. Such sources may include the opposing camera head, and walls and floors surrounding the detector which the simulation cannot account for. Figure 17 shows the relationship between simulated and experimental sensitivity for the insert and phantom configurations found using the least squares linear regression feature of the MATLAB curve-fitting toolbox. The relationship appears linear with activity as expected from the definition of sensitivity. The sensitivity is lower for when the outer phantom is present, as the phantom provides a larger region where photons emitted form the source can be scattered. These scattered photons are not likely to be recorded by the detector, and hence account for the lower sensitivity.

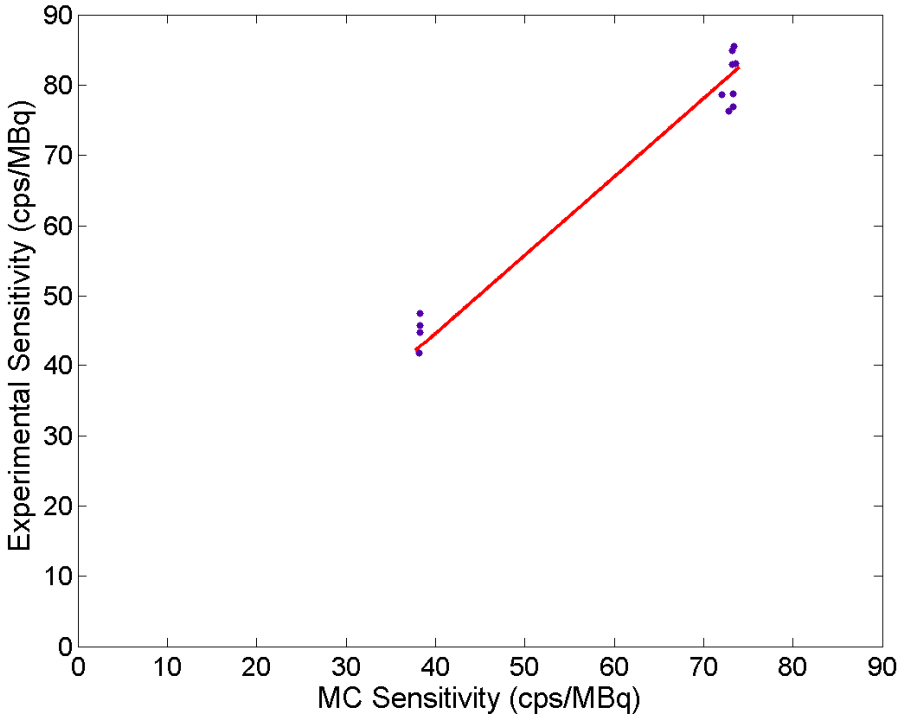

Figure 17. Sensitivity correction factor to account for differences in gamma camera performance and simulated model.

The gradient of the fit as measured from the MATLAB curve-fitting toolbox is 1.119 ± 0.036. Therefore, the linear relationship between simulated and experimental sensitivity is:

$$Sensitivity(Exp) = 1.119 \cdot Sensitivy(MC) \quad (3)$$

Conclusion

According to the linear relationship we have found, the counts in a simulated image must be increased by 1.119 in order to match the counts in a corresponding experimental

image taken from the Millennium MG gamma camera. Furthermore, the magnitude of the gradient approximates the amount of scatter that the simulated model is not accounting for, at least in the photo-peak energy window where the images were acquired.

Finally, there is little variation in the sensitivity over the duration of the study. Therefore, images acquired at different times may be analysed without correcting for a varying sensitivity over time.

4.3.3 Bed attenuation correction factor

The Millennium MG has a bed that patients lie on for the duration of their whole-body bone scan. This configuration means that the bed is between the patient and surface of detector 2 and so has an attenuating effect on the gamma radiation that originates from the patient and is incident on the detector. The bed has a carbon fibre shell and contains low-density polyester foam. SIMIND is unable to model this and so the magnitude of this attenuation must be quantified so that we can apply a correction factor to the simulated images from detector 2.

Experimental

The IEC insert was filled with 264 MBq of a Tc-99m/saline solution and then placed on polystyrene blocks above the face of detector 2. This resulted in a source-detector distance of 10 cm. A 5-minute static acquisition was performed and the DICOM image saved. The insert was then placed on the bed with a source-detector distance of 14.5 cm and another 5-minute static image was acquired. Next, the insert was placed inside the outer IEC phantom and the phantom positioned on the bed. The source-detector distance was now 14 cm. A third 5-minute static image was acquired. Finally, the phantom was positioned its side resting on a table so that an ‘in-air’ measurement of the phantom at a distance of 14 cm could be acquired.

Data analysis

Circular ROIs were defined around the disk in the same manner as Figure 16. The total counts in each ROI were then calculated. These counts were normalised using the decay corrected activity present in the insert at the time of each static image acquisition. As a measure of the attenuating effect, the ratio of counts in the images where the bed was present, to the counts in the 'in-air' images for both insert only and insert plus phantom were found. The mean ratio was used as the factor to reduce the number of counts in the simulated images. The uncertainty is taken from the uncertainties in the number of detected counts in the ROIs and the uncertainty in the activity of the source.

Results

Table 11 shows the calculated ratios and thus the effect that the carbon fibre bed has on the number of counts in the images. The mean ratio must be applied to reduce the number of counts in simulated images of detector 2, when the patient bed is between the source and face of the detector. This situation arises most when we are simulating the posterior aspect of the NCAT whole-body bone scan.

Table 11. Corrected counts in the bed attenuation experiment. The magnitude of the ratios of counts is the attenuating effect of the bed.

SCAN	Corrected counts
Insert 'in-air'	23689
Insert 'with bed'	21879
Ratio	0.9236
Phantom 'in-air'	12325
Phantom 'with bed'	11754
Ratio	0.9536
Mean ratio	0.9386

Conclusion

There is a non-negligible attenuating effect of the patient bed of 6.1 ± 1.5%. Therefore, a correction factor of 0.9386 can be applied to any image simulated using detector 2. This will scale the number of counts in the simulated image to the expected experimental value.

4.3.4 Correcting for detector size

The whole-body bone scan is not a static procedure. The limited FOV of the detectors mean they are moved along the length of a patient from head to feet to acquire a whole-body image. The SIMIND code cannot account for any temporal motion of the detector heads and so the whole-body bone scan must be simulated in SIMIND by defining a detector with a length equal to that of the patient bed. This larger detector area means there is a much larger area for the gamma ray photons to be detected in any one second and so there is a corresponding increase in the simulated sensitivity. For example, if the simulated detector has a FOV with twice the area of the Millennium MG FOV, then it is expected that the simulation would detect twice as many counts per second per MBq of activity present. Therefore, to account for the difference in sensitivity in the whole-body bone scan simulation due to the larger area of the simulated gamma camera detector, the sensitivity must be reduced by the area of the FOV of the Millennium MG to the simulated FOV.

The width of the detector is the same for both the experimental and simulated model so the sensitivity was adjusted by taking the ratio of the length of the simulated and actual detector FOV. For the Millennium MG, the length of the simulated detector length of 194 cm compared to the actual detector length of 38 cm. Thus, the sensitivity that is output by the simulation is expected to be a factor of 5.10 higher than what is actually measured by the Millennium MG detectors.

4.4 Physics and image quality model validation

The calibration factors determined in the previous experiments are designed to account for the differences due to the inherent simplifications and differences between the model and experiment. However, once these have been accounted for, the model should be able to match the performance of the actual gamma camera. These following series of experiments are designed to investigate the spatial resolution and scattering physics and their effect on the image quality achievable using the simulated model of the Millennium MG gamma camera. More specifically, the spatial resolution, energy spectra, source-background intensity variation and scatter quantification are all investigated in detail.

4.4.1 Spatial resolution

The Full Width Half Maximum (FWHM) and Full Width Tenth Maximum (FWTM) of the Line Spread Function (LSF) are the main measures of the spatial resolution of a gamma camera system [36]. The aim of this experiment was to compare the experimental and simulated FWHM and FWTM of the LSFs to see how closely the model matches the values determined by experiment.

Experimental

The central chamber of the Nuclear Associates line source phantom (Figure 12) was filled with 192.1 MBq of Tc-99m corresponding to a total volume of 0.9 ml. The Tc-99m was injected at one end of the phantom and extracted at the opposite. This was an attempt to achieve a uniform activity along the length of the tube. The phantom was placed in contact with the collimator of detector 1 so that there was a distance of 10 cm between the central cylinder and the detector face. The radius of rotation of the 2 detectors was set to 187 mm meaning there was an 8 cm air gap between the exterior of the phantom and detector 2. A 5-minute static acquisition was performed on detector 1 and detector 2 simultaneously to acquire images of the line source. The Millennium MG camera detector heads were then rotated by 180º and the phantom was placed in contact with detector 2 with the same radius of rotation. A second 5-minute STATIC acquisition was performed.

Simulation

The experiment was repeated in SIMIND with the same geometry of the NEMA spatial resolution line source phantom with the simplification that only the central source tube was modelled (Appendix D). This simplification was believed to be valid as the phantom was positioned in such a way that two off-axis tubes were not between the source and face of the gamma camera detectors. The entire phantom was modelled as water since the SIMIND program cannot construct a phantom out of more than one material.

Four simulations were performed to match the permutations of the experiment configurations and to provide 4 simulated images that could be used to extract the simulated LSF.

Data analysis

ImageJ was used to define a rectangular ROI of width 578.82 mm and height 22.6 mm at the midpoint of each experimental and simulated line source image. This was where the activity of the experimental line source was most uniform. The dimensions of the ROI were set so that both the experimental and simulated line profiles span a width equal to the length of the camera FOV. This meant all the line profile vectors had the same length and number of data points accounting for any offsets in the midpoint caused by a mis-alignment of the source within the camera FOV. The line profiles from these ROIs were saved for display and comparison in MATLAB

To compare the experimental and simulated profiles, two steps were required. First, the experimental images did show evidence that the line source had not been aligned

parallel to the axis of rotation of the camera heads. This was corrected by shifting the midpoints of the experimental line sources to the centre of the camera FOV via a simple translation in a MATLAB script. Second, each line profile was normalised to the maximum value within the profile and scaled to give a maximum value of 1000, before each profile was displayed for comparison.

The FWHM and FWTM of the line source using the line profile tool of the AMIDE image processing software. Using AMIDE, the experimental DICOM image files were opened using the DICOM 3.0 import option. The simulated raw binary files were imported via the "Float, little Endian (32 bit)" option in the data format drop-down menu and selecting a 256 x 256 x 1 matrix size. To find the FWHM and FWTM, a line profile was generated through the midpoint of the image and the results read from the screen.

Results

An example of the acquired and simulated images of the line source is shown in Figure 18.

Figure 18. Images of the NEMA spatial resolution phantom with active line source. (Left) Experiment, (Right) Simulated. The window and level of each image has been altered to aide visualisation.

There is a build up of activity at the endpoints of the experimental image because the source is injected at one end of the phantom and then extracted from the opposing end. This procedure results in 'hot' points at the end of the tube where the Tc-99m accumulates. This is not an issue in the Monte Carlo technique and in contrast, the simulated image displays a uniform distribution along the length of the source. The peaks in the profiles measured by the detector furthest away from the source in Figure 19 show evidence of widening. This widening is due to the increased distance of the source to detector and is an expected geometric effect [34]. To quantify this widening, the FWHM

and FWTM of each line source were measured using a Gaussian approximation of the peak in the AMIDE image processing software. These are displayed in Table 12.

Table 12. FWHM and FWTM measurements in mm of a line source in the NEMA spatial resolution phantom. Percent differences between simulations and acquisitions (with respect to the acquisition value) are given in parentheses.

FWHM (mm)

	Phantom placed on Detector 1			Phantom placed on Detector 2		
	Detector 1	Detector 2	Ratio	Detector 1	Detector 2	Ratio
Measurement	9.40	12.95	0.726	12.66	8.73	0.690
Simulation	8.32	11.63	0.715	11.63	8.30	0.714
	(-11.5%)	(-6.4%)		(-8.1%)	(-4.9%)	

FWTM (mm)

	Phantom placed on Detector 1			Phantom placed on Detector 2		
	Detector 1	Detector 2	Ratio	Detector 1	Detector 2	Ratio
Measurement	16.28	24.19	0.673	23.78	16.53	0.695
Simulation	15.16	21.26	0.713	21.28	15.08	0.709
	(-6.9%)	(-12.1%)		(-10.5%)	(-8.8%)	

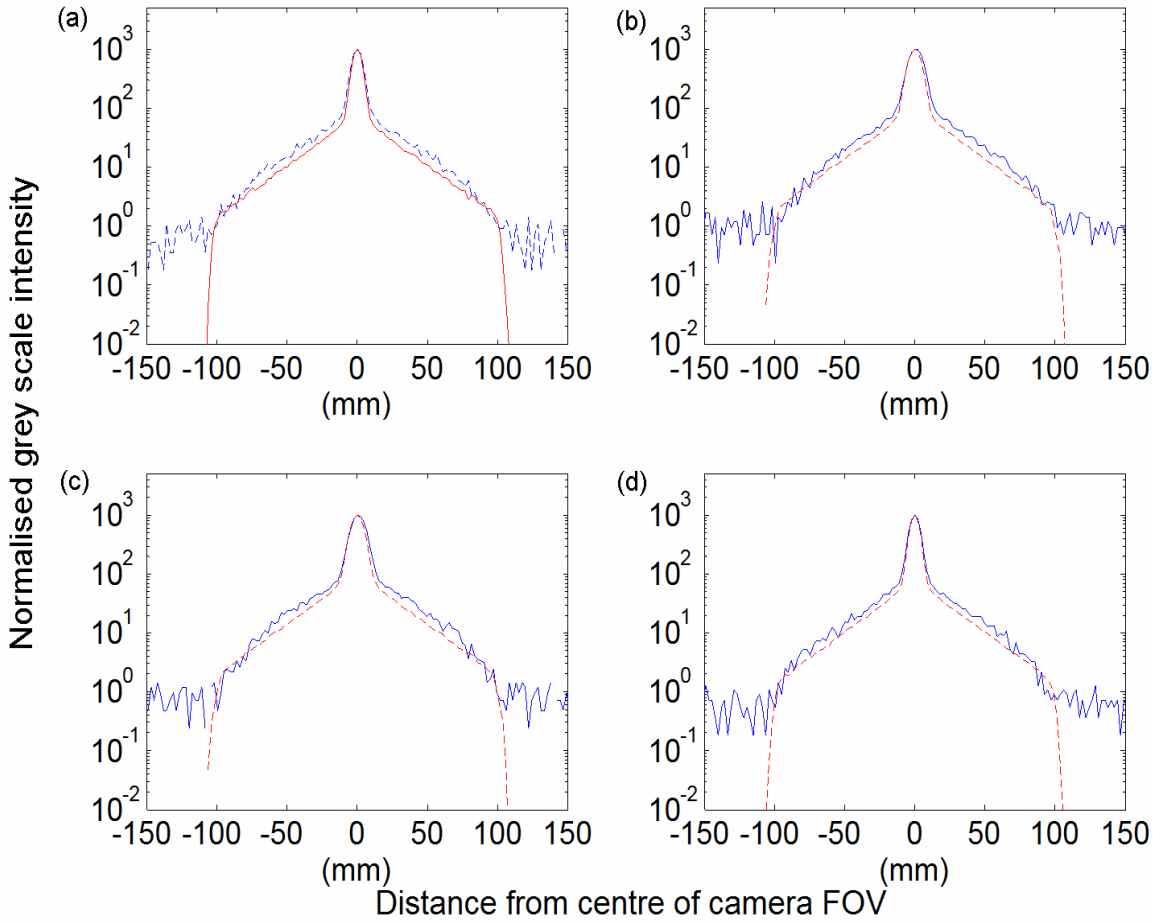

Figure 19. The LSFs for the NEMA line source phantom. (a) Phantom placed on surface of detector 1, profile measured on detector 1. (b) Phantom placed on detector 1, profile measured on detector 2. (c) Phantom placed on detector 2, profile measured on detector 1. (d) Phantom placed on detector 2, profile measured on detector 1.

4.4.1.1 Discussion and conclusion

From Table 12 we see that the Monte Carlo FWHM and FWTM are lower by 4.9-12.1% when compared with the measured results. From the raw values it appears that the simulated line source images have a higher spatial resolution than the experimental images. The ratios of FWHM and FWTM for the detector the phantom was resting on to the FWHM and FWTM of the opposing detector are also displayed in Table 12. The differences between measured and simulated ratios of the FWHM and FWTM have a maximum variation of 5.9%. This means the geometric effect on spatial resolution is well accounted for in the model. It also provides evidence that the difference is most likely due to the model collimator not having exactly the same dimensions as the real collimator installed on the Millennium MG. This is the case even though the manufacturer data sheet was used in conjunction with the collimator database within SIMIND. If a closer match was desired, the collimator would have to be removed from the camera and its dimensions measured directly. The only other approach to correct for the difference would be to incrementally increase the radius of the collimator holes and repeat the simulation until they matched. The magnitude of difference is not so large that it warrants the time required to undertake this.

Overall, the spatial resolution performance of the model shows an acceptable level of agreement with the measured values.

4.4.2 Energy spectra validation

The determination of the energy spectrum under different scattering conditions is an important performance measurement of the camera. It provides information about the scatter rejection capabilities of the camera through the use of the collimator and energy window setting. We wish to determine the agreement between the measured experimental and simulated energy spectra under two widely varying scatter environments. A good match would indicate that the physics algorithms implemented in SIMIND have the ability to treat scattering accurately thus providing another measure of validation.

Experimental

The insert of the NEMA IEC count rate performance in scatter phantom was filled with 83.9 MBq of Tc-99m saline solution and placed into the outer Perspex phantom to provide a high scatter environment. The phantom was then placed within the FOV on the surface of detector 1. The static acquisition mode of the Millennium MG Xeleris software was used to acquire an image of the phantom for 5 minutes. The energy spectrum was then recorded by using a spectra acquisition until 10,000 counts had been recorded in the photo peak energy window. Detector 2 was then rotated 180º and the insert and phantom configuration placed upon the detector face and the static and spectra scans repeated to acquire the DICOM image and energy spectra for detector 2.

To simulate a low scattering environment, the insert was removed from the acrylic phantom. The insert was placed on a two rectangular polystyrene blocks to raise the insert

off the detector heads. This configuration allowed both detector heads to be moved towards the centre of rotation of the camera. With a radius of rotation of 103 mm, the insert was at a distance of 10 cm from the face of detector 1 and 11 cm from the face of detector 2. Another 5-minute static acquisition of the insert alone was performed for detector 1 and 2 simultaneously followed by recording another spectra scan until 10,000 counts had been recorded in the photo peak window as was done for the insert and phantom configuration. The images from the static scans were exported from the camera in DICOM format while the spectra files were exported in a 16-bit unsigned binary format.

Simulation

The experiment was repeated using four input files containing the source and phantom dimensions of the IEC insert and phantom and the specific settings for each of the two detectors (Appendix C). The activity was set to equal the decay corrected activity at the time of the scans. 100 million photon histories were performed for each of the four simulations. The simulated energy spectra for each of the 10 scattering orders was extracted from its binary format using SIMIND's 'BIS' utility and saved into an ASCII format for plotting in MATLAB

Data analysis

The binary energy spectra files from the Millennium MG gamma camera were converted into an ASCII format using the MATLAB ReadSpectrum script [106]. The keV per channel calibration factor was applied to these files and the results were graphed. For

the simulated results, the 10 files containing the counts per energy bin for each of the 10 scattering orders were summed to find the total counts per energy bin and the total normalised to the maximum value in the spectra. These spectra were overlaid on the experimental results for comparison.

Results and discussion

Figure 20 shows the energy spectra recorded by the Millennium MG for both the insert and insert inside the phantom for the two detectors of the gamma camera. The spectra for the corresponding simulations are overlaid for comparison. All spectra have been normalised to unity using the maximum value of each spectra.

There are several things to note. First, the abrupt loss of signal in the experimental data below 40 keV is due to the internal threshold electronics of the Millennium MG. Second, the peak in the spectra from 72 to 75 keV is consistent with the characteristic x ray energy of lead [107]. These x rays have been generated in the LEHR collimator. More importantly, the presence of these x ray peaks indicates that SIMIND via the SCATTWINC routine is able to account for the generation and transport of these photons. However, the lead peak for the simulation of the insert alone is noted as being reduced in magnitude. The cause of this is unknown but it is possibly due to the approach taken in the normalisation of the spectra. Third, the close match between experimental and simulated data in the 92-125 keV energy range means the Compton region is being modelled accurately. This indicates that the physics model implemented in SIMIND is modelling scattering physics correctly.

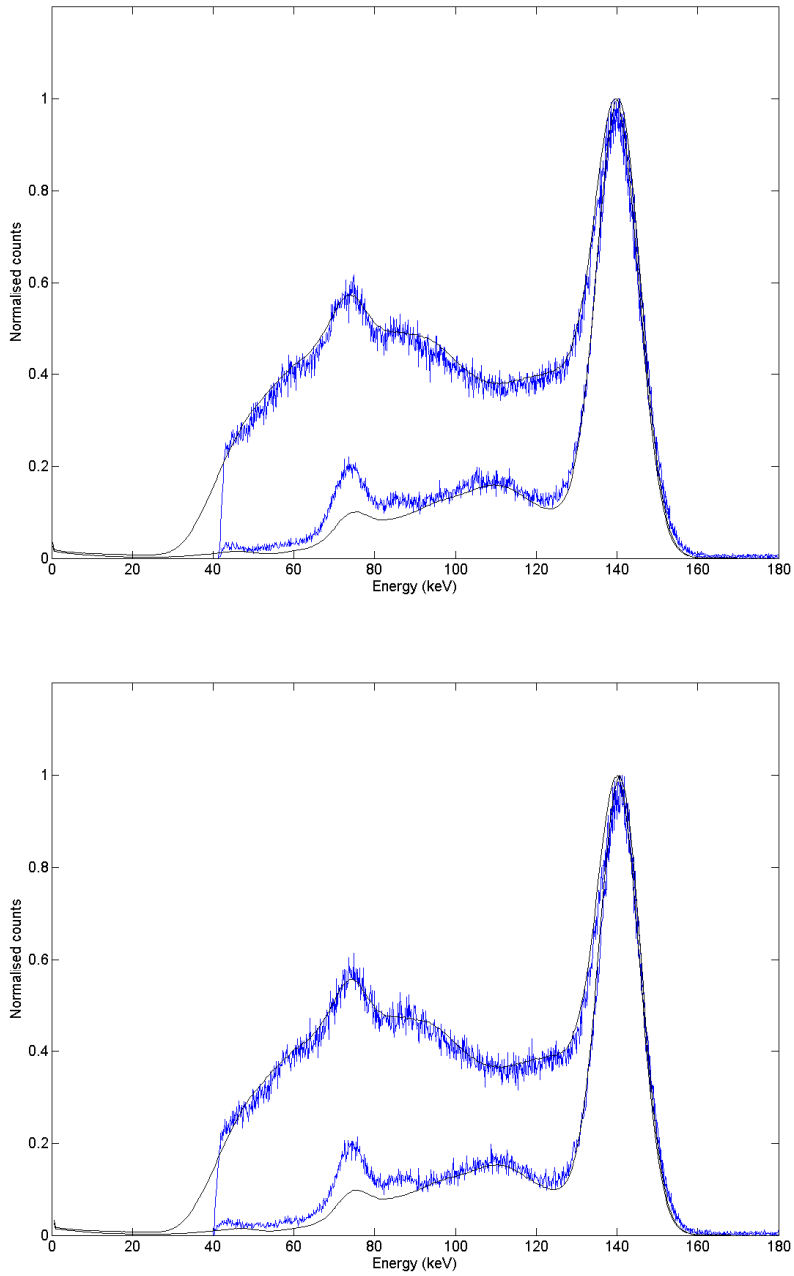

Figure 20. The IEC insert and phantom energy spectra for detector 1 (Top) and detector 2 (Bottom). The experimental energy spectra are shown in blue, with simulated results as solid black line.

Finally, the shape of the spectra in the photo-peak region of 126-154 keV shows very close agreement. The results of this validation mean SIMIND can accurately model the region where the counting statistics are recorded by the camera for analysis. Overall, the agreement between the experimental and simulated energy spectra for both low and high scattering conditions is excellent, especially in the region where clinical parameters are calculated.

4.4.3 Intensity variation at a source boundary

This analysis was performed to investigate how the code performs in regions where there is large variation in the radiation intensity. This is a common scenario found in nuclear medicine as radiopharmaceuticals are designed to display a high uptake in specific organs with very little in the surrounding tissue. For the proposed whole-body bone scan study, this situation would occur at skeleton-soft tissue boundaries.

Experimental

The same DICOM and binary images of the IEC phantom that were obtained in the energy spectra validation experiment were used for the analysis.

Data analysis

The radial plot profile plug-in for ImageJ [108] was used to extract the intensity of the experimental and simulated images from the centre of the phantom out to a radius of 45 cm. This ROI was use to visualise the change in intensity present at the edge of the insert and throughout the scattering material of the outer Perspex phantom. After the radial profiles were extracted using the radial profile plug-in, they were normalised to the maximum value in each profile. The experimental profiles were shifted to the origin to correct for the centre of the phantom not being positioned directly on the centre of the camera FOV. The profiles were then plotting using a MATLAB script for a visual comparison.

Results and discussion

Figure 21 shows the radial profiles for the experimental and simulated data.

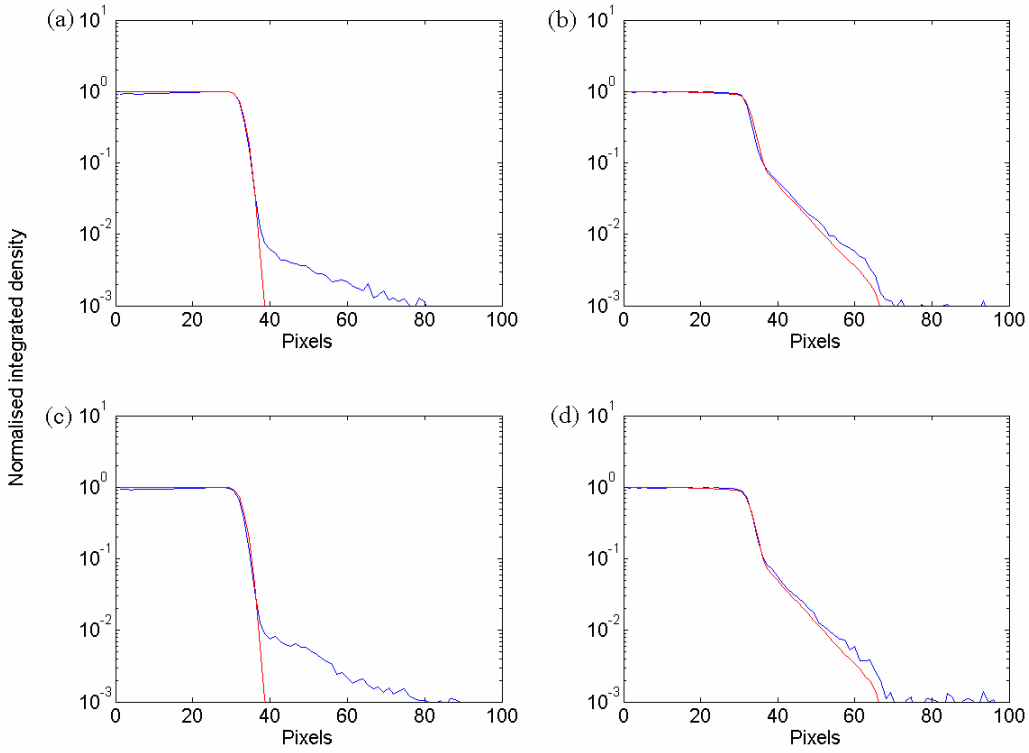

Figure 21. Radial profiles. (a) Insert only, detector 1. (b) Insert + phantom, detector 1. (c) Insert, detector 2. (d) Insert + phantom, detector 2. Experimental (blue), simulated (red).

The experimental and simulated radial profiles match well to the edge of the outer Perspex phantom. At the peak the normalised integrated density, of the profiles match within 1%. This indicates that the gamma camera possesses an excellent uniformity. At the boundary of the insert the two profiles diverge. Due to this region being outside of the insert, the higher number of counts is perhaps from photons that have back scattered from the opposing detector and/or from photons that have undergone more than 10 scattering

events. This is because the maximum number of scattering orders that photons are tracked through and recorded by the simulation is equal to 10. The low level of the signal may indicate that it is simply background noise.

Overall, the profiles show that SIMIND is modelling the source and rapid fall off in intensity within the dimensions of the phantom accurately.

4.4.4 Compton window scatter ratio validation

The Monte Carlo method provides detailed information about scattered radiation within the energy spectra that is difficult or impossible to quantify experimentally. One method that may be performed to quantify the level of scatter in an experiment is the calculation of the ratio of photons detected in the Compton region of the energy spectra to the number of events in the photo peak window. This experiment was performed as a final validation of the SIMIND program's ability to reproduce the scattering physics. It was also designed as a test of the sensitivity correction factor found earlier. Agreement between the ratios of scattering events in the Compton energy window to the counts in the photo-peak would provide confidence in using the code to set multiple energy windows and investigate the energies and orders of scatter in each. It would also confirm the sensitivity calibration factor is an accurate means of correcting the counts in a simulated image so that they may be compared with experimental images.

Experimental

To find this ratio, the IEC insert was filled with a total of 570 MBq of Tc-99m. This was inserted inside the phantom and the configuration was placed on the face of detector 2. Two energy windows were defined on the Millennium workstation. The first window was the standard 20% energy window centred at 140 keV. This records all gamma ray events within the energy range 126-154 keV. The second energy window was set to 92-125 keV to record scattering events in the Compton region of the energy spectra. A 5-minute STATIC

acquisition was performed and the image exported in the DICOM format for further analysis.

Simulation

The binary images of the IEC phantom produced in the energy spectra validation experiment were used again since this simulation was performed using the SCATTWINC routine which recorded the images in both the energy windows of 92-125 keV and the photo-peak energy window of 126-154 keV.

Data analysis

The DICOM files from the experiment and simulated binary images were analysed in ImageJ. For all the images, circular ROIs corresponding to the boundary of the disk were defined (see Figure 16). The same ROI was then used for the Compton energy window image to ensure consistency between all the images. The counts within the ROI were calculated using the value of integrated density. The sensitivity correction factor found earlier was applied to the simulated images. Furthermore, because this analysis used the simulated images of the IEC insert and phantom from the energy spectra and source-boundary validation experiments, a scaling factor was required to account for the different activities contained in the insert. Recall, the activity in the energy spectra experiment was 69.5 MBq. As the relationship between activity and count rate should be linear [63], a factor equal to (560.9/69.5) was used to scale the sensitivity corrected counts to the level of the dual energy window experiment.

After these two correction factors were applied to the simulated image, the ratio of the number of counts in the ROI of the Compton region energy window image to the number of counts in the photo peak energy window image was used as the parameter to determine the level of agreement between the experimental and the simulated images.

Results and discussion

Figure 22 shows the experimental and simulated images in the two energy windows. There is a noticeable haze or blurring of the insert boundary in the image where the energy window was set to 92-125 keV when compared with the photo-peak energy window. This is because *all* photons detected in the Compton energy window are ones that have undergone one or more scattering events and have not been rejected by the collimator. Such photons are detected as being in a position on the camera face that is different from their position of origin. This mis-positioning of events is the reason behind the blurring effect. In contrast, the images recorded in the photo-peak window display a sharp boundary since the image is made up mostly of primary photons (those which have not undergone any scattering events).

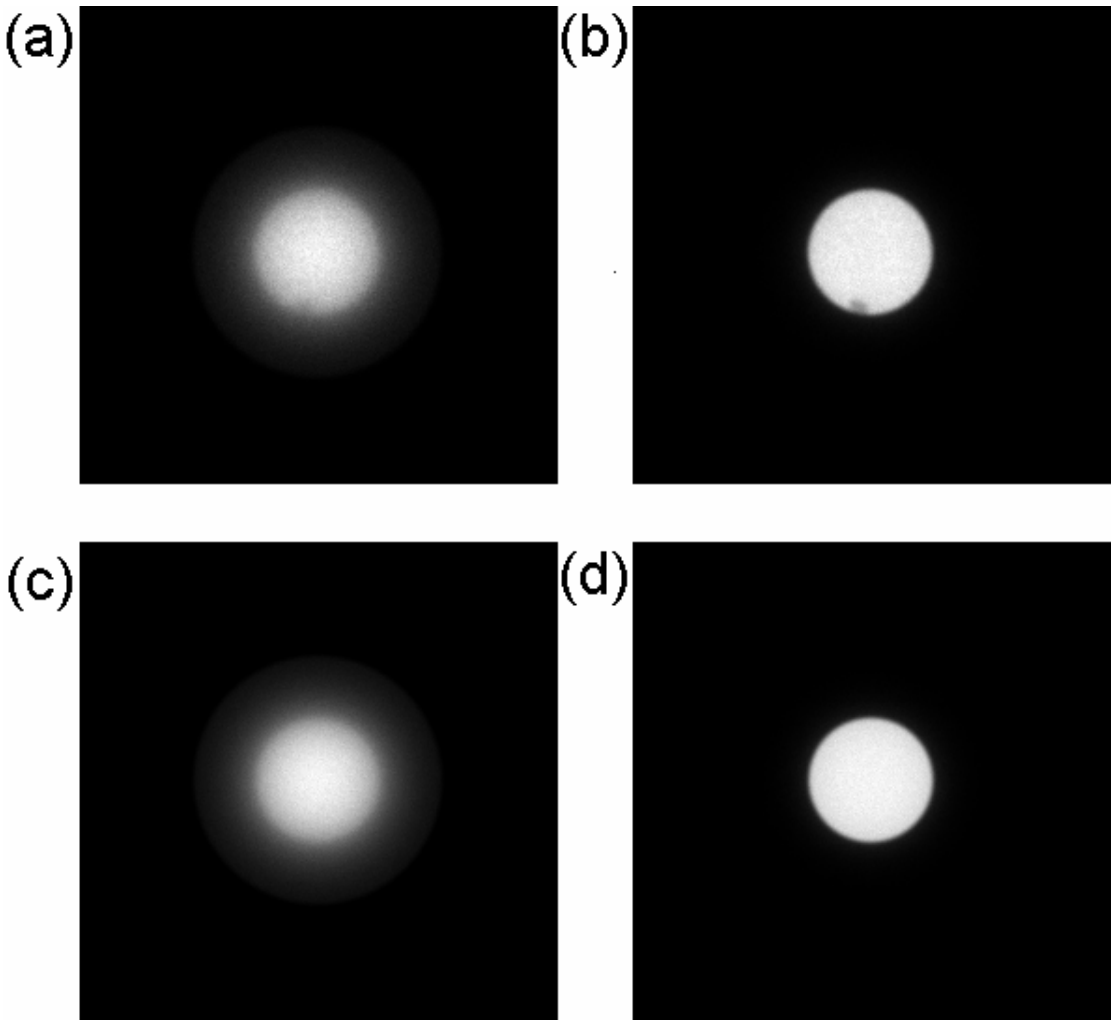

Figure 22. Dual energy window images. (a) Experimental image acquired in Compton region energy window. (b) Experimental image from photo peak energy window. (c) Simulated image from Compton region. (d) Simulated image of photo peak energy window. The slight non-uniformity in the experimental images is a region of reduced activity due to the presence of an air bubble within the phantom.

Table 13 shows the values for the number of counts in the image, normalised to the activity of the source. The corresponding uncertainties were calculated using the percent

uncertainty in the activity of the source and the sensitivity correction factor and also the statistical uncertainty associated with Poisson statistics of $\sqrt{N}$.

Table 13. Scatter quantification using the Compton and photo-peak energy window. (Values of counts are x 10^6)

	Compton	Photo-peak	Ratio
Measured	4.236 ± 0.042	7.026 ± 0.070	0.603±0.008
Simulated	3.866 ± 0.305	6.832 ± 0.540	0.566±0.063

Table 13 shows that the experimental values for the number of counts in both the photo peak and Compton energy windows are still higher than the simulation. In particular, the number of counts in the Compton window is higher than can be explained solely by experimental uncertainty. The simulation uncertainties are an order of magnitude larger than the measured due to the combined effect of the uncertainties in the correction factors, used to calculate the image counts.

The ratio of counts in the Compton window to the counts in the photo-peak window is also higher for the experiment. This is not surprising since all counts in the Compton window arise from scattering events. The difference may be partly due to the difference in activity measured by the AtomLab dose calibrator as was suspected in the sensitivity correction experiment. It may also be due to the model not possessing the opposing detector or walls and floors surrounding the camera, the model already suffers from a reduced number of possible origins of scatter. It is not surprising then, that the number of scattering events is significantly different.

Overall, this experiment has shown that the sensitivity correction factor is a valid method of scaling the counts in the simulated images acquired with the photo-peak energy window. Furthermore, within uncertainty, the ratio of counts in the Compton energy window to photo-peak window is the same. This is another validation that our model is a robust description of the Millennium MG gamma camera.

4.5 Study discussion: gamma camera development and validation

The goal of this study was to design, build and validate a model of the General Electric Millennium MG gamma camera within the SIMIND Monte Carlo simulation package. It was intended to use this model primarily to investigate the relationship between the variation of patient height and weight and accumulated counts detected by the gamma camera.

The validated model is also a tool to be utilised by researchers in future studies undertaken within the department. Much present day nuclear medicine research contains a significant Monte Carlo component and having a validated model provides incentive to use it for many reasons. First, it reduces the amount of time necessary to design and test such a model from scratch and as such, more time can be spent on the investigating real clinical issues - arguably a more interesting aspect of research. Second, it provides a measure of a 'gold standard' in which to compare clinical data by providing valuable information about the scattering events that are unable to be determined from experiment alone. Finally it reduces the amount of camera time needed for research. Performing a simulation may be time consuming but the wealth of information that can be gained from one may direct the focus of required experiments - perhaps uncovering an aspect of the geometry or unexpected variation that warrants further investigation. It may also lessen the need to repeat experiments, which means more time may be devoted to the camera's primary duty of providing patient care.

The results from all the calibration and validation experiments show that the model is very flexible and accurate in modelling a variety of simple phantom geometries typically used in nuclear medicine quality assurance protocols. This means that other simple geometries may be input by the user and the results obtained would be expected to be the same as if the experiment had been performed on the actual gamma camera.

It is believed that where differences between the simulation and experimental results do exist they can be explained by the inherent simplifications of the SIMIND model. These simplifications are in only being able to model a single detector and specifying the PMTs and electronics as a 4 cm thick, Lucite backing.

Overall, our model of the General Electric Millennium MG gamma camera has been validated for general use in nuclear medicine research studies that will use this camera. The results from all of the validation experiments undertaken in this study indicate that our model is a robust tool and one that is ready to be implemented in investigating the question originally posed by this study. That is, how do the counts in a whole-body bone scan image vary with patient height and weight?

5. Development and implementation of the NCAT phantom for use in whole-body bone scan simulations

5.1 Introduction

The 4D NURBS-based (Non-Uniform Rational B-Splines) Cardiac-and Torso (NCAT) phantom [79] has been developed to provide a realistic and flexible model of the human anatomy and physiology. It contains all the organs and the major bones of the human body, with simplifications for the skull, hands and feet. To date, the phantom has been used extensively in the areas of cardiac and respiratory gating, SPECT and PET imaging and radiology [82-86, 89, 109-111].

The major advantage in using computational phantoms such as the NCAT in simulation studies is that the exact anatomy and physiological functions of the phantom can be defined according to the requirements of the researcher. This provides a 'gold standard' that can be used to evaluate and improve medical imaging devices and image processing and reconstruction techniques. Furthermore, the NCAT phantom is able to be changed to model different anatomies and medical procedures. This provides the possibility of developing large populations of subjects from which to perform research, thus avoiding ethical and practical problems that can occur in clinical studies.

We wish to use the phantom in a study of whole-body bone scans. The motivation to use this phantom is that it allows both the organ shapes to be specified and the kinetics of the HDP radiopharmaceutical to be controlled. The control over the kinetics is an important

advantage since the variability of the kinetics between patients has been shown to have a significant influence on the amount of radioactivity present in individual patients at the time of their scan and hence, the number of counts detected in their whole-body bone scan image.

This study was undertaken primarily as a proof of concept. That is, we wished to see whether it was feasible to first, modify the NCAT whole-body phantom for use in investigating the whole-body bone scans, and second, to implement the modified phantom into the validated model of the Millennium MG gamma camera from the earlier study. If this proved to be possible then the simulation system could be used to answer the question pertinent to this study – that is, how the detected counts vary with patient height and weight.

Furthermore, because the NCAT phantom is a versatile research tool, experience with the phantom means it can be used in a wide variety of future theoretical and clinical studies.

5.2 Method

5.2.1 Changing the phantom anatomy

The male and female versions of the NCAT phantom were scaled from their default size using the mean height and weight of the male and female clinical study participants. The dimensions of the centroid male and female patient could have been used. However, the centroid male and/or female patient may have possessed unusual physiology which could have resulted in image counts that were significantly different compared to the mean. Using the mean value removes this possibility.

The mean height and weight for the clinical study participants was 174 cm and 82.5 kg for males and 161.5 cm and 68.5 kg for females. The change in anatomy was done using an updated version of the interactive GUI program developed by the NCAT author, William Paul Segars [81]. The GUI also has the ability to overlay real patient CT data to align the NURBS surfaces for patient specific simulations if desired (Figure 23). The height of the patients was scaled by selecting all structures in the phantom and using the "Scale in 3D" option in the GUI to reduce the male phantom from its default height of 189.0 cm to the required height of 174 cm using the ratio of 174/189. Similarly, the height of the female phantom was scaled down in 3D using the ratio of 161.5/189.

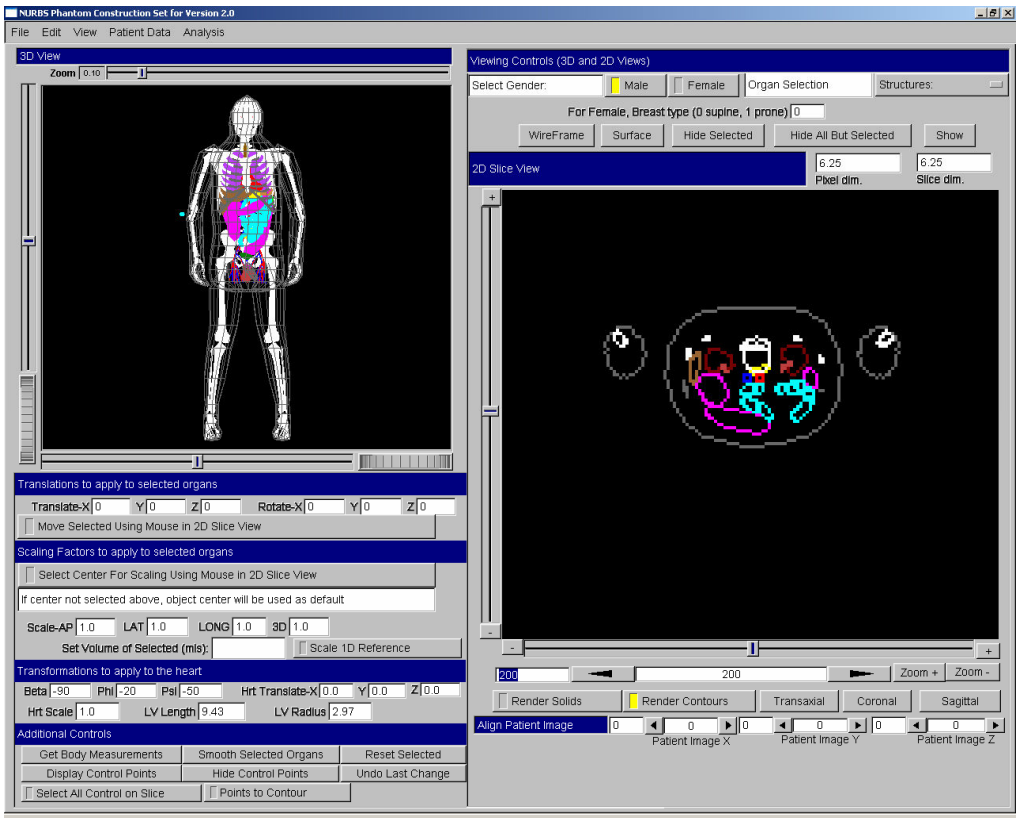

Figure 23. A screen capture of the GUI program used in the development of the average patient anatomy. Organs are changed using the organ selection tab (top right) and scaling factors (bottom left).

Defining the weight of the phantoms is more complicated since it must be found indirectly using the organ volumes that the GUI calculates. For the phantoms, the relationship between organ volumes and weight is

$$Weight = V_{skeleton} \cdot \rho_{bone} + (V_{body} - V_{skeleton}) \cdot \rho_{water} \ .$$

Using the calculated volumes for the skeleton and organs and a density of bone 1650 kg/m^3 and density of water equal to 1000 kg/m^3 [112], the weight of the phantoms

were found. The weights of the scaled male and female versions of the phantoms were lower than the average weights of the male and female patients in the clinical study. Therefore, it was necessary to use the GUI to alter the body outline of the phantom to increase the amount of soft tissue and therefore weight. This was done by selecting only the body outline, and scaling the anterior-posterior and lateral aspects of the phantom. Unfortunately, the required scaling factors are not obvious and must be found through trial and error, which is a time consuming process. For males, an Anterior-Posterior increase of 1.12 was used. For females, an Anterior-Posterior increase of 1.21 and Lateral increase of 1.01 was used to scale the body outline. These gave weights of 82.91 kg and 69.06 kg, compared with the actual average patient weights of 82.64 kg and 68.57 kg for males and females respectively.

5.2.2 Defining the phantom activity

The estimated average activity of the male and female patients at the time of their scan in the clinical study was used as the value for the total activity present in the phantom. This was 307 MBq for males and 305 MBq for females. For both male and female phantoms, the total activity was separated into two components. Based on the ICRP reference kinetic data of Table 2, the first component was distributed throughout the skeleton. The second was the remaining activity, which was distributed throughout the body soft tissue and specific organs.

It is possible to implement time-activity curves for all the organs and the bones that are defined in the parameter file. This is most useful in cardiac or pulmonary studies where the activity is rapidly varying with respect to time, or where the radionuclides used have short half-lives. However, in our study we used fixed values for the activity in each organ since, over the 20-minute duration of the procedure the total activity is only expected to reduce by 4%.

The activity in each of the bones that make up the skeleton of the phantom was assigned a fraction of the total skeleton activity based on its volume. For example, if the femur has a volume equal to 3% of the overall skeleton volume, it receives 3% of the total activity in the skeleton. This was designed to give a consistent activity per unit volume for the entire skeleton, representing a uniform uptake and retention of the radiopharmaceutical throughout every bone in the skeleton.

An important point to note is that while there are many bones defined in the phantom, only the activity of the spine head, spine process, pelvis and ribs may be set in the parameter file used to create the binary activity and attenuation files. This meant that the activity in the bones that make up these structures must be grouped together. For the spine head and spine process, the total activities in the cervical, thoracic and lumbar vertebra and the sacrum were divided equally between the spine head and spine process. The pelvis activity was used without modification. Finally, since the rib activity defines the activity of the remainder of the skeleton, the rib activity was set to equal the sum of the activity in the remaining bones, i.e. the bones of the arms, legs and skull.

To define the activity for the organs, the second component of the activity was distributed according to each organ's volume. However, the sum of the activity in the organs was not equal to the second activity component. This meant there was some leftover activity. This leftover activity was assigned as the body activity to approximate the soft tissue retention of the radiopharmaceutical. Finally, the bladder activity was set to 0 since the counts in the bladder were removed using a ROI in the clinical study.

Table 14. Distribution of activity within the NCAT phantom. The activities represent the proportion of activity present in the average male and female patient at the time of their scan**.**

	Male (MBq)	Female (MBq)
Skeleton		
- Spine	47.73	48.76
- Pelvis	45.59	45.69
- Ribs	210.68	208.54
Organs	0.20	0.20
Body	2.65	1.80
Total	307	305

5.2.3 Phantom parameter file

The NURBS surfaces defining the organ and body surfaces of the NCAT phantom must be transformed into voxels in order for photon transport to be able occur in a Monte Carlo simulation. To achieve this, the NCAT phantom program contains a utility that reads a parameter file as input and outputs two binary files that represent the activity and attenuation maps for input into any Monte Carlo software. The parameter file contains all of the anatomy settings and allows the activity of the organs to be set. To produce a voxelised phantom representing the average male and female patient, the parameter file was

set to use the ‘average_clinical_male.nrb’ and ‘average_clinical_female.nrb’ anatomy files that were created using the GUI. The activities of the organs were set in the parameter file according to their volumes as described previously (Appendix G). The utility was then executed and the activity and attenuation maps for the average male and female patient in the clinical study were used to define the source and phantom in SIMIND.

5.2.4 Simulation

The activity and attenuation binary files must have the same base file name as the input file for the simulation to work [113]. They were renamed to ncat_act_av.bin and ncat_atn_av.bin and placed in an appropriate directory that contained the SIMIND input file ncat.smc. Within the SIMIND input file, both the source and phantom type were set to ‘-7’ as is required to implement the NCAT phantom in SIMIND. The activity of the source was set to 1 MBq so that the counts in the images would have units of counts per second per MBq. The simulation was then performed from the command line using the SCATTWINC routine. The number of histories for each simulation is determined by the relative activity concentration in the binary activity file. Based on the information contained in this file, the code calculates the number of decays for each organ and normalises this to the total number of photon histories intended to be simulated [113]. For the male phantom, this resulted in 114 million histories and 105 million for the female phantom.

From the simulated images, we find the integrated density of the entire image in units of CPS/MBq. To compare with the average counts extracted from all the images in the clinical study, the following must be done. First, the CPS/MBq value is reduced by the detector size correction factor of 5.10 to represent the expected reduction in sensitivity due to the smaller detector size used in the clinic. Then, the adjusted value for the CPS/MBq was multiplied by 1164 seconds (the duration of a typical whole-body bone scan is 19.4 minutes) to find a value of counts per MBq. Next, the sensitivity calibration factor of 1.119 was applied to account for the lower magnitude of scatter in the simulation. The bed-attenuation correction factor was applied to the posterior projection images. Finally, the counts per MBq for each phantom was multiplied by the activity contained within the phantom. This then gives a value for total expected counts in the simulated whole-body images. We can now compare the simulated value of total counts in an average patient, to the average clinical values for the male and female patients.

5.3 Results

Figure 24 displays the result of the SIMIND simulation using the average female NCAT phantom with activity defined using Table 14. In particular, the skull, along with the lower half of the arms and legs are much brighter than the rest of the skeleton, which is indicative of an increased uptake in these bones.

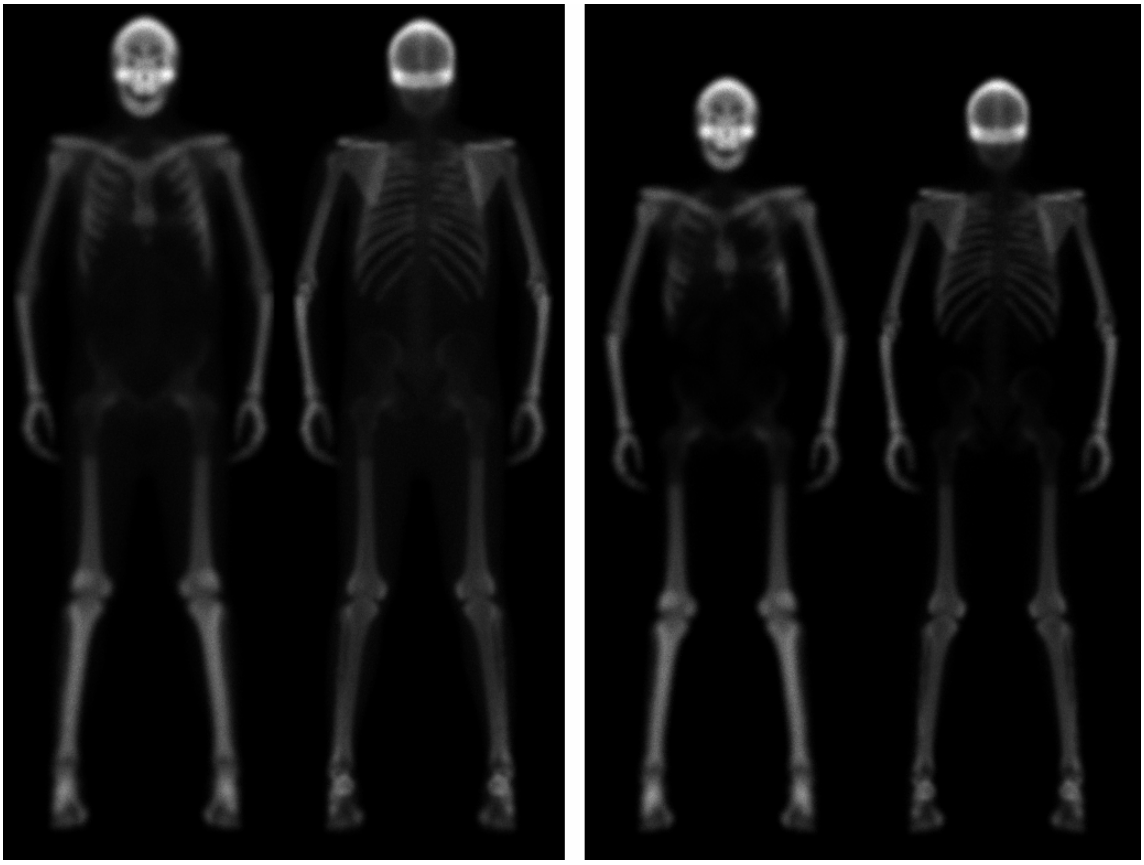

Figure 24. The male (left) and female (right) NCAT phantom anterior and posterior projections produced by the SIMIND simulation using the Millennium MG model, the average patient anatomy from the clinical study and the ICRP reference kinetics (without body activity).

Table 15 shows the calculated counts for the average male and female phantoms of Figure 24. The measured values are the averaged image counts for all the male and female patients in the clinical study.

Table 15. Counts for the NCAT phantom simulation and the average counts for male and female patients in the clinical study. Uncertainity in measured values σ in detected counts for study participants. Uncertainty for simulated is combined uncertainty in sensitivyt correction factor and bed attenuation correction factor. The percent difference is relative to the measured counts and is shown in parentheses.

	Male		Female	
	Anterior	Posterior	Anterior	Posterior
Measured	2472424	2361687	2528004	2376837
	± 587233	± 556681	± 28428	± 489338
Simulated	2845197	2170481	2887754	2148098
	±85356	±97672	±86633	±96664
	(15.08%)	(-8.10%)	(14.23%)	(-9.62%)

The anterior counts of the phantoms are approximately 15% higher than the measured values with the posterior projection images close to 10% lower. The increased anterior counts may be due to the increased activity in the skull, and lower arms and legs of the phantom where there is little attenuating tissue. The lower counts for the simulated posterior projection images may be due to the reduced amount of activity in the spine and pelvis of the NCAT phantom relative to the other bones in the body as can be seen in Figure 24. As these bones are closest to the posterior detector, it explains the reduction of detected events.

5.4 Discussion

While the NCAT phantom has been used in many areas where the bone *shape and density* has been important, as in radiology studies [82, 84], this study is believed to be the first time the phantom's skeleton has been implemented in a *functional* study of nuclear medicine. The results of using the phantom are extremely encouraging as they show that they predict values for counts in a whole-body bone scan within the range of those found clinically. This means that is it likely that the phantom could be used to investigate the variation in expected counts with patient height and weight. However, some problems were encountered.

First, while the phantom provides the most detailed representation of the true structure of internal organs and bones, the distribution of activity throughout the phantom is difficult to model accurately as evidenced by the lack of activity in the pelvis and spine of Figure 24. With the skeleton, there is an inherent restriction as the activity of all the bones in the skeleton is set by defining quantities in only four regions - the pelvis, spine head, spine process and ribs. This situation probably arises from the fact that these were the only bones originally contained in the original 3D NCAT phantom. Furthermore, there has not been any demand to use the phantom for functional imaging of the skeleton to date and so the status quo remains. Therefore, the activity in the additional bones of the skull, cervical vertebrae, and bones are still based on the activity given to the ribs. One important

improvement that could be implemented in future versions of this phantom is the ability to define the activity of a greater number of individual bones.

Second, it may be desirable if the phantom had the provision to distribute the activity throughout the skeleton based on the surface area of each bone rather than its volume. The reason that this may lead to improvements in accuracy in simulating bone scans is that the phosphate-based radiopharmaceuticals are not distributed evenly throughout the bone volume. Instead, they only bind to the surface of the bone [27]. It is hypothesised that this would lead to more accurate distributions of activity throughout the skeleton, especially in bones that display large surface areas such as the spine and pelvis. Since the phantom is based on the NURBS surfaces, it should not be difficult to implement a method in the GUI to output the surface area of the organs as an alternative to organ volume.

The second major problem encountered in this study is the time consuming nature of the approach adopted in this study. The length of time required to change the anatomy of and define the activity distribution within the default phantom was typically one days work. Compounding this is the lengthy nature of the Monte Carlo simulations. For acceptable statistics and image quality, a typical duration of a single projection simulation using the NCAT phantom on a single CPU was approximately 8 hours. Therefore, for an anterior and posterior projection, completely simulating one phantom takes the better part of a day. As this study would require the creation of multiple patient sizes, and their subsequent

simulations, without increasing the amount of computing power, the feasibility of this study decreases.

The GUI is an excellent tool for visualising and altering the anatomy of the NURBS surfaces describing the patient anatomy. However, it would be desirable if a more precise method of defining the weight of the patient *within* the GUI was available. This could be a scaling factor as is done with the organ sizes. This addition would make studies such as ours, which utilise the entire phantom much easier to undertake.

As it stands, this study has used the most advanced model of human anatomy to describe the dimensions of the average male and average female patient observed in the clinical study. We have also implemented the ICRP reference kinetic data to model the distribution of activity in the skeleton and organs of the NCAT phantom specific to those found in a whole-body bone scan. Furthermore, the study has confirmed that it is possible to implement the entire phantom in the SIMIND Monte Carlo simulation software to represent the average patient in the earlier clinical study. The counts that are produced are similar in magnitude to those expected in a real clinical case. Thus, the original proof of concept that this thesis was based on has been confirmed. That is, the study has shown it is feasible to apply Monte Carlo techniques in conjunction with the NCAT phantom to investigate a clinical study, specifically a whole-body bone scan.

Finally, it is recommended that this study be continued if two conditions are satisfied. One, should a later version of the NCAT phantom be released with the improvements believed to be necessary for an accurate description of the activity

distribution of the HDP/HMDP based radiopharmaceutical, and two, the provision of more computing resources in conjunction with a more efficient methods of defining a variety of patient sizes.

6. Conclusions

The overall aim of this thesis was to investigate how the counts in whole-body bone scan projection images vary with patient height and weight. To investigate this issue, this study was divided into three parts. First, a clinical study was undertaken in an attempt to determine the relationship between the variables. The analysis revealed that the weight is the more important aspect of patient anatomy. However, the anticipated influence on the counts in the images due to the sex and age of the study participants was proven to be correct. Because of these influences, it was decided to pursue a proof of concept study as to whether it was feasible to utilise modern simulation techniques to isolate the effect of patient anatomy on image counts.

The second part of the thesis involved designing and validating a Monte Carlo based model of the planar gamma camera imaging system present in the nuclear medicine department at Christchurch Hospital. To accomplish this aim, a series of standard performance measurements and performance measurements specific to this study were undertaken to ensure the model was a robust representation of the imaging system. It also means that our model will be able to be applied to a variety of clinical problems in the future.

Then, to develop a simulation system for whole-body bone scans, the NCAT whole-body computational phantom was modified to represent a typical whole-body bone scan patient and implemented into model. The results of the implementation are

encouraging and we believe that if minor improvements are made to the phantom, the continuation of the study will provide valuable and clinical relevant information.

References

1. Gordon M, Rishpon S, Gorski M: **Delayed diagnosis of carcinoma of the oral cavity**. *Harefuah: Journal of the Israel Medical Association* 2005, **144**(4):243-245.

2. Halpern AC, Lieb JA: **Early melanoma diagnosis: A success story that leaves room for improvement**. *Current opinion in oncology* 2007, **19**(2):109-115.

3. Chan KK, Selman TJ: **Testing for ovarian cancer**. *Best practice & research Clinical obstetrics & gynaecology* 2006, **20**(6):977-983.

4. Tanyi M, Fülöp B, Garami Z, Garai I, Tanyi J, Lukács G: **The role of MIBI scintigraphy in the early detection of breast cancer**. *Journal of the Hungarian Surgical Society* 2001, **54**(2):118-122.

5. Blomfield P: **Management of cervical cancer**. *Australian family physician* 2007, **36**(3):122-125.

6. Collins LG, Haines C, Perkel R, Enck RE: **Lung cancer: diagnosis and management**. *American family physician* 2007, **75**(1):56-63.

7. Young G, Toretsky JA, Campbell AB, Eskenazi AE: **Recognition of common childhood malignancies**. *American Family Physician* 2000, **61**(7):2144-2154.

8. Badawi RD: **Nuclear medicine**. *Physics Education* 2001, **36**(6):452-459.

9. Bushberg JT, Seibert JA, Leidholdt Jr EM, Boone JM: **Nuclear Medicine**. In: *The Essential Physics of Medical Imaging.* Edited by John J-R, 2 edn. Philadelphia: Lippencott Williams & Wilkins; 2002: 587-719.

10. Webb A: **Introduction to Biomedical Imaging**. Hoboken, New Jersey: John Wiley & Sons Inc.; 2003.

11. Siantar CH: **Fast Monte Carlo for radiotherapy - the PEREGRINE code**. *Radiation Physics and Chemistry* 1998, **53**(3):346.

12. Weaver K, Siantar CH, Chandler W, White RM: **A source model for efficient brachytherapy computations with Monte Carlo**. *Medical Physics* 1996, **23**(12):2079-2084.

13. Donohoe KJ, Henkin RE, Royal HD, Brown ML, Collier BD, O'Mara RE, Carretta RF: **Procedure guideline for bone scintigraphy: 1.0**. *The Journal of Nuclear Medicine* 1996, **37**(11):1903.

14. PTGEANMM: **A radiopharmaceuticals schedule for imaging in paediatrics**. *European Journal of Nuclear Medicine and Molecular Imaging* 1990, **17**:127-129.

15. Stabin M, Brill A, Segars W, Emmons M, Gesner J, Milam R: **Realistic phantom series for OLINDA/EXM 2.0**. *The Journal of Nuclear Medicine* 2006, **47**(Supplement 1):156P.

16. Stubbs JB, Evans JF, Stabin MG: **Radiation absorbed doses to the walls of hollow organs**. *The Journal of Nuclear Medicine* 1998, **39**(11):1989-1995.

17. Abel-Dayem HM, Amaral H, Bahk YW, Britton K, Collins L, Divgi C, Fernández O, Gopinathan Nair PG, Hutton B, Jia HT *et al*: **Guidelines for General Imaging: Muscoskeletal system**. In: *Nuclear Medicine Resources Manual.* Edited by IAEA; 2006.

18. Ott RJ, Flower MA, Babich JW, Marsden PK: **The physics of radioisotope imaging**. In: *The Physics of Medical Imaging.* Edited by Webb S. Bristol and Philadelphia: Institute of Physics; 1988: 142-318.

19. Blomquist RN, Gelbard EM: **ASSESSMENT OF EXISTING KLEIN-NISHINA MONTE CARLO SAMPLING METHODS**. *Nuclear Science and Engineering* 1983, **83**(3):380-384.

20. Horowitz YS, Dubi A, Mordechai S: **MONTE CARLO NONUNIFORM SAMPLING TECHNIQUE APPLIED TO THE KLEIN-NISHINA PROBABILITY DENSITY FUNCTION**. *Nuclear Science and Engineering* 1976, **60**(4):461-482.

21. Li D, Shaohui C, Zhengfeng H, Jie H: **A Monte Carlo model for gamma-ray Klein-Nishina scattering probabilities to finite detectors**. *Journal of Nuclear Science and Technology* 1996, **33**(9):736-740.

22. Nowotny R: **XMuDat: Photon attenuation data on PC**. IAEA; 1998.

23. RSC: **Radioisotopes in medicine: A history of nuclear medicine. No. 5 in a series of essays on Radioactivity produced by the Royal Society of Chemistry, Radiochemical Methods Group** London: Royal Society of Chemistry; 2005.

24. Larsson A: **Corrections for improved quantitative accuracy in SPECT and planar scintigraphic imaging**. *PhD Dissertation* 2005.

25. Tsui BMW: **Collimator Design, Properties and Characteristics**. In: *The Scintillation Camera.* Edited by Simmons GH: The Society of Nuclear Medicine; 1988.

26. Wieczorek H, Goedicke A, Edström F, Degenhardt C, Botterweck H, Bippus R: **Collimator Spatial Resolution**. *IEEE Nuclear Science Symposium Conference Record* 2005, **3**:1717-1721.

27. Francis MD, Fogelman I: **Tc-99m diphosphonate uptake mechanism on bone**. In: *Bone scanning in clinical practice.* Edited by Fogelman I, vol. 1. Berlin: Springer-Verlag; 1987.

28. Rieppo R, Holmberg P, 7 4, Int. J . Appl. Radiat. Isotope,s, 25, 188.: **Calculated efficiency values for Nal-detectors and some applications**. *International Journal of Applied Radiation and Isotopes* 1974, **25**:188.

29. Anonymous: **Future of nuclear medicine, part 2: Assessment of the U.S. diagnostic radiopharmaceuticals market (2001-2002)**. *The Journal of Nuclear Medicine* 1998, **39**(3):20N-25N.

30. Veall N: **40 years of development in radioisotope imaging**. *Physics in Medicine and Biology* 1984, **29**(2):163.

31. Bushberg JT, Seibert JA, Leidholdt Jr EM, Boone JM: **Image Quality**. In: *The Essential Physics of Medical Imaging.* Edited by John J-R. Philadelphia: Lippencott Williams & Wilkins; 2002: 255-291.

32. Anger HO: **Scintillation camera**. *Review of Scientific Instruments* 1958, **29**(1):27-33.

33. Nichols KJ, Bacharach SL, Bergmann SR: **Instrumentation quality assurance and performance**. *Journal of Nuclear Cardiology* 2006, **13**:25-41.

34. Friel H-I: **Nuclear medical diagnotics**. In: *Imaging Systems for Medical Diagnostics.* Edited by Krestel E, 2 edn. Berlin and Munich: Siemens Aktiengesellschaft; 1990.

35. Ott RJ, Flower MA, Babich JW, Marsden PK: **Table 6.1: Physical properties of inorganic scintillators**. In: *The Physics of Medical Imaging.* Institute of Physics; 1988.

36. NEMA: **Standards Publication NU 1-2001: Performance Measurements of Scintillation Cameras**. In: *Performance Measurements of Scintillation Cameras.* National Electrical Manufacturers Association; 2001.

37. Strand S-E: **The scintillation camera - basic principles**. In: *Monte Carlo Calculations in Nuclear Medicine: Applications in diagnostic imaging.* Edited by Ljungberg M, Strand S-E, King MA, vol. 1. Bristol and Philadelphia: Institute of Physics; 1998.

38. Sanchez-Crespo A, Persson L, Jonsson C, Larsson SA: **Photon Depth of Interaction in Various Scintillation Crystals and Its Influence on PET Image Spatial Resolution**. *IEEE Nuclear Science Symposium Conference Record* 2004, **4**:2589-2590.

39. Bombardieri J, Rosenfeld D: **On the performance of scintillation detectors for nuclear imaging**. *Proceedings of SPIE - The International Society for Optical Engineering* 1986, **671**:214-229.

40. Antich P, Malakhov N, Parkey R, Slavin N, Tsyganov E: **3D position readout from thick scintillators**. *Nuclear Instruments and Methods in Physics Research Section A: Accelerators, Spectrometers, Detectors and Associated Equipment* 2002, **480**(2-3):782-787.

41. Zasadny KR, Koral KF, Swailem FM: **Dead time of an anger camera in dual-energy-window-acqusition mode**. *Medical Physics* 1993, **20**(4):1115-1120.

42. Koral KF, Zasadny KR, Ackermann R: **Deadtime correction for two multihead Anger cameras in I-131 dual-energy-window-acquisition mode**. *Medical Physics* 1998, **25**:85-91.

43. Raeside DE: **Monte Carlo Principles and Applications**. *Physics in Medicine and Biology* 1976, **21**(2):181-197.

44. Andreo P: **Monte Carlo techniques in medical radiation physics**. *Physics in Medicine and Biology* 1991, **36**(7):861-920.

45. Manno I: **Introduction to the Monte Carlo method**. Budapest: Akadémiai Kiadó; 1999.

46. Bielajew, AF **Fundamentals of the Monte Carlo method for neutral and charged particle transport.** Accessed April 2007, *http://www.bhargav.com/books/Physics/Fundamentals_of_the_Monte_Carlo_Method_for_Neutral_and_Charged_Particle_Transport.pdf*

47. Lomsky M, Richter J, Johansson L, El-Ali H, Åstrom K, Ljungberg M, Edenbrandt L: **A new automated method for analysis of gated-SPECT images based on a three-dimensional heart shaped model**. *Clinical Physiological and Functional Imaging* 2005, **25**:234-240.

48. Berger MJ: **Monte Carlo calculation of the penetration and diffusion of fast charged particles**. *Methods in Computational Physics* 1963, **1**:135-215.

49. Berger MJ, Seltzer SM: **Response functions for sodium iodide scintillation detectors**. *Nuclear Instruments and Methods* 1972, **104**(2):317-332.

50. Chen CS, Doi K, Vyborny C, Chan H-P, Holje G: **Monte Carlo simulation studies of detectors used in the measurement of diagnostic x-ray spectra**. *Medical Physics* 1980, **7**(6):627-635.

51. Armstrong TW, Chandler KC: **Stopping powers and ranges for muons, charged pions, protons, and heavy ions**. *NUCLINSTRUMMETH* 1973, **113**(2):313-314.

52. Lal B, Iyengar KVK: **Monte Carlo calculations of gamma ray response characteristics of cylindrical GE(Li) detectors**. *Nuclear Instruments and Methods* 1970, **79**(1):19-28.

53. Steyn JJ, Andrews DG, Dixmier M: **Collimated detector response to point, line and plane sources**. *Nuclear Instruments and Methods* 1969, **74**(1):123-131.

54. Van Hemert RL, Bowman CD, Baglan RJ, Berman BL: **New detector for keV neutrons**. *Nucl Instrum Methods* 1970, **89**:263-275.

55. Walsh PJ: **Stopping power and range of alpha particles**. *Health Physics* 1970, **19**(2):312-316.

56. Baker RG, Scrimger JW: **An Investigation of the Parameters in Scintillation Camera Design**. *Physics in Medicine and Biology* 1967, **12**(1):51-63.

57. Daube-Witherspoon ME, Zubal IG, Karp JS: **Developments in instrumentation for emission computed tomography**. *Seminars in Nuclear Medicine* 2003, **33**(1):28-41.

58. Macey DJ: **The Uniformity of Gamma Cameras**. *Physics in Medicine and Biology,* 1972, **17**:857-858.

59. Muehllehner G, Luig H: **Septal Penetration in Scintillation Camera Collimators**. *Physics in Medicine and Biology* 1973, **18**(6):855-862.

60. Yap KK, H B Toh MW, Rowe CC, Health A: **Dual tracer parathyroid imaging - should pertechnetate imaging of the thyroid be performed before or after sestamibi - registrar's award**. *Internal Medicine Journal* 2005, **35**(s1):E1-E33.

61. Moore SC, Ouyang J, Park MA, El Fakhri G: **Monte Carlo-based compensation for patient scatter, detector scatter, and crosstalk contamination in In-111 SPECT imaging**. *Nuclear Instruments and Methods in Physics Research, Section A: Accelerators, Spectrometers, Detectors and Associated Equipment* 2006, **569**(2):472-476.

62. De Vries DJ, Moore SC, Zimmerman RE, Mueller SP, Friedland B, Lanza RC: **Development and Validation of a Monte Carlo Simulation of Photon Transport in an Anger Camera**. *IEEE Transactions on Medical Imaging* 1990, **9**(4):430-438.

63. Ljungberg M: **The SIMIND Monte Carlo program**. In., 4.5 edn; 1989.

64. Harrison RL, Haynor DR, Gillispie SB, Vannoy SD, Kaplan MS, Lewellen TK: **A public-domain simulation system for emission tomography: photon tracking through heterogeneous attenuation using importance sampling**. *The Journal of Nuclear Medcine* 1993, **34**(5):60.

65. Baró J, Sempau J, Salvat F, Fernández-Varea JM: **PENELOPE: An algorithm for Monte Carlo simulation of the penetration and energy loss of electrons and positrons in matter**. *Nuclear Instruments and Methods in Physics Research Section B* 1995, **100**:31-46.

66. Ljungberg M, Strand S-E: **Attenuation and scatter correction in SPECT for sources in a nonhomogeneous object: A Monte Carlo study**. *The Journal of Nuclear Medicine* 1990, **32**(6):1278-1284.

67. Ljungberg M, Strand S-E: **Attenuation correction in SPECT based on transmission studies and Monte Carlo simulations of build-up functions**. *The Journal of Nuclear Medicine* 1989, **31**:493-500.

68. Ljungberg M, Larsson A, Johansson L: **A new collimator simulation in SIMIND based in the delta scattering technique**. *IEEE Transactions on Nuclear Science* 2004.

69. Jonsson L, Ljundberg M, Strand S-E: **Evaluation of accuracy in activity calculations for the conjugate view method from Monte Carlo simulated scintillation camera images using experimental data in an anthropormorphic phantom**. *The Journal of Nuclear Medicine* 2005, **46**(10):1679-1686.

70. Dewaraja YK, Ljungberg M, Majumdar A, Bose A, Koral K: **A parallel Monte Carlo code for planar and SPECT imaging: implementation, verification and applications in I-131 SPECT**. *Computer Methods and Programs in Biomedicine* 2002, **67**(2):115-124.

71. ICRU: **Phantoms and computational models in therapy, diagnosis and protection**. In: *report 48.* Edited by ICRU. Bethesda: International Commission on Radiation Units and Measurements, ICRU report 48; 1992.

72. Lee C, Lee J-K: **Computational anthropomorphic phantoms for radiation protection dosimetry: evolution and prospects**. *Nuclear Engineering and Technology* 2006, **38**(3):239-250.

73. Hayes R, Brucer M: **Compartimentalized phantoms for the standard man, adolescent and child**. *International Journal of Applied Radiation and Isotopes* 1960, **9**:113.

74. Dosimetry I: **Fisher-Snyder Phantom**. Accessed 2007 http://www.internaldosimetry.com/courses/intromonte/images/figure5.gif.

75. Gibbs SJ, Pujol A, Chen TS, Malcom AW, James AE: **Computer simulation of patient dose from dental radiography**. *Journal of Dental Research* 1984, **63**:209.

76. Veit R, Zankl M, Petoussi N, Mannweiler E, Williams G, Drexler G: **Tomographic anthropomorphic models, Part I: Construction technique and desecription of models of an 8-week-old baby and a 7-year-old child**. GSF-National Research Center for Environment and Health, GSF-Report 3/89; 1989.

77. Zubal I, Harell C, Smith E, Rattner Z, Gindi G, Hoffer P: **Computerized 3-Dimensional segmented human anatomy**. *Medical Physics* 1994, **21**:299.

78. Sjogreen K, Stuchly MA: **Zubal Phantom**. Accessed 2007 http://noodle.med.yale.edu/zubal/samples.htm.

79. Segars WP: **Development of a new dynamic NURBS-based cardiac-torso (NCAT) phantom**. PhD dissertation. Chapel Hill: University of North Carolina; 2001.

80. Segars WP: **The extended 4D NCAT phantom**. Used with permission from http://dmip.rad.jhmi.edu/people/faculty/Paul/Segars_research.htm#NCAT; 2007.

81. Segars WP, Lalush DS, Tsui BMW: **Development of an interactive software application to model patient populations in the 4D NURBS-based Cardiac Torso phantom**. In: *IEEE Nuclear Science Symposium and Medical Imaging Conference: 2000*; 2000: 20/51-20/55.

82. Segars WP, Mahesh M, Beck T, Frey EC, Tsui BMW: **Validation of the 4D NCAT simulation tools for use in high-resolution x-ray CT research**. In: *Progress in Biomedical Optics and Imaging - Proceedings of SPIE: 2005*; 2005: 828-834.

83. Segars WP, Taguchi K, Fung GSK, Fishman EK, Tsui BMW: **Effect of heart rate on CT angiography using the enhanced cardiac model of the 4D NCAT**. In: *Progress in Biomedical Optics and Imaging - Proceedings of SPIE: 2006*; 2006.

84. Segars WP, Tsui BMW, Frey EC, Fishman EK: **Extension of the 4D NCAT phantom to dynamic X-ray CT simulation**. In: *IEEE Nuclear Science Symposium Conference Record: 2003*; 2003: 3195-3199.

85. Lee TS, Segars WP, Tsui BMW: **A study of the effect of cardiac gating in myocardial SPECT using the 4D NCAT**. In: *IEEE Nuclear Science Symposium Conference Record: 2003*; 2003: 2681-2685.

86. Segars WP, Tsui BMW: **Study of the efficacy of respiratory gating in myocardial SPECT using the new 4-D NCAT phantom**. *IEEE Transactions on Nuclear Science* 2002, **49 I**(3):675-679.

87. Baird WH, Frey EC, Tsui BMW, Wang Y, Wessell DE: **Evaluation of rotating slant-hole SPECT mammography using Monte-Carlo simulation methods**. In: *IEEE Nuclear Science Symposium and Medical Imaging Conference: 2001*; 2001: 1331-1334.

88. Liu C, Tsui BMW, Baird WH, Xu J, Wang Y, Frey EC: **Evaluation of rotating slant hole SPECT mammography with respect to planar scintimammography using Monte Carlo simulation methods**. In: *IEEE Nuclear Science Symposium Conference Record: 2004*; 2004: 4063-4067.

89. He X, Fey EC, Links JM, Gilland KL, Segars WP, Tsui BMW: **A mathematical observer study for the evaluation and optimization of compensation methods**

for myocardial SPECT using a phantom population that realistically models patient variability. *IEEE Transactions on Nuclear Science* 2004, **51**(1):218-224.

90. He B, Frey E: **Comparison of conventional, model-based quantitative planar, and quantitative SPECT image processing methods for organ activity estimation using In-111 agents**. *Physics in Medicine and Biology* 2006, **51**:3967-3981.

91. Naddaf SY, Collier BD, Elgazzar AH, Khalil MM: **Technical errors in planar bone scanning**. *The Journal of Nuclear Medicine Technology* 2004, **32**(3):148-153.

92. Gates GF: **SPECT bone scanning of the spine**. *Seminars in Nuclear Medicine* 1998, **28**(1):78-94.

93. Nuclear Medicine: **Bone Scan Imaging Procedures**. Christchurch Public Hospital Clinical Guidelines, 2005.

94. ImageJ: **http://rsb.info.nih.gov/ij/index.html**. In., 1.37 edn: National Institute of Health; 2006.

95. Siegel JA, Thomas SR, Stubbs JB, Stabin MG, Hays MT, Koral KF, Robertson JS, Howell RW, Wessels BW, Fisher DR *et al*: **MIRD pamphlet No. 16: Techniques for quantitative radiopharmaceutical biodistribution Data Acquisition and Analysis for use in Human Radiation Dose Estimates**. *The Journal of Nuclear Medcine* 1999, **40**(2):37S.

96. ICRP 53: **Radiation Dose to Patients from Radiopharmaceuticals**. In.: International Commission on Radiological Protection; 1988: 213-214.

97. Moore DS, McCabe GP: **Multiple regression**. In: *Introduction to the Practice of Statistics.* Edited by Maass DC, 3rd edn. New York: W. H. Freeman and Company; 1998.

98. Bevington PR, Robinson DK: **Data Reduction and Error Analysis for the Physical Sciences**, 2nd edn. New York: McGraw-Hill, Inc.; 1992.

99. Crawley MJ: **Statistical Computing: an introduction to data analysis using S-Plus**, 1st edn. New York: Wiley; 2002.

100. Cohen JL: **Pharmacokinetic changes in aging**. *The American Journal of Medicine* 1986, **80**(5):31-38.

101. Vestal RF: **Pharmacology and aging**. *Journal of the American Geriatrics Society* 1982, **30**(3):191-200.

102. IAEA: **X-ray and Gamma-ray Decay Data Standards for Detector Calibration and Other Applications: URL http://www-nds.iaea.org/xgamma_standards/**. In.: IAEA; 2005.

103. GE: **Product Data: MPR Collimators**. In.; 1997.

104. Floyd CE, Jaszczak RJ, Harris CC, Greer KL, Coleman RE: **Monte Carlo evaluation of Compton scatter subtraction in single photon emission tomography**. *Medical Physics* 1985, **12**(6):776-778.

105. Ljungberg M: **Personal communcation with M Ljungberg**. In. Edited by McGurk R. Christchurch; 2007.

106. O'Keefe D: **ReadSpectrum.m**. In.; 2005.

107. Gallardo S, Ródenas J, Verdú G, Villaescusa JI: **Analysis of shielding materials in a Compton spectrometer applied to x-ray tube quality control using Monte Carlo simulation**. *Radiation Protection Dosimetry* 2005, **115**(1-4):375-379.

108. Baggethun P: **Radial Profile Plot**. ImageJ Plugin. Pittsburgh, PA; 2002.

109. Segars WP, Tsui BMW, Da Silva AJ, Shao L: **CT-PET Image Fusion using the 4D NCAT Phantom with the Purpose of Attenuation Correction**. In: *IEEE Nuclear Science Symposium and Medical Imaging Conference: 2002*; 2002: 1775-1779.

110. Thireou T, Rubio Guivernau JL, Atlamazoglou V, Ledesma MJ, Pavlopoulos S, Santos A, Kontaxakis G: **Evaluation of data reduction methods for dynamic PET series based on Monte Carlo techniques and the NCAT phantom**. *Nuclear Instruments and Methods in Physics Research, Section A: Accelerators, Spectrometers, Detectors and Associated Equipment* 2006, **569**(2 SPEC. ISS.):389-393.

111. Veress AI, Segars WP, Weiss JA, Tsui BMW, Gullberg GT: **Normal and pathological NCAT image and phantom data based on physiologically realistic left ventricle finite-element models**. *IEEE Transactions on Medical Imaging* 2006, **25**(12):1604-1616.

112. Johns HE, Cunningham JR: **The Physics of Radiology**, 4th edn. Springfield, Illinois: Charles C Thomas; 1983.

113. Ljungberg M: **The SIMIND Monte Carlo Program**. In: *Monte Carlo Techniques in Nuclear Medicine: Applications in diagnostic imaging.* Edited by Ljungberg M, Strand S-E, King MA. Bristol: Institute of Physics; 1998.

Appendix A

Raw data from the clinical study

MALES

Patient ID	Age	Height	Weight	Dispensed activity	Dispense-Injection	Injected Activity	Injection-scan time	Scan Activity				WB Image Counts		ICRP Normalised counts	
								Physical	Skeleton	ICRP	Soft	Anterior	Posterior	Anterior	Posterior
07SC287A	72	169.50	92.00	789	0.45	749	195.00	542	306	309	4	2809823	2697169	9083	8719
07SC294A	64	177.50	107.50	753	0.17	739	207.00	506	289	289	0	2103501	1990133	7272	6880
07SC300U	65	170.50	88.00	805	1.17	704	199.00	548	310	313	3	2204581	2081728	7045	6652
07SC301V	76	177.60	91.00	835	0.90	753	185.00	584	326	333	7	3044981	2910078	9137	8732
07SC316G	67	171.00	82.00	815	1.32	700	167.00	590	323	337	14	3052601	2766576	9053	8204
07SC318I	74	171.80	91.50	716	0.57	671	205.00	483	275	276	1	2282015	2110814	8275	7654
07SC323G	61	174.00	93.00	884	1.63	732	197.00	604	341	345	3	2260305	2245443	6560	6517
07SC340J	70	175.50	81.00	788	0.68	728	214.00	522	300	299	-1	2427041	2259619	8119	7559
07SC344N	72	187.40	74.50	872	1.88	702	193.00	600	338	342	5	2382284	2276969	6962	6654
07SC349S	53	172.90	100.00	717	0.08	710	189.00	499	279	284	5	2341640	2216041	8233	7791
07SC350M	67	174.90	79.50	754	0.57	706	209.00	504	289	288	0	2406839	2330849	8344	8081
07SC358U	41	181.6	65.00	794	0.73	730	204.00	536	305	306	1	2090116	1989119	6825	6495
07SC371T	60	178.50	76.00	755	0.97	675	222.00	492	286	283	-3	2049847	1913395	7253	6770
07SC379E	76	170.30	74.00	828	1.48	698	227.00	534	312	307	-5	2671002	2425026	8692	7891
07SC393E	85	170.90	80.00	770	0.13	758	167.00	559	306	319	13	4074736	4138477	12761	12960
07SC429R	64	168.10	57.00	758	0.35	728	213.00	503	289	288	-1	2237549	2212410	7764	7677
07SC433O	84	167.20	81.00	757	0.68	700	179.00	536	297	306	9	4075030	3615026	13324	11820
07SC441P	80	168.30	62.50	749	0.78	684	191.00	518	291	296	5	2794783	2773452	9454	9382
07SC464B	55	186.8	94.00	776	1.20	676	168.00	561	308	320	13	2217722	2073229	6921	6470
07SC467E	68	176.10	93.00	808	1.47	682	194.00	555	313	317	4	2094701	2022237	6613	6384
07SC499P	56	179.20	83.50	769	0.73	707	186.00	537	300	306	6	2453617	2279177	8007	7438
07SC504L	77	171.20	84.00	833	1.65	689	193.00	573	323	327	4	2686246	2736078	8214	8367
07SC546C	72	171.80	79.00	759	0.87	687	234.00	484	285	279	-6	2169619	1999641	7773	7164
07SC553C	50	159.80	85.00	766	1.63	635	189.00	531	298	303	5	1531292	1550684	5054	5118
07SC576L	64	177.10	84.00	781	1.32	671	199.00	532	301	304	2	1891461	1943498	6232	6403
07SC578N	60	175.90	84.00	777	0.67	720	228.00	501	293	288	-5	1929683	1846983	6691	6405
07SC644F	69	175.00	80.00	819	1.42	696	177.00	582	322	332	10	2617430	2338295	7890	7048
07SC651F	77	172.00	72.00	767	0.35	737	210.00	512	294	293	0	2913796	2655204	9943	9060
Mean	67.11	174.01	82.64	785.50	0.92	705.97		537	304	307	3	2472424	2361687	8125	7725
Std deviation	10.5	6.0	11.2	41.3	0.5	29.3		35	17	20	5	587233	556681	1796	1682
Minimum	41	160	57	716	0	635		483	275	276	-6	1531292	1550684	5054	5118
Maximum	85	187	108	884	2	758		604	341	345	14	4075030	4138477	13324	12960

FEMALES

								Scan Activity				WB Image Counts		ICRP Normalised	
Patient ID	Age	Height	Weight	Dispensed activity	Dispense-Injection time	Injected Activity	Injection-scan time	Physical	ICRP Bone	ICRP Total	Body activity	Anterior	Posterior	Anterior	Posterior
07SC267R	73	157.4	74.50	809	0.48	808	206.00	544	314	311	-2.846	2522068	2516070	8107	8088
07SC270N	52	172.5	63.00	797	0.80	796	212.00	530	308	303	-4.457	2368442	2360161	7810	7783
07SC315F	66	149.0	41.00	826	1.38	824	187.00	575	325	328	3.251	3548973	3243342	10817	9885
07SC321E	60	151.8	68.00	839	0.80	838	189.00	583	330	332	2.588	2547601	2479519	7665	7460
07SC335L	67	163.6	93.00	777	0.50	776	205.00	524	302	299	-2.455	2105968	2032836	7036	6792
07SC343M	59	167.0	60.00	826	1.47	824	190.00	572	324	326	2.197	2414042	2272183	7401	6966
07SC353P	35	165.9	62.50	756	0.88	734	195.00	505	288	288	0.458	2269141	2112910	7877	7335
07SC375A	59	151.0	55.00	776	2.08	752	178.00	535	299	305	6.056	2039610	1901113	6688	6234
07SC395G	49	163.0	58.00	771	1.33	769	185.00	539	304	307	3.709	2523537	2299924	8208	7480
07SC397I	87	153.1	65.00	745	1.37	743	167.00	539	298	308	10.171	2948347	2934183	9566	9520
07SC401D	56	173.0	61.00	798	1.15	796	197.00	546	311	311	-0.131	2940777	2675867	9446	8595
07SC407J	43	166.8	79.00	743	0.52	742	159.00	547	300	313	13.587	1676731	1636951	5349	5222
07SC419O	66	158.2	64.00	820	1.33	818	148.00	616	334	355	20.875	2452643	2295620	6916	6473
07SC422K	53	162.8	75.00	838	1.98	835	170.00	602	334	344	10.080	2418310	2115753	7029	6149
07SC448W	67	155.3	46.00	757	1.25	735	188.00	512	289	292	2.582	2568970	2472263	8798	8466
07SC451S	69	160.1	48.00	777	1.32	754	181.00	533	299	304	5.006	3914866	3659672	12878	12039
07SC474E	76	156.2	53.50	768	1.10	746	193.00	515	293	294	1.065	2642233	2469908	8996	8409
07SC475F	74	165.0	69.00	758	0.53	737	202.00	500	287	285	-1.522	2294225	2146652	8036	7519
07SC483G	54	162.4	62.00	748	0.72	726	216.00	480	280	275	-5.030	2077194	1919993	7553	6981
07SC491H	67	166.0	52.00	740	0.18	719	187.00	502	284	286	2.838	3323016	3102443	11602	10832
07SC492I	61	163.3	77.00	750	0.35	729	191.00	505	286	288	1.640	2638830	2462569	9159	8547
07SC493J	25	156.7	56.50	737	0.55	716	203.00	485	279	277	-1.742	1968496	1935109	7110	6989
07SC497N	57	158.6	83.00	738	0.52	717	166.00	521	288	298	10.205	2532999	2327705	8502	7813
07SC502J	81	163.0	65.00	813	1.50	790	189.00	550	311	313	2.441	3084772	2932590	9841	9355
07SC518S	63	165.9	92.00	795	1.50	772	223.00	503	296	289	-7.048	1859071	1779924	6430	6156
07SC520N	39	166.5	60.00	760	1.03	738	216.00	488	284	279	-5.109	2167652	2077620	7759	7437
07SC522P	58	167.3	70.00	810	1.28	787	217.00	519	303	298	-5.707	2305648	2146892	7746	7213
07SC525S	73	144.5	84.00	770	1.02	748	207.00	503	290	287	-2.899	2390163	2185443	8317	7605
07SC531R	62	169.0	69.50	725	0.55	704	165.00	513	283	293	10.413	2933902	2671642	10008	9114
07SC540T	47	168.0	92.00	884	1.80	860	189.00	599	339	341	2.658	1752517	1677066	5134	4913
07SC549F	39	168.7	98.00	759	0.70	737	223.00	481	283	276	-6.731	1731796	1538347	6272	5571
07SC573I	67	163.2	104.00	970	0.08	949	174.00	680	378	388	9.506	3488767	3186932	8993	8215
07SC589R	64	157.6	46.00	758	0.93	736	188.00	513	290	293	2.588	2871229	2857181	9813	9765
07SC592N	64	158.0	81.00	720	0.42	699	194.00	482	274	275	0.716	2629610	2386073	9572	8686
07SC643E	54	159.0	66.00	774	1.25	752	175.00	537	299	307	7.151	2228309	2077594	7270	6778
07SC645G	72	164.4	82.00	836	1.52	813	199.00	555	317	317	-0.761	2356361	2249848	7440	7103
07SC648J	40	162.5	61.50	822	1.88	798	197.00	547	312	312	-0.131	2242004	2054952	7182	6583
Mean	59.41	161.52	68.57	786.22	1.03	770.73	191.11	535	303	305	2.30	2528004	2376837	8225	7732
Std deviation	13.31	6.71	15.75	49.95	0.50	52.85	18.48	44.09	21.30	24.17	6.12	528428	489338	1658	1549
Minimum	25	145	41	720	0	699	148	480	274	275	-7	1676731	1538347	5134	4913
Maximum	87	173	104	970	2	949	223	680	378	388	21	3914866	3659672	12878	12039

Appendix B

Clinical Trial AIC analysis

Best Fit
Anterior Analysis

```
      Source |       SS       df       MS              Number of obs =      65
-------------+------------------------------           F(  6,    58) =   13.95
       Model |   116617947     6  19436324.6           Prob > F      =  0.0000
    Residual |  80805277.5    58  1393194.44           R-squared     =  0.5907
-------------+------------------------------           Adj R-squared =  0.5484
       Total |   197423225    64  3084737.89           Root MSE      =  1180.3
------------------------------------------------------------------------------
         ant |      Coef.   Std. Err.      t    P>|t|     [95% Conf. Interval]
-------------+----------------------------------------------------------------
           s |  -8245.221   2894.861    -2.85   0.006    -14039.91   -2450.527
           a |   65.06357   67.42784     0.96   0.339    -69.90791    200.0351
           w |  -65.81197   60.68389    -1.08   0.283     -187.284    55.66004
          sa |   63.54738   28.92931     2.20   0.032     5.639068    121.4557
          sw |   49.90918   24.72871     2.02   0.048     .4092928    99.40906
          aw |   .0083381    .984421     0.01   0.993    -1.962195    1.978871
       _cons |   9866.491   4169.518     2.37   0.021     1520.293    18212.69
------------------------------------------------------------------------------
------------------------------------------------------------------------------
       Model |    Obs    ll(null)   ll(model)     df          AIC         BIC
-------------+----------------------------------------------------------------
           . |     65   -577.3414   -548.3089      7     1110.618    1125.838
------------------------------------------------------------------------------
```

Posterior Analysis

```
      Source |       SS       df       MS              Number of obs =      65
-------------+------------------------------           F(  6,    58) =   16.93
       Model |   107989180     6  17998196.6           Prob > F      =  0.0000
    Residual |  61667184.3    58  1063227.32           R-squared     =  0.6365
-------------+------------------------------           Adj R-squared =  0.5989
       Total |   169656364    64  2650880.69           Root MSE      =  1031.1

------------------------------------------------------------------------------
         pos |      Coef.   Std. Err.      t    P>|t|     [95% Conf. Interval]
-------------+----------------------------------------------------------------
           s |  -7374.622   2528.919    -2.92   0.005     -12436.8   -2312.441
           a |   56.31172   58.90422     0.96   0.343    -61.59789    174.2213
           w |  -72.02218   53.01279    -1.36   0.180    -178.1388    34.09444
          sa |   54.34536   25.27233     2.15   0.036     3.757287    104.9334
          sw |   47.96459   21.60273     2.22   0.030     4.722036    91.20715
          aw |   .1294645   .8599794     0.15   0.881    -1.591971      1.8509
       _cons |   9763.234   3642.446     2.68   0.010     2472.087    17054.38
------------------------------------------------------------------------------
------------------------------------------------------------------------------
       Model |    Obs    ll(null)   ll(model)     df          AIC         BIC
-------------+----------------------------------------------------------------
           . |     65   -572.4152   -539.5244      7     1093.049     1108.27
```

Height and weight fit

Anterior Analysis

```
      Source |       SS       df       MS              Number of obs =      65
-------------+------------------------------           F(  2,    62) =    6.80
       Model |  35529497.7     2  17764748.9           Prob > F      =  0.0021
    Residual |   161893727    62  2611189.15           R-squared     =  0.1800
-------------+------------------------------           Adj R-squared =  0.1535
       Total |   197423225    64  3084737.89           Root MSE      =  1615.9

------------------------------------------------------------------------------
         ant |      Coef.   Std. Err.      t    P>|t|     [95% Conf. Interval]
-------------+----------------------------------------------------------------
           h |  -8.432797   26.07099    -0.32   0.747    -60.54795    43.68236
           w |  -46.51582   14.96257    -3.11   0.003    -76.42556   -16.60607
       _cons |   14016.02   3965.964     3.53   0.001     6088.168    21943.87
------------------------------------------------------------------------------
------------------------------------------------------------------------------
       Model |    Obs    ll(null)   ll(model)     df          AIC         BIC
-------------+----------------------------------------------------------------
           . |     65   -577.3414   -570.8931      3     1147.786    1154.309
------------------------------------------------------------------------------
```

Posterior Analysis

```
      Source |       SS       df       MS              Number of obs =      65
-------------+------------------------------           F(  2,    62) =    7.17
       Model |  31861000.9     2  15930500.5           Prob > F      =  0.0016
    Residual |   137795363    62  2222505.85           R-squared     =  0.1878
-------------+------------------------------           Adj R-squared =  0.1616
       Total |   169656364    64  2650880.69           Root MSE      =  1490.8

------------------------------------------------------------------------------
         pos |      Coef.   Std. Err.      t    P>|t|     [95% Conf. Interval]
-------------+----------------------------------------------------------------
           h |  -5.318792   24.05247    -0.22   0.826      -53.399    42.76142
           w |   -44.8559   13.80411    -3.25   0.002    -72.44991   -17.26188
       _cons |   12865.66   3658.904     3.52   0.001     5551.615    20179.71
------------------------------------------------------------------------------
------------------------------------------------------------------------------
       Model |    Obs    ll(null)   ll(model)     df          AIC         BIC
-------------+----------------------------------------------------------------
           . |     65   -572.4152    -565.655      3      1137.31    1143.833
------------------------------------------------------------------------------
```

Appendix C

General Settings for the SIMIND CHANGE program

1.	Write Results to the Screen	>	TRUE
2.	Write Image Matrix to File	>	TRUE
3.	Write Pulse-Height Distribution to File	>	TRUE
4.	Include the Collimator	>	TRUE
5.	Simulate a SPECT Study	>	FALSE
6.	Include Characteristic X-Ray Emission	>	TRUE
7.	Include Backscattering Material	>	TRUE
8.	Use a Random Sampled Seed Value	>	TRUE
9.	Simulate a Transmission Study	>	FALSE
10.	Include Interactions in the Cover	>	TRUE
11.	Include Interactions in the Phantom	>	TRUE
12.	Include Simulation of Energy Resolution	>	TRUE
13.	Include Forced Interaction at Crystal Entry	>	TRUE
14.	Write File Header in INTERFILE V3.3 Format	>	FALSE
15.	Save Aligned Density Map	>	FALSE

Default Settings for the Millennium MG

8.	Crystal: Half-Length/Radius	cm >	19.000
9.	Crystal: Thickness	cm >	0.900
10.	Crystal: Half-Width..[0 = Circular]	cm >	26.800
11.	Backscattering Material: Thickness	cm >	4.000
13.	Thickness of Cover	cm >	0.100
19.	Photon Direction	deg >	1
20.	Upper Window Threshold	% >	-20
27.	keV / Channel	keV >	0.352
28.	Pixel Size in simulated image	cm >	0.226

Default Collimator Settings

46.	Hole Size X	cm >	0.180
47.	Hole Size Y	cm >	0.300
48.	Distance between two holes: X direction	cm >	0.018
49.	Distance between two holes: Y direction	cm >	0.120
50.	Displacement center hole: X direction	cm >	0.009
51.	Displacement center hole: Y direction	cm >	0.167
52.	Collimator Thickness	cm >	4.2
54.	Shape: 1=Triang, 2=Ellipt, 3=Hexa, 4=Rect	>	3
55.	Coll Type: 0=PA, 1=SH, 2=CO, 3=FB, 4=DI	>	0
59.	Move the Collimator	(0=no, 1=yes) >	0

Detector Specific Settings

Detector 1

22.	Energy Resolution [140 keV]	% >	8.99
23.	Intrinsic Resolution [140 keV]	cm >	0.377

Detector 2

22.	Energy Resolution [140 keV]	% >	8.61
23.	Intrinsic Resolution [140 keV]	cm >	0.374

Appendix D

Specific source and phantom dimensions used in this study

Tc-99m point source

1.	Photon energy	kev >	140.50
2.	Source: Half Length Source	cm >	0.500
3.	Source: Half Width Source	cm >	0.400
4.	Source: Half Height Source	cm >	0.400
5.	Phantom: Half Length Phantom	cm >	0.500
6.	Phantom: Half Width Phantom	cm >	0.500
7.	Phantom: Half Height Phantom	cm >	0.500
12.	Height to Detector Surface	cm >	1800
14.	Source Type		4.000
15.	Phantom Type		4.000
16.	Shift Source in X direction	cm >	2.500
25.	Source Activity	MBq >	6.350
	Emitted photons per decay		0.885

Co-57 point source

1.	Emitted photons per decay (via isotop subroutine)		14.41 keV	0.092
			122.06 keV	0.855
			136.47 keV	0.107
2.	Source: Half Length Source	cm >		0.250
3.	Source: Half Width Source	cm >		0.150
4.	Source: Half Height Source	cm >		0.150
5.	Phantom: Half Length Phantom	cm >		0.300
6.	Phantom: Half Width Phantom	cm >		0.200
7.	Phantom: Half Height Phantom	cm >		0.200
12.	Height to Detector Surface	cm >		1800
14.	Source Type			3.000
15.	Phantom Type			3.000
16.	Shift Source in X direction	cm >		0.000
25.	Source Activity	MBq >		0.544

Nuclear Associates “Line Source” phantom

1.	Photon energy	kev >	140.50
2.	Source: Half Length Source	cm >	10.000
3.	Source: Half Width Source	cm >	0.050
4.	Source: Half Height Source	cm >	0.050
5.	Phantom: Half Length Phantom	cm >	10.635
6.	Phantom: Half Width Phantom	cm >	10.000
7.	Phantom: Half Height Phantom	cm >	10.000
12.	Height to Detector Surface	cm >	varies
14.	Source Type		3.000
15.	Phantom Type		3.000
16.	Shift Source in X direction	cm >	0.000
25.	Source Activity	MBq >	183.780

IEC “Count Rate Performance in Scatter” Insert

1.	Photon energy	keV >	140.5
2.	Source: Half Length Source	cm >	7.500
3.	Source: Half Width Source	cm >	7.500
4.	Source: Half Height Source	cm >	0.500
5.	Phantom: Half Length Phantom	cm >	8.500
6.	Phantom: Half Width Phantom	cm >	8.500
7.	Phantom: Half Height Phantom	cm >	1.000
12.	Height to Detector Surface	cm >	varies
14.	Source Type		3.000
15.	Phantom Type		3.000
16.	Shift Source in X direction	cm >	0.000
25.	Source Activity	MBq >	varies

IEC “Count Rate Performance in Scatter” Outer Phantom

1.	Photon energy	keV >	140.5
2.	Source: Half Length Source	cm >	7.500
3.	Source: Half Width Source	cm >	7.500
4.	Source: Half Height Source	cm >	0.500
5.	Phantom: Half Length Phantom	cm >	15.000
6.	Phantom: Half Width Phantom	cm >	15.000
7.	Phantom: Half Height Phantom	cm >	6.500
12.	Height to Detector Surface	cm >	varies
14.	Source Type		3.000
15.	Phantom Type		3.000
16.	Shift Source in X direction	cm >	0.000
25.	Source Activity	MBq >	varies

Appendix E

SIMIND command line switches

/CC Collimator code according to the description in the CHANGE program. Note that you should not include the '*' as is necessary in the CHANGE. For example simind input/cc:ge-legp gives this collimator in the simulation regarding of what is given in the smc file[Character input]

/CS Collimator flag: Selects that only geometrical=1, penetration=2 or scattering=3 in the collimator are allowed.

/DF This switch is used when simulating heart beating and respiratory movements using MCAT/NCAT phantom. Since each segment from MCAT/NCAT has its own image file with a particular number this switch makes a patch to the file name of the density file. For example, suppose you have generated 8 segment of a beating heart using the base name "test". The output from NCAT give you files named test_act_1.bin, test_atn_2.bin,...test_atn_8.bin. If you add the switch /SF:3 then you will use the source map test_act_3.bin even if the input file says test. If this switch is not given then it will open the file test_atn_av.bin as is the standard name for the average source image from ncat

/ES Energy offset relative to Index 01 in keV for the center energy of the photo peak window. Negative value means lower value than index 1. If this shift is not given then the center value of the energy window is defined by index 1.

/FA This switch in combination with a number turns off the simulation flag for the corresponding number. For example /FA:5 turns of SPECT simulation. To set a flag to true then use the switch /TR

/FZ Give the name for the zubal file without the extension 'zub' [Character input]

/FI Give the name for the isotope file without the extension 'isd' [Character input]

/FD Base name for the density map (*.dmi) or the NCAT attenuation map[Character input]

/FS Base name for the source map (*.smi) or the NCAT activity map[Character input]

/I2 Image files are stored as integer*2 matrices. By default a scaling factor is calculated from the first projection so that the maximum in that projection will be 1000. If a data value is gives after /I2 then that value will be used as a scaling factor

/LO Number of photon histories before printout of the ongoing status line. Require a data value. The default is 1000.

/LF A samplings technique based on linear sampling of the polar angle for the photon direction is used. Note that this is only useful when simulating the simindc and the scattwinc programs with the new collimator.

/OR Parameter that changes the orientation of the density map. Value 2 transpose the maps, value 3 swaps the maps so index (1,1) is the lower left and value 4 both transpose and swaps.

/PR Start simulation at projection number given by the switch. Default value is projection 1.

/PU In some cases it is more convenient to express the centre of the source in terms of pixel unit instead for cm and let the computer calculate the physical centre position. By using the /PU (= pixel units) switch on can give the shift of the source in pixel units according to $ simind input/16:38/17:128/18:64/PU. From the phantom length and the density pixel size is calculated the true source shift in cm. If the command looks like $ simind input/16:38/17:128/18:64/PU:0.25 then the position is scaled down by a factor of four. It's used when the pixel units are valid for e.g. a 512 matrix but the actual density map used in the simulation is only a 128 matrix.

/QF Quit the simulation if an earlier result file exists. This flag is useful if a batch simulation has been ongoing and the computer has been restarted following a power-failure. This may then prevent recalculation of already existing data files.

/SC Maximum number of scatter orders allowed in the phantom. Require a data value. A large number requires more computing time since more multiple scattered photons will be followed in the phantom. In some case (for example, when simulating images obtained in a narrow energy window) a lower value may be sufficient since the lower energy photon with a low probability is rejected by the energy window. The user must therefore be careful so the proper number of scatter orders is simulated for the particular simulation. It can be necessary to do some 'trial-and-error' simulation. The default value is 3. If scatter order are a negative value the only the scatter distribution is simulated and stored in the images and spectrum.

/SW Swap the bytes in the integer image file created if the switch /I" have been given. The Interfile file key "number format" is properly set according to the computer that is used. For example, if running on a PC the number format will be BIGENDIAN if /SW is given and LITTLEENDIAN if the running computer is a SUN

/SF This switch is used when simulating heart beating and respiratoric movements using MCAT/NCAT phantom. Since each segment from MCAT/NCAT has its own image file with a particular number this switch makes a patch to the file name of the density file. For example, suppose you have generated 8 segment of a beating heart using the base name "test". The output from NCAT give you files named test_act_1.bin, test_act_2.bin,...test_act_8.bin. If you add the switch /SF:3 then you will use the source map test_act_3.bin even if the input file says test. If this switch is not given then it will open the file test_act_av.bin as is the standard name for the average source image from ncat

/TR: Turns on simulation flag corresponding to the number. For example, /TR:12 turns on simulation of the energy resolution.

/TS A time shift can be added to the date and time description in the interfile header. The initial time and date is set in the simind.ini file and the value of the /TS switch is the extension of this time expressed in hours. Note that it must be a positive value greater or equal to 0.s

/UA Set the density equal to the data buffer or if not present equal to 1.0 (=water). This makes the phantom equal to uniform attenuated regardless of the initial voxel value in the phantom.

/WB Whole Body Simulation of Anterior and Posterior view. Note that you might need to adjust the Matrix size with simparam and the detector length (index 8)..When this switch is given the following parameters is set
Number of projections = 2
Interfile = .true.
Phantom flag = .true.
Rotation type = 0 (360 degrees)

/XP Number of split photons emitted from the last interaction point in the phantom. This parameter can be used to increase the statistics in the images.

/Xn 'n' specifies the cross-section that can be changed. The X1-X5 refers to the index 9,10,11,12 and 15 in the main CHANGE menu and X6 is the material for the collimator when using the simindc, scattwinc.[Character input]

Appendix F

MATLAB code

Clinical study data analysis

```
%% Whole Body Bone Scan Research Study
%% PATIENT DATA ANALYSIS
%% Ross McGurk
%% July-September 2007

%%%%%%%%%%%%%%%%%%%%%%%%%%%%%%%%%%%%%%%%%%%%%%%%%%%%%%%%%%%%%%%%%%%%%%%%%%%%%%%%
%%%
% read in patient data
% data = [age sex height weight ant_counts pos_counts]
format short g
data=dlmread('NEW_FINAL_PATIENTS.txt');

%%%%%%%%%%%%%%%%%%%%%%%%%%%%%%%%%%%%%%%%%%%%%%%%%%%%%%%%%%%%%%%%%%%%%%%%%%%%%%%%
%%%
% rearrange the data matrix to find the correlations between variables
ant_correlation_matrix=[data(:,5) data(:,1) data(:,2) data(:,3)
data(:,4)];
pos_correlation_matrix=[data(:,6) data(:,1) data(:,2) data(:,3)
data(:,4)];

[ant_corr ant_pval]=corr(ant_correlation_matrix)
[pos_corr pos_pval]=corr(pos_correlation_matrix)

%
%%%%%%%%%%%%%%%%%%%%%%%%%%%%%%%%%%%%%%%%%%%%%%%%%%%%%%%%%%%%%%%%%%%%%%%%%%%%%%%%
%%%
% %% Plot the variables that show statistically significant
correlations
figure(1)
subplot(2,2,1)
scatter(data(:,1),data(:,5))
xlabel('Age','Fontsize',14); ylabel('Counts/MBq','Fontsize',14)
legend('r=0.5470','Location','NorthWest')
set(gca,'Fontsize',14)
subplot(2,2,2)
scatter(data(:,4),data(:,5))
xlabel('Weight','Fontsize',14); ylabel('Counts/MBq','Fontsize',14)
legend('r=-0.4226','Location','NorthEast')
set(gca,'Fontsize',14)
subplot(2,2,3)
scatter(data(:,3),data(:,4))
xlabel('Height','Fontsize',14); ylabel('Weight','Fontsize',14)
```

```
legend('r=0.4623','Location','NorthWest')
set(gca,'Fontsize',14)
subplot(4,2,6)
scatter(data(:,2),data(:,3),'o')
xlabel('Sex','Fontsize',14); ylabel('Height','Fontsize',14)
legend('r=0.7135','Location','North')
axis([-0.2 1.2 140 200])
set(gca,'Fontsize',14)
subplot(4,2,8)
scatter(data(:,2),data(:,4),'o')
xlabel('Sex','Fontsize',14); ylabel('Weight','Fontsize',14)
legend('r=0.4614','Location','North')
axis([-.2 1.2 30 120])
hold off
set(gca,'Fontsize',14)
%
%
% %%%%%%%%%%%%%%%%%%%%%%%%%%%%%%%%%%%%%%%%%%%%%%%%%%%%%%%%%%%%%%%%%%%%%%%%%%%
% %% Finally, how are the residuals of the fit behaving?
% %% Turn to the AIC derived model to judge the fit
% %% The coefficients found from the linear regression
ant_fitted_data=[-8245.221.*data(:,2)+...
                 65.06357.*data(:,1)-...
                 65.81197.*data(:,4)+...
                 63.54738.*data(:,2).*data(:,1)+...
                 49.90918.*data(:,2).*data(:,4)+...
                 .0083381*data(:,1).*data(:,4)+...
                 9866.491];
ant_residuals=data(:,5)-ant_fitted_data;

figure(3)
subplot(2,1,1)
[ant_resid_n,ant_resid_x]=hist(ant_residuals,25);
ant_resid_h=ant_resid_x(2)-ant_resid_x(1);
bar(ant_resid_x,ant_resid_n./(65*ant_resid_h),1);
hold on
%
ant_resid_mu=mean(ant_residuals)
ant_resid_sigma=std(ant_residuals)
ant_resid_xp=linspace(-4000,4000);
ant_resid_yp=normpdf(ant_resid_xp,ant_resid_mu,ant_resid_sigma);
plot(ant_resid_xp,ant_resid_yp)
hold off
ylabel('Relative frequency','Fontsize',16);

% %% And now repeat for the posterior counts from the AIC fit
pos_fitted_data=[-7374.622.*data(:,2)+...
                 56.31172.*data(:,1)-...
                 72.02218.*data(:,4)+...
                 54.34536.*data(:,2).*data(:,1)+...
```

```
                47.96459.*data(:,2).*data(:,4)+...
                0.1294645*data(:,1).*data(:,4)+...
                9763.234];
pos_residuals=data(:,6)-pos_fitted_data;

pos_mu=mean(pos_residuals)
pos_sigma=std(pos_residuals)

pos_xp=linspace(-4000,4000);
pos_yp=normpdf(pos_xp,pos_mu,pos_sigma);

ideal_pos_yp=normpdf(pos_xp,0,pos_sigma);

subplot(2,1,2)
[n,pos_x]=hist(pos_residuals,25);
h2=pos_x(2)-pos_x(1);
bar(pos_x,n./(65*h2),1);
hold on
plot(pos_xp,pos_yp);
hold on
plot(pos_xp,ideal_pos_yp,'r')
hold off
axis([-4000 4000 0 8e-4]);
xlabel('Residual (counts)','Fontsize',16);
ylabel('Relative frequency','Fontsize',16);
```

ReadSpectrum.m

```
% Opens and reads a spectrum file for the Millennium MG Gamma Camera
% Darin O'Keeffe, 20021024
% 20021031 Added save support
%    The    spectrum    files    are    stored    in    the    Genieacq    in
%/usr/genieacq/dataf/enghst.var

% Ask the user for the name of the file to process
[fileName, pathName] = uigetfile('*.*', 'Select the spectrum file to
process');

fullFileName = fullfile(pathName, fileName);

fid = fopen(fullFileName, 'r');

[rawSpectrum, count] = fread(fid,inf,'uint16');

plot(rawSpectrum);

% Save the data into an ASCII file
[pathstr,name,ext,versn] = fileparts(fullFileName);   % base it on the
current file name

saveFileName = [pathstr, filesep, name, '.txt'];

[saveFileName, savePathName] = uiputfile(saveFileName, 'Select the file
to save data to');

save(fullfile(savePathName, saveFileName), 'rawSpectrum','-ASCII');

% close the file before exiting
fclose(fid);
```

Line profiles

```
%%% Read in the line profiles taken from ImageJ
%% For the NEMA phantom in contact with detector 1
Det1_MC_horizontal_line_profile=dlmread('C:\Masters Part II\DICOM
Files\17_April\det1_contact_MC_horizontal_profile_det1');
Det1_EXP_horizontal_line_profile=dlmread('C:\Masters Part II\DICOM
Files\17_april\det1_contact_EXP_horizontal_profile_det1');

Det2_MC_horizontal_line_profile=dlmread('C:\Masters Part II\DICOM
Files\17_April\det1_contact_MC_horizontal_profile_det2');
Det2_EXP_horizontal_line_profile=dlmread('C:\Masters Part II\DICOM
Files\17_april\det1_contact_EXP_horizontal_profile_det2');

%% For the NEMA phantom in contact with detector 2
Det1_MC_horizontal_line_profile_det2=dlmread('C:\Masters Part II\DICOM
Files\17_April\det2_contact_MC_horizontal_profile_det1');
Det1_EXP_horizontal_line_profile_det2=dlmread('C:\Masters Part II\DICOM
Files\17_april\det2_contact_EXP_horizontal_profile_det1');

Det2_MC_horizontal_line_profile_det2=dlmread('C:\Masters Part II\DICOM
Files\17_April\det2_contact_MC_horizontal_profile_det2');
Det2_EXP_horizontal_line_profile_det2=dlmread('C:\Masters Part II\DICOM
Files\17_april\det2_contact_EXP_horizontal_profile_det2');

%% The middle of the image matrix of 256x256 or 578.56x578.56 = 578.26/2
or
%% 128 /0.442478 (conversion factor) see notes. But peak of MC results is
%% at 127
Centre=289.28; % mm

% % raw plots to determine peak of profiles
plot(2.26.*Det1_MC_horizontal_line_profile_det2(:,1),Det1_MC_horizontal_l
ine_profile_det2(:,2))
hold on
plot(Det1_EXP_horizontal_line_profile(:,1),Det1_EXP_horizontal_line_profi
le(:,2),'r')
legend('MC Det 1','Exp Det 1')
hold off
%% Raw plot profile leads to peaks of MC at 287 mm
%%                                    Exp at 278 mm
%% Thus, add on the difference ->> MC = 289.28 - 287 = 2.28 mm
%%                                  Exp = 289.28 - 278 = 12.28
%% This leads to us needing to shift the profiles to line up the centre
of
%% each peak by the following amounts
Det1_MC_profile_shift=2.28.*ones(length(Det1_MC_horizontal_line_profile),
1);
Det1_EXP_profile_shift=12.28.*ones(length(Det1_EXP_horizontal_line_profil
e),1);
```

```
%% Raw plot profile for det 2 leads to peaks of MC at 287.02 mm
%%                                              Exp at 293.8 mm
%% For Detector 2 MC ->> 289.28 - 287.02 = 2.26
%%               Exp ->> 289.28 - 293.8 = -4.52

Det2_MC_profile_shift=2.26.*ones(length(Det2_MC_horizontal_line_profile),
1);
Det2_EXP_profile_shift=-
4.52.*ones(length(Det2_EXP_horizontal_line_profile),1);

 % For Det 1 in contact with the camera face
figure[28]
subplot(1,2,1)
plot(2.26.*Det1_MC_horizontal_line_profile(:,1)+Det1_MC_profile_shift,Det
1_MC_horizontal_line_profile(:,2)./max(Det1_MC_horizontal_line_profile(:,
2)),'--r');
hold on
plot(Det1_EXP_horizontal_line_profile(:,1)+Det1_EXP_profile_shift,Det1_EX
P_horizontal_line_profile(:,2)./max(Det1_EXP_horizontal_line_profile(:,2)
));
hold on
axis([200 400 0 1.2])
title('LSF for Detector 1 with NEMA line source phantom in contact with
detector 1')
legend('Simulated','Experimental')
xlabel('Distance across camera face (mm)')
ylabel('Normalised counts')

% For Det 2 in contact with the camera face
subplot(1,2,2)
plot(2.26.*Det2_MC_horizontal_line_profile(:,1)+Det2_MC_profile_shift,Det
2_MC_horizontal_line_profile(:,2)./max(Det2_MC_horizontal_line_profile(:,
2)),'--r');
hold on
plot(Det2_EXP_horizontal_line_profile(:,1)+Det2_EXP_profile_shift,Det2_EX
P_horizontal_line_profile(:,2)./max(Det2_EXP_horizontal_line_profile(:,2)
));
hold off
axis([200 400 0 1.2])
title('LSF for Detector 2 with NEMA line source phantom win contact with
detector 1')
legend('Simulated','Experimental')
xlabel('Distance across camera face (mm)')
ylabel('Normalised counts')
```

Radial profiles

```
%% Radial profiles of the IEC COUNT RATE PHANTOM

%% Experimental results
EXP_det1_insert_only=dlmread('C:\Masters Part II\DICOM Files\Radial
Profile Plots\EXP_det1_insert_only_test');
EXP_det1_insert_plus_phantom=dlmread('C:\Masters Part II\DICOM
Files\Radial Profile Plots\EXP_det1_insert+phantom_test');

EXP_det2_insert_only=dlmread('C:\Masters Part II\DICOM Files\Radial
Profile Plots\EXP_det2_insert_only_test');
EXP_det2_insert_plus_phantom=dlmread('C:\Masters Part II\DICOM
Files\Radial Profile Plots\EXP_det2_insert+phantom_test')

%% Monte Carlo results
MC_det1_insert_only=dlmread('C:\Masters Part II\DICOM Files\Radial
Profile Plots\MC_det1_insert_only');
MC_det1_insert_plus_phantom=dlmread('C:\Masters Part II\DICOM
Files\Radial Profile Plots\MC_det1_insert+phantom');

MC_det2_insert_only=dlmread('C:\Masters Part II\DICOM Files\Radial
Profile Plots\MC_det2_insert_only');
MC_det2_insert_plus_phantom=dlmread('C:\Masters Part II\DICOM
Files\Radial Profile Plots\MC_det2_insert+phantom')

%% Normalise everything to 1
%% Experimental
norm_EXP_det1_insert_only=EXP_det1_insert_only(:,2)./max(EXP_det1_insert_
only(:,2));
norm_EXP_det1_insert_plus_phantom=EXP_det1_insert_plus_phantom(:,2)./max(
EXP_det1_insert_plus_phantom(:,2));

norm_EXP_det2_insert_only=EXP_det2_insert_only(:,2)./max(EXP_det2_insert_
only(:,2));
norm_EXP_det2_insert_plus_phantom=EXP_det2_insert_plus_phantom(:,2)./max(
EXP_det2_insert_plus_phantom(:,2));

%% Monte Carlo
norm_MC_det1_insert_only=MC_det1_insert_only(:,2)./max(MC_det1_insert_onl
y(:,2));
norm_MC_det1_insert_plus_phantom=MC_det1_insert_plus_phantom(:,2)./max(MC
_det1_insert_plus_phantom(:,2));

norm_MC_det2_insert_only=MC_det2_insert_only(:,2)./max(MC_det2_insert_onl
y(:,2));
norm_MC_det2_insert_plus_phantom=MC_det2_insert_plus_phantom(:,2)./max(MC
_det2_insert_plus_phantom(:,2));
```

```
% Now plot to compare simulated with experimental profiles
subplot(2,2,1)
semilogy(EXP_det1_insert_only(:,1),norm_EXP_det1_insert_only)
hold on
semilogy(MC_det1_insert_only(:,1),norm_MC_det1_insert_only,'r')
axis([0 100 0.0001 10])
xlabel('Pixels')
ylabel('Normalised integrated density')
legend('Exp','MC')
hold off
subplot(2,2,2)
semilogy(EXP_det1_insert_plus_phantom(:,1),norm_EXP_det1_insert_plus_phan
tom)
hold on
semilogy(MC_det1_insert_only(:,1),norm_MC_det1_insert_plus_phantom,'r')
axis([0 100 0.0001 10])
xlabel('Pixels')
ylabel('Normalised integrated density')
hold off
subplot(2,2,3)
semilogy(EXP_det2_insert_only(:,1),norm_EXP_det2_insert_only);
hold on
semilogy(MC_det2_insert_only(:,1),norm_MC_det2_insert_only,'r');
axis([0 100 0.0001 10])
xlabel('Pixels')
ylabel('Normalised integrated density')
hold off
subplot(2,2,4)
semilogy(EXP_det2_insert_plus_phantom(:,1),norm_EXP_det2_insert_plus_phan
tom);
hold on
semilogy(MC_det1_insert_plus_phantom(:,1),norm_MC_det2_insert_plus_phanto
m,'r');
axis([0 100 0.0001 10])
xlabel('Pixels')
ylabel('Normalised integrated density')
hold off
```

Appendix G

Activity distribution in the NCAT phantom

Average Clinical Male

Total	307	MBq	
Bone	**304**	**MBq**	
			Activity (MBq)
Volume of body:	86364.7502	ml	307
Volume of brain:	1054.1993	ml	0.04
Volume of brain stem:	35.1563	ml	0.00
Volume of cerebellum:	107.4219	ml	0.00
Volume of heart:	1099.6094	ml	0.04
Volume of right lung:	1309.3262	ml	0.05
Volume of left lung:	1066.1622	ml	0.04
Volume of liver:	1589.3555	ml	0.06
Volume of gall bladder:	33.2031	ml	0.00
Volume of stomach:	246.582	ml	0.01
Volume of spleen:	215.0879	ml	0.01
Volume of right kidney:	170.4102	ml	0.01
Volume of left kidney:	145.2637	ml	0.01
Volume of small intestine:	1199.9512	ml	0.04
Volume of asc. large int:	560.791	ml	0.02
Volume of desc. large int:	474.6094	ml	0.02
Volume of trans. large int:	375	ml	0.01
Volume of rectum:	152.5879	ml	0.01
Volume of bladder:	75.6836	ml	0.00
Volume of skeleton:	8766.8461	ml	**304.00**
skull + mandible:	896.7286	ml	31.10
mandible only:	108.6426	ml	3.77
right ribs:	618.8965	ml	21.46
left ribs:	603.5157	ml	20.93
sternum:	73.7305	ml	2.56
right clavicle:	63.2324	ml	2.19
left clavicle:	64.209	ml	2.23
right scapula:	255.8594	ml	8.87
left scapula:	256.3477	ml	8.89
cervical vert:	150.1465	ml	5.21
thoracic vert:	502.6856	ml	17.43
lumbar vert:	433.3496	ml	15.03
sacrum:	290.2832	ml	10.07
pelvis:	1314.6973	ml	45.59
right humerus (total):	201.1719	ml	6.98
right radius:	77.1484	ml	2.68

right ulna:	89.3555	ml	3.10
right hand:	128.418	ml	4.45
left humerus (total):	216.3086	ml	7.50
left radius:	78.125	ml	2.71
left ulna:	91.3086	ml	3.17
left hand:	128.9063	ml	4.47
right femur (total):	440.6738	ml	15.28
right tibia,fibula,patella:	436.7676	ml	15.15
right foot:	242.9199	ml	8.42
left femur (total):	432.3731	ml	14.99
left tibia,fibula,patella:	439.6973	ml	15.25
left foot:	239.9902	ml	8.32
Volume of prostate:	21.9727	ml	0.00
Volume of right testicle:	39.0625	ml	0.00
Volume of left testicle:	47.3633	ml	0.00
Weight	82.91	kg	

Activity in phantom parameter file

Bones	304.00
Spine	47.73
Pelvis	45.59
Ribs	210.68
Organs	0.35
Body	2.65

Average Clinical Female

Total activity	305	MBq
Bone activity	**303**	**MBq**

			Activity
Volume of body:	71810.3061	ml	305
Volume of brain:	846.1914	ml	0.02
Volume of brain stem:	29.7852	ml	0.00
Volume of cerebellum:	88.3789	ml	0.00
Volume of heart:	712.1582	ml	0.02
Volume of right lung:	739.9903	ml	0.02
Volume of left lung:	679.1993	ml	0.02
Volume of liver:	1227.5391	ml	0.03
Volume of gall bladder:	26.8555	ml	0.00
Volume of stomach:	197.5098	ml	0.01
Volume of spleen:	173.8281	ml	0.00
Volume of right kidney:	137.207	ml	0.00
Volume of left kidney:	116.2109	ml	0.00
Volume of small intestine:	975.586	ml	0.03
Volume of asc. large int:	456.7871	ml	0.01
Volume of desc. large int:	390.3809	ml	0.01
Volume of trans. large int:	311.0352	ml	0.01
Volume of rectum:	125.2441	ml	0.00
Volume of bladder:	51.2695	ml	0.00
Volume of skeleton:	6989.014	ml	**303.00**
skull + mandible:	725.3418	ml	31.4
mandible only:	93.2617	ml	4.0
right ribs:	437.2559	ml	19.0
left ribs:	429.6875	ml	18.6
sternum:	46.3867	ml	2.0
right clavicle:	50.7813	ml	2.2
left clavicle:	53.2227	ml	2.3
right scapula:	211.9141	ml	9.2
left scapula:	211.1817	ml	9.2
cervical vert:	131.5918	ml	5.7
thoracic vert:	407.4707	ml	17.7
lumbar vert:	353.5156	ml	15.3
sacrum:	232.1777	ml	10.1
pelvis:	1053.9551	ml	45.7
right humerus (total):	169.1895	ml	7.3
right radius:	65.918	ml	2.9
right ulna:	76.416	ml	3.3
right hand:	105.2246	ml	4.6
left humerus (total):	175.5371	ml	7.6
left radius:	66.1621	ml	2.9

left ulna:	77.8809	ml	3.4
left hand:	104.7363	ml	4.5
right femur (total):	343.5059	ml	14.9
right tibia,fibula,patella:	354.7363	ml	15.4
right foot:	200.1953	ml	8.7
left femur (total):	347.6563	ml	15.1
left tibia,fibula,patella:	357.4219	ml	15.5
left foot:	199.9512	ml	8.7
Volume of right breast:	1662.1095	ml	0.05
Volume of left breast:	1375.0001	ml	0.04
Volume of left ovary:	7.8125	ml	0.00
Volume of right ovary:	6.5918	ml	0.00
Volume of vagina:	0	ml	0.00
Volume of uterus:	20.5078	ml	0.00
Volume of left fl. tube:	0	ml	0.00
Volume of right fl. tube:	0	ml	0.00
Weight	69.06	kg	

Activity in phantom parameter file

Bones	303.00
Spine	48.76
Pelvis	45.69
Ribs	208.54
Organs	0.20
Body	1.80